



UNIVERSITÄT  
BAYREUTH

---

# Photoionization of atoms with ultrashort XUV laser pulses at extreme intensities

---

Der Universität Bayreuth  
zur Erlangung des Grades eines  
Doktors der Naturwissenschaften (Dr. rer. nat.)  
vorgelegte Abhandlung

von

Benjamin Kaiser

geboren am 18.09.1984 in Bobingen

1. Gutachter: Prof. Dr. Vollrath Martin Axt
2. Gutachter: Prof. Dr. Stephan Kümmel

Tag der Einreichung: 27.11.2014

Tag des Kolloquiums: 27.04.2015

## Abstract

---

The present thesis is concerned with the photoionization dynamics of atoms exposed to high intense and ultrashort XUV-laser pulses of free-electron lasers. In particular, the influence of coherent dynamics of the electrons as well as the electron-electron interaction are in focus of this survey and the resulting signatures as Rabi oscillations and characteristic spectra of photoelectrons are analysed. Furthermore, different levels of theory are applied for one-dimensional model atoms, providing a systematic manner to pinpoint the features induced by coherent and correlated electron dynamics. To this end, the exact solution of the time-dependent Schrödinger equation is determined numerically for a two electron system. To surmount the limitation of the latter to systems with a small number of electrons, the time-dependent reduced density matrix formalism is implemented on the Hartree-Fock level as well as one level above and thus accounts also for a correlated electron-electron interaction. Furthermore, for the ionization of resonantly driven atomic bound states an extended two level system is discussed, resulting in an analytic solution.

As a prime example of coherent quantum dynamics Rabi oscillations are studied in a two electron atom for a resonant laser coupling between the ground state and an excited bound state. In addition a single-photon absorption of the model atom in the excited bound state gives rise to an ionization process. It was found that the ground state occupation as a function of time exhibits damped Rabi oscillations. The ionization, which induces the damping, scales linearly with the field intensity. For the ion yields induced by a finite laser pulse a quadratic intensity scaling is observed for pulse lengths below the Rabi period. Consequently, at a critical pulse area the onset of Rabi cycles induces a transition between a quadratic and linear intensity scaling in the ion yields. In the high intensity regime the comparison between the results of a simplified solvable model, including only two bound states coupled to the ionization continuum, and the exact solution of the time-dependent Schrödinger equation reveals that the further excited localized states and the direct two-photon ionization of the ground state carry a non negligible contribution to the total ionization yields. Besides, a shift of the Rabi frequency compared to its value for an isolated level is found. The analytic solution of the simplified model manifests that the shift is related to the ionization. Thus, the higher ion yields observed for the time-dependent Schrödinger equation affect the respective Rabi frequency, acquiring a high renormalization of the Rabi frequency of an isolated system.

Investigations for an off-resonant excitation prove that the basic dependency of the Rabi amplitudes and of the Rabi frequencies on the detuning coincides with the one known for the isolated two level system. The detuning additionally affects the renormalization of the Rabi frequency. Depending on the sign of the detuning a Rabi frequency larger or smaller than in the isolated two level system is observed. However, the direct two-photon ionization of the ground state gains in importance already at small intensities compared to the resonant excitation and affects the intensity scaling of the ion yields. In particular, for a large detuning the transition from a quadratic to a

linear intensity scaling is determined by a competition between the direct two-photon ionization and the Rabi-assisted ionization instead of the critical pulse area needed for one Rabi cycle. For a fixed detuning the respective intensity at which the transition occurs is the same for all pulse durations as long as the ion yields do not reach the saturation regime. In addition, also signatures of the coexistence of different Rabi processes are observed as beats in the time evolution of the occupation of the ground state.

The influence of correlated electron dynamics on the ionization process has been studied for a laser excitation in the vicinity of the single-photon ionization threshold of a helium model. The comparison between the time-dependent Hartree-Fock theory and the exact numerical solution of the Schrödinger equation reveals that correlation effects gain in importance at a high radiation intensity with a photon energy close to the threshold and strongly affect the time evolution of the ground state population. Furthermore, the momentum distributions of the electrons emitted in a double ionization process have been analysed. The characteristic signatures of different double ionization processes allow to separate their respective parts in the total double ionization yield. In case of the coexistence of a sequential two-photon and a non-sequential three-photon double ionization the individual ion yields scale quadratically and cubically with intensity. However, even though the three-photon double ionization dominates at high intensities its signature is not observed in the total ion yields. Instead, a power law with an exponent between two and three is found. Studying the temporal evolution of the two-electron momentum distribution reveals a broad peak at short times which becomes narrower with ongoing time. This feature reflects the energy-time uncertainty and indicates a strong coherent regime at short times. A further analysis of the temporal evolution of the double ionization yields for both electrons leaving the atom in the same direction exhibits signatures of a recapture process.

Finally, the time-dependent reduced density matrix formalism is applied for an atom interacting with an ultrashort laser pulse. To this end, the Bogolyubov-Born-Green-Kirkwood-Yvon hierarchy is truncated one level above the mean field level and therefore correlations between electrons are included. The reduced one particle matrix and the two particle correlations are represented by the finite element discrete variable representation. The numerically obtained time traces of the Hartree-Fock orbitals forming the ground state are analysed for two, four and six electron atoms excited by an intense ultrashort XUV laser pulse. In order to identify correlation induced processes in the ionization dynamics, results for correlated electrons are compared with the time-dependent Hartree-Fock theory. In this manner, signatures of the shake-off ionization process and the Auger decay are found in the time evolution of the occupation of the Hartree-Fock orbitals.

## Kurzfassung

---

Ziel dieser Arbeit ist die theoretische Behandlung der Photoionisation von Atomen durch hoch intensive Femtosekunden-XUV-Laserpulse von Freien-Elektronen-Lasern, wobei Einflüsse auf den Ionisationsprozess durch kohärente Dynamik der Elektronen sowie der Wechselwirkung zwischen den Elektronen im Mittelpunkt der Untersuchungen stehen. Deren Auswirkungen, wie Rabi-Oszillationen und charakteristische Spektren der Photoelektronen, werden in eindimensionalen Atommodellen auf unterschiedlichen Ausbaustufen der Theorie diskutiert. Der Vergleich zwischen Ergebnissen für verschiedene Ausbaustufen der Theorie ermöglicht eine systematische Analyse der Einflüsse von kohärenter Dynamik und der Elektron-Elektron-Wechselwirkung auf die Ionisation. Im Speziellen wird für ein Zweielektronenatommodell die exakte Lösung der zeitabhängigen Schrödingergleichung numerisch bestimmt. Um deren Begrenzung auf Atome mit einer geringen Anzahl an Elektronen zu überwinden, wird die Anwendung des zeitabhängigen Formalismus der reduzierten Dichtematrix auf die Photoionisation erprobt. Diese Theorie wird auf der Hartree-Fock Stufe sowie auf einer Ausbaustufe, die Korrelationen der Elektronen berücksichtigt, implementiert. Die analytische Lösung eines erweiterten Zweiniveausystems unterstützt die Untersuchung einer resonanten Anregung zweier gebundener atomarer Zustände und deren Ionisation.

Als Paradebeispiel für kohärente Quantendynamik werden Rabi-Oszillationen in einem Zweielektronenatom für eine resonante Laserkopplung zwischen dem Grundzustand und einem angeregten gebundenen Zustand analysiert. Der angeregte Zustand kann durch die Absorption eines Photons ionisiert werden. Die Grundzustandsbesetzung des Atoms zeigt gedämpfte Rabi-Oszillationen, wobei die Dämpfung eine unmittelbare Folge der Ionisation des angeregten Zustands darstellt und linear mit der Intensität des Lasers skaliert. Im Fall einer kleinen Pulsfläche, die keinen abgeschlossenen Rabi-Zyklus induziert, zeigt die Ionisation als Funktion der Laserintensität eine quadratische Abhängigkeit. Das Einsetzen der Rabi-Oszillationen bei einer kritischen Pulsfläche bedingt daher einen Übergang zwischen quadratischem und linearem Skalierungsverhalten der Ionisation bezüglich der Intensität. Für extrem hohe Intensitäten ergibt der Vergleich zwischen Ergebnissen eines vereinfachten Modells, das ein Zweiniveausystem an ein Kontinuum koppelt und der zeitabhängigen Schrödingergleichung, dass weitere in der exakten Lösung enthaltene gebundene Zustände sowie die direkte Zweiphotonenionisation des Grundzustandes einen zusätzlichen Beitrag zur Ionisation leisten. Außerdem weicht die im Modell ermittelte Rabi-Frequenz von der eines isolierten Zweiniveausystems ab. In der analytischen Lösung des vereinfachten Modells ist die Frequenzverschiebung eine direkte Folge der Ionisation. Daher beeinflusst die hohe Ionisation in der exakten Lösung die Rabi-Frequenz und führt zu einer starken Renormalisierung bezüglich der Rabi-Frequenz eines isolierten Zweiniveausystems.

Weitere Analysen für den Fall einer off-resonanten Kopplung zweier atomarer Zustände zeigen ähnliche Abhängigkeiten der Amplitude und der Frequenz der Rabi-Oszillationen von der Verstimmung des Lasers bezüglich der Resonanzenergie wie in einem isolierten Zweiniveausystem. Zudem beeinflusst die Verstimmung die Renormalisierung der Rabi-

frequenz. In Abhängigkeit von deren Vorzeichen wird meistens eine größere wie auch kleinere Rabi-Frequenz als in einem isolierten Zweiniveausystem gefunden. Daneben beobachtet man im Vergleich zu einer resonanten Anregung einen größeren Einfluss der direkten Zweiphotonenionisation des Grundzustandes auch bei niedrigen Intensitäten. Dieser wirkt sich auf den Übergang von einer quadratischen zu einer linearen Intensitätsabhängigkeit der Ionisation aus. Anstelle des Arguments der Pulsfläche, das für kleine Verstimmungen ähnlich wie bei resonanter Anregung den Skalierungsübergang auszeichnet, bestimmt für eine stärkere Verstimmung die Konkurrenz zwischen direkter Zweiphotonenionisation und Rabi-assistierter Ionisation das Skalierungsverhalten des Ionenstrahles. Zudem erweisen sich Schwebungen im Zeitverlauf der Besetzung des Grundzustandes als Signatur einer Koexistenz zweier Rabi-Prozesse.

Um Auswirkungen von Korrelationen zwischen Elektronen zu analysieren, wird die Photoionisation eines eindimensionalen Helium Atommodells in der Nähe der Einphotonionisationsschwelle untersucht. Der Vergleich zwischen der zeitabhängigen Hartree-Fock-Theorie und der exakten Lösung der Schrödinger Gleichung zeigt, dass knapp über der Einfachionisationsschwelle für hohe Intensitäten starke Korrelationseffekte auftreten und den Zeitverlauf der Grundzustandsbesetzung stark beeinflussen. Zudem werden die verschiedenen Doppelionisationsprozesse anhand ihrer charakteristischen Impulsverteilung zwischen den abgegebenen Elektronen identifiziert. Bei einer Koexistenz von nichtsequentieller Zwei- und sequentieller Dreiphotonendoppelionisation zeigen die jeweiligen Ionenstrahle eine quadratische und kubische Intensitätsabhängigkeit. Dennoch resultiert die Dominanz des Dreiphotonenprozesses bei hohen Intensitäten nicht in das erwartete kubische Skalierungsverhalten der gesamten Doppelionisation. Stattdessen folgt die Intensitätsabhängigkeit der gesamten Doppelionisation einem Potenzgesetz mit einem Exponenten zwischen zwei und drei. Des Weiteren zeigt die Impulsverteilung der freien Elektronen zu kurzen Zeiten ein breites Maximum, das mit fortschreitender Zeit schmaler wird. Diese Signatur der Energie-Zeit-Unschärfe weist auf ein kohärentes Regime bei kurzen Zeiten hin. Eine Analyse des Anteils der Doppelionisation bei dem beide Elektronen das Atom in dieselbe Richtung verlassen zeigt Hinweise darauf, dass durch die Coulomb-Abstoßung zwischen den Elektronen eines von ihnen wieder vom Kern eingefangen wird.

Der zeitabhängige Dichtematrix-Formalismus wurde zur Modellierung der Wechselwirkung zwischen einem eindimensionalen Atommodell und einem ultrakurzen Laserpuls angewandt. Dafür wurde die Bogolyubov-Born-Green-Kirkwood-Yvon-Hierarchie eine Stufe über der Hartree-Fock-Stufe abgebrochen, wodurch Korrelationen zwischen den Elektronen berücksichtigt werden. Als Basisfunktionen für die Darstellung der reduzierten Ein- und Zweiteilchen-Dichtematrizen wird eine Finite-Elemente-Methode verwendet. Die numerischen Ergebnisse für die Ionisation von Zwei-, Vier- und Sechselektronenatomen werden anhand der Besetzungen der Hartree-Fock-Orbitale des Grundzustandes als Funktion der Zeit analysiert. Um durch Korrelationen induzierte Prozesse in der Ionisation zu identifizieren, werden Ergebnisse für korrelierte Elektronen mit denen der Hartree-Fock-Stufe verglichen. Auf diese Weise konnten Signaturen gefunden werden, die auf Shake-off-Ionisation und Augerzerfälle hinweisen.

# Contents

<b>I. Introduction and motivation</b>	<b>1</b>
I.1. Opportunities of free-electron-lasers . . . . .	2
I.2. Photoionization of atoms with XFEL-radiation . . . . .	4
I.3. Theoretical methods for photoionization . . . . .	7
I.3.1. Rate-equations and cross sections . . . . .	8
I.3.2. Wave function based methods . . . . .	9
I.3.3. Reduced many-particle methods . . . . .	10
<b>II. Applied methods and models</b>	<b>13</b>
II.1. One-dimensional atom models . . . . .	13
II.2. Finite-element discrete variable representation . . . . .	15
II.3. Time-dependent Schrödinger equation . . . . .	19
II.4. Reduced density matrix formalism . . . . .	20
II.5. Generic model for Rabi-assisted ionization . . . . .	21
<b>III. Ionization of resonantly driven atomic states</b>	<b>27</b>
III.1. Non-interacting electrons . . . . .	27
III.2. Interacting electrons . . . . .	30
III.3. Impact on the ionization dynamics . . . . .	32
<b>IV. Ionization of off-resonantly driven atomic states</b>	<b>35</b>
IV.1. Negative laser detuning . . . . .	37
IV.1.1. Renormalization for negative detuning . . . . .	41
IV.1.2. Influence on the ionization yields . . . . .	42
IV.2. Positive laser detuning . . . . .	45
IV.2.1. Renormalization for positive detuning . . . . .	49
IV.2.2. Influence on the ionization yields . . . . .	50
<b>V. The role of electron correlations</b>	<b>55</b>
V.1. Dynamics of the ground state . . . . .	56
V.2. Few photon double-ionization . . . . .	58

V.3. Time dependence of double ionization . . . . .	61
<b>VI. Reduced density matrix formalism</b>	<b>65</b>
VI.1. Equations of motion . . . . .	66
VI.1.1. Separation of spin and basis function variables . . . . .	67
VI.1.2. Choice of the initial values . . . . .	69
VI.2. Time propagation scheme . . . . .	70
VI.3. Results . . . . .	71
VI.3.1. Two electron atoms . . . . .	73
VI.3.2. Four electrons . . . . .	75
VI.3.3. Six electrons . . . . .	77
VI.3.4. Remarks . . . . .	79
<b>VII. Summary and outlook</b>	<b>83</b>
<b>Publications</b>	<b>101</b>
<b>Acknowledgment</b>	<b>103</b>



# Introduction and motivation

The present thesis is part of the project “Changing of atomic form factors by ultrashort intensive x-Ray pulses and their influence on X-ray scattering-patterns”<sup>1</sup>, which accounts for the new and extraordinary conditions for X-ray scattering experiments provided by free-electron lasers (XFEL) in the extreme ultraviolet (XUV) and X-ray regime. In contrast to common X-ray synchrotrons, for the novel XFEL sources one pulse is sufficient to record a scattering pattern but also alters the target to a high degree [115]. Due to the high photon flux of an XFEL, the target atom is expected to undergo multiple photoionization, excitations and relaxations. Therefore, the assumption of the atoms as static scatterers during the interaction with the radiation of an XFEL might lose its general validity [59]. In addition, signatures of the dynamics of the electrons could appear in the scattering signal. Within this framework the thesis elaborates on the theoretical description of the time evolution of the photoionization, elaborating the influence and need of coherent and correlated electron dynamics.

---

<sup>1</sup>Original german title: "Veränderung atomarer Formfaktoren durch ultrakurze intensive Röntgenpulse und deren Auswirkungen auf Röntgenbeugungsmuster“.

## I.1 Opportunities of free-electron-lasers

---

The new generation of free-electron lasers provides radiation with extreme high intensities, ultrashort femtosecond pulse durations and a high coherence for photon energies reaching from the XUV to the hard X-ray regime. Until now exist four running facilities providing XUV photons (FLASH in Hamburg, Germany and FERMI in Trieste, Italy) and hard X-rays (the LCLS in Stanford, USA and SACLA in the Hyogo Prefecture, Japan). A detailed list of facilities in construction can be found in reference [127]. The concept of creating coherent light with free-electron lasers has been developed [99] and realised [31] about four decades in the past. It is based on the interaction between a relativistic electron beam and electromagnetic waves both passing through a periodical magnetic field. Its huge advantage in comparison with standard lasers rises upon the in principle continuously tunable photon energy over an large range accessing also the XUV and X-ray regime. The high requirements on the quality of the electron beam and the lack of mirrors for X-rays had limited the application to infrared and optical light waves using a external cavity for amplification. Nevertheless developments in accelerator technology enabled the first realisation of a FEL in the XUV regime at the TESLA Test Facility [4, 10] using self-amplified spontaneous emission (SASE) [80], followed by FLASH [1, 9], LCLS [38], FERMI [2] and SACLA [174]. The photon-beam characteristics [1] of those facilities outmatch the one of standard synchrotrons by magnitudes reaching more than a 1000 times higher peak brilliance<sup>2</sup>. A XFEL pulse can carry  $10^{13}$  photons per pulse with a peak power of several gigawatts and a duration of 25-500 femtoseconds [1, 2, 9, 38]. In spite of the impressive and extraordinary performance, the operation of XFELs has just started and is therefore still cumbersome, stimulating further developments. The SASE principle causes fluctuations in the intensity and pulse shape of the XFEL pulse, because it is initiated by noise [1, 9, 144]. In order to improve this deficit seeding schemes are applied, triggering the amplification by an external seed signal [2, 3, 176]. Substantial progress has been achieved in the characterisation of individual XFEL pulses via terahertz streaking [50] and cross-correlation techniques [34]. Furthermore, recent achievements [30] in focusing the radiation enable pulses with intensities up to  $10^{17}$  W/cm<sup>2</sup> and propose that a value of  $10^{19}$  W/cm<sup>2</sup> is within reach.

With these unique properties the XFELs enable new possibilities for imaging nano and atomic structures, the observation of ultra fast dynamics and exposing matter to extreme conditions. The possibility of imaging nano and atomic structures in the noncrystalline phase is of great interest and has been considered in the year 2000 to be achieved with radiation provided by an XFEL [115]. On the one hand the coherence of the radiation and the high number of photons per pulse induce a sufficient number of scattering events to record a coherent diffraction pattern with a single shot. Additionally, the ultrashort pulse duration assures that the destruction of the structure of the sample caused by the radiation damage is not affecting the scattering process, also denoted

---

<sup>2</sup>Brilliance is also denoted as brightness and defined as photons  $s^{-1} \text{ mm}^{-2} \text{ mrad}^{-2}$  per 0.1% spectral bandwidth.

as "diffracting before destroying". This scheme has been predicted theoretically for a range of photon energies, covered by the recent XFELs and targets as nano-structured materials, molecules, clusters and proteins [17, 58, 61, 115] and was first realised 2006 at FLASH in Hamburg [23]. In the latter the far field intensity diffraction pattern has been recorded and iterative phase retrieval techniques [42, 106] were applied to reconstruct the structure of the sample. Further imaging experiments at FLASH and LCLS [18, 24, 104, 155], pave the way for a recent achievement at the LCLS. In a bio-medical investigation of the structure and mechanism of the enzyme *Trypanosoma brucei* cysteine protease cathepsin B, important contributions to develop therapies against the sleeping sickness [125] were achieved.

Furthermore, both the short pulse duration and the short wavelength of the XFEL radiation have led to exciting investigations of dynamic phenomena, providing high temporal and spatial resolution. Different schemes of pump-probe experiments have been established, in which the XFEL pulse often serves as the probe pulse applying an X-ray spectroscopy method with a defined time delay to the pump-pulse. The photon energy of the pump-pulse is chosen with respect to the subject of interest. In particular, for the observation of magnetic dynamics an optical pump laser is used in combination with time-resolved resonant X-ray diffraction [33, 120]. This scheme has been applied to examine the transition from the collinear to the spiral antiferromagnetic phase in CuO [71]. In another experiment of the same type the initial strongly coupled order of spin and charge in stripped  $\text{La}_{1.75}\text{Sr}_{0.25}\text{NiO}_4$  was driven out of equilibrium by an optical laser to observe the regeneration of the initial state [25]. Furthermore, the probe pulse can be utilized for X-ray absorption near-edge spectroscopy instead of resonant X-ray diffraction, e.g. for studying spin crossover dynamics [95]. Of course also Bragg peaks in diffraction patterns, recorded by the probe pulse, give insight in the dynamics of periodic structures, as demonstrated at FLASH [36]. In the latter, lattice vibrations were induced in a colloidal crystal by an infrared laser and probed with an XUV pulse. Another desired target are the dynamics of molecules. In particular it was proposed to gather detailed knowledge about the evolution of chemical reactions. First proceedings have been achieved by identifying the ionization and dissociation steps of diatomic iodine molecules exposed to a strong near-infrared laser [82]. Therefore Kriknova et al. have measured the characteristic kinetic release energy of iodine ion fragments as a function of the delay time between a near-infrared and XUV pulse. Afterwards they associated the kinetic release energy with the product resulting from the instantaneous impact of the XUV pulse on a specific intermediate state in the dissociation process. Beside iodine also diatomic oxygen and nitrogen molecules have been in focus, applying XUV-pump-XUV-probe experiments [100, 139].

In the references discussed so far, the XFEL radiation has been mainly utilized as a unique tool for imaging and tracing physical processes. Moreover, with an XFEL it is possible to realise unexplored states of matter and access new physical phenomena, in particular with respect to the plasma state. By irradiating xenon cluster the generation and dynamics of a nanoplasma was investigated [19, 48, 81] to obtain detailed knowledge of optical properties and relation between cluster size and the initiated Coulomb expansion. Furthermore, plasmas were also generated by exposing solid samples to XFEL

radiation. Here, attention was especially paid to the destruction process [46, 60, 169] and to the extraordinary behaviour, as the transition of aluminium into a transparent state due to the strong photoionization [114].

## **I.2 Photoionization of atoms with XFEL-radiation**

Since the photoionization of atoms is present in many applications of XFELs and starts the destruction process to obtain detailed knowledge about it is of importance. A very fundamental and basic situation for the understanding of photoionization by XFEL radiation is the interaction between the intensive femtosecond X-ray pulse and an isolated atom. In contrast to the ionization induced by infrared and optical lasers, in which the Coulomb field of the atomic core is bent by the strong electric field of the laser enabling tunnel ionization and mainly interacting with valence electrons, the photons of XUV and X-ray radiation have sufficient energy to release electrons of the inner shell of the atom by the absorption of only a few or even one photon.

The photoionization of rare gases exposed to high intense ultrashort XUV and X-ray pulses has been in focus in a couple of experiments, primarily detecting the created ions using ion time-of-flight spectroscopy [129, 136, 137, 157, 158, 170, 175]. This method measures the yields of different charged ions and mostly deduces the dominating processes from the intensity dependence of the respective ion yield. Perturbation theory predicts a power law for the ion yield induced by a photoionization process with XUV and X-ray photons, in which the base is given by the intensity and the exponent by the number of involved photons.

First realisations of this scheme at FLASH in the XUV regime [158, 170] using neon at photon energies of 38.4 eV and 42.8 eV, argon and xenon at 12.7 eV and intensities up to  $10^{14}$  W/cm<sup>2</sup> indicated that sequential multiphoton ionization of electrons is the dominating process. Thereby one electron after the other is ejected, always absorbing the minimal amount of photons, necessary to access the next higher charged ion state, instead of the direct instantaneous release of two or more electrons at once. Additionally, due to the applied low photon energy, the ionization starts with the most outer, only lightly bound electrons. In an experiment with neon and 230-340 fs X-ray pulses at the LCLS [175] the same behaviour was found in the case of 800 eV, where only the L-shell electrons can be ripped off. For these excitation conditions the ion yield as a function of ionic charge state decreases monotonic. On the contrary the higher applied photon energies of 1050 eV and 2000 eV were able to release also the K-shell electrons. The preferred ejection of K-shell electrons creates a "hole" in the electronic configuration which subsequently decays by the ejection of an Auger electron. This process results in a higher probability of the atom to end up in an even charged ionic state.

Even though these results suggest that lowest order perturbation theory might be adequate to describe the dominating photoionization process induced by femtosecond intense XUV and X-rays pulses, an extraordinary behaviour has been observed in particular for xenon [137, 157]. In reference [157] xenon was exposed to photons of 93 eV

and a peak intensities of  $10^{16}$  W/cm<sup>2</sup>, creating highly charged states up to Xe<sup>21+</sup> due to the absorption of almost 60 photons in 10-20 femtoseconds. The authors conclude out of their results for low irradiation that the initial process probably is a sequence of one-photon ionizations of the 4d shell as predicted in the framework of perturbation theory. Subsequently Auger decays take part. In this manner Xe<sup>4+</sup> can be reached. Afterwards the 5p shell is supposed to be completely ionized by sequential one-photon processes leading to Xe<sup>6+</sup>. Higher ion states could be reached by multiphoton ionization with an increasing number of photons. However the authors announced that the applicability of perturbation theory on their observation of Xe<sup>21+</sup> might be questionable. They also discussed that a strong correlation between the 4d electrons could induce collective effects enabling the extraordinary high degree of ionization. For heavy atoms as xenon the ionization thresholds decrease with increasing ionization and therefore further sequential multiphotons ionization processes are in competition with ionization paths including excited states, which are possibly effected by quantum coherences and electron-electron correlations. A further confirmation of this conclusion is provided by a recent experiment at LCLS [137] with xenon irradiated with 1.5 and 2.0 keV photons. The observed ion yields for 2.0 keV excitations are in good agreement with results obtained by rate equations, but in the case of 1.5 keV excitations theoretical predictions only coincide with the experiment for ion states below Xe<sup>28+</sup> and could not reproduce the high amount of highly charged states up to Xe<sup>36+</sup>. The ionization thresholds for different one electron orbitals as a function of charge state manifest that the threshold of the 3s orbitals falls below 1.5 keV for ion states exceeding Xe<sup>18+</sup>. The same holds for the 3d orbitals in the case of ion states higher than Xe<sup>24+</sup>. Thus, a further single ionization of the ions is no longer possible. Based on this analysis, the authors explain their observation of highly charged states up to Xe<sup>36+</sup> with "resonance-enabled X-ray multiple ionization" described as "highly efficient transient resonant excitation process in highly charged ions accompanied by hollow-atom formation and auto-ionization of multiple excited states". A similar observation has been made for krypton [136].

So far, measuring the ion yields, comparing them with results obtained by rate equations and analysing their intensity dependence may give an indication about present processes. Additional information which help to identify involved processes and can be estimated theoretically is the kinetic energy of the released photoelectrons, their angular distribution and the involved transient atomic states. Two useful and well-established experimental methods to obtain these quantities are electron [39] and fluorescence spectroscopy. The latter has been applied besides time of flight spectroscopy in the above mentioned experiments at LCLS with xenon [137] and krypton [136]. The measured fluorescence spectrum in these experiments supplied the assumption of a "resonance-enabled X-ray multiple ionization"-regime because emitted photons could be associated with relaxations in highly charged xenon ions which possess an excited electron configuration. In this manner the role of transient states, which are involved in the generation of highly ion states, has been identified. Beside fluorescence spectroscopy electron spectroscopy has been adopted to investigate ionization of XFEL-radiation [109, 113, 128, 135, 153]. In particular for a further clarification of the mechanism responsible for the unexplained high degree of ionization of xenon observed at FLASH

[128] and for confirming the excitation of a doubly excited state in helium by absorbing two photons [113].

In addition to the above discussed ionization experiments, demonstrating the accessibility of unexpected behaviour with XFELs, particular interest has also been paid to ionization processes which do not play a dominating part in the photoionization of atoms, but rather aim at understanding the basic principles of the interaction between photons and the electrons of an atom. These processes, also denoted as few photons few electrons reactions, are mostly characterised by their small cross sections and therefore are predestined to be accessible by XFEL radiation. After the investigation of one-photon double ionization of helium [5, 78] at synchrotrons, the two-photon double ionization (TPDI) of helium consequently moved into focus and has received enormous theoretical attention [40, 44, 45, 54, 66, 70, 88, 89, 92, 119]. In general, the TPDI of helium is classified into two mechanisms, the sequential and non-sequential (direct) double ionization. In the sequential process the double ionization evolves step by step. After the absorption of one photon by the neutral atom, inducing the ejection of an electron, the second photon releases the now stronger bound electron of the residual ion without being further affected by the first step. The kinetic energy of the two ejected electrons is determined by the energy conservation separately for each step according to the photon energy and the ionization thresholds of helium (24.6 eV) or the ion  $\text{He}^+$  (54.4 eV) and therefore results in two different values. Obviously this mechanism is only possible for photon energies above 52 eV [54, 88]. In the case of non-sequential TPDI the two electrons absorb the two photons simultaneously and are influencing each other while leaving the atom. Thus, the electrons are leaving the atom preferentially in opposite direction. Also the partitioning of the kinetic energy between the electrons is not as strictly defined as for the sequential TPDI, resulting in a more uniform energy distribution [40, 54]. The two ionization thresholds for neutral and single charged helium add up to the double ionization threshold of 79.0 eV which can be exceeded by two photons with an energy larger than 39.5 eV. So between 39.5 eV and 54.4 eV only non-sequential TPDI is present whereas above 54.4 eV sequential TPDI dominates, although both processes are energetically allowed [66]. A qualitative similar behaviour is contained in the double ionization of neon, concerning the two 2s electrons. First experimental signatures [111, 112, 117] of non-sequential TPDI of helium with XUV photons, generated via higher harmonic generation, were found in a quadratic power law for yield of the bare helium core as a function of intensity. To survey in detail theoretical predictions for TPDI, concerning the released electron's kinetic energy and angular momentum distribution, a "reaction microscope" [166] has been applied at FLASH. In first experiments it recorded the recoil-ion momentum of helium and neon ions [86, 138]. By neglecting the absorbed photons the momentum conservation has to be fulfilled only for the momentum of the neutral atom before the ionization and the momentum of the electrons and ion afterwards. Thus, the ion momentum distribution is affected by the momenta of the electrons [67] and reflects their characteristic properties in the case of sequential and non-sequential TPDI. Furthermore, the kinetic energies of the two electrons, ejected by the same sequential TPDI event, have been detected [87, 139] for neon, but only with a precision sufficient to conclude a qualitative agreement with theory.

Also resonant excitation of atomic bound states gains increasing attention, since on the one hand it has been connected with unexpected behaviour in Xenon [129, 136] as the ionization thresholds of the ions exceed the photon energy. On the other hand, XFEL radiation is supposed to induce Rabi oscillations between atomic states [132] and therefore could access the coherent regime of quantum dynamics driven by X-rays. Pioneering works [16, 79] have demonstrated theoretically the coexistence of Rabi-oscillations and ionization. However, it seems unlikely that measuring the occupation of atomic states as a function of time will be possible in the near future, as it had been done for quantum dots [124]. Nevertheless, recent experiments found signatures of Rabi oscillations in the ion yield and the Auger electron spectrum. In reference [146] the absolute two-photon absorption cross-section of Helium has been measured between 20 and 23 eV. An unexpected behaviour is observed if the photon energy is in resonance between the initial ground state and an excited bound state. In particular, the exponent of the power dependence between ion yield and laser intensity deviates from the behaviour predicted by lowest order perturbation theory. A theoretical investigation [143] established that Rabi oscillations are affecting the ionization dynamics and are responsible for deviations from perturbation theory. A more complex scenario accompanied by Rabi oscillations is the resonant Auger decay [132], which is initialized by the ionization of a valence-electron. Thereafter, one resonantly drives a transition between the single ionized states with a hole either in the valence or in the core shell. The induced Rabi cycling is accompanied by the decay of the involved excited ion state by the release of an Auger electron or a photon via simulated emission. This scheme has been realised with neon at the LCLS [76] and a broadened Auger electron peak was observed. As theory predicted [116, 132, 133] the broadening of the peak is due to Rabi oscillations.

### I.3 Theoretical methods for photoionization

---

In this chapter currently applied methods for the description of the interaction between an atom and XFEL radiation are presented. At first, general assumptions commonly used in this field are discussed, following reference [145]. In comparison with the electron rest mass of 511 keV the XUV and X-ray photon energy is rather small. Therefore relativistic quantum electrodynamics are neglected leading to a Hamiltonian approach for the electrons and the nucleus in an electromagnetic field. Since the mass of a nucleus exceeds the mass of an electron by magnitudes and the electromagnetic fields of XUV and X-rays are oscillating fast, it is well justified to assume a fixed nucleus and to account for the electrons of the atom only. Finally, for the electrons of an atom interacting with XFEL radiation the Hamiltonian has the following form:

$$H = H_{\text{kin}} + H_{\text{core-el.}} + H_{\text{el.-el.}} + H_{\text{field}} + H_{\text{field-el.}} \quad (\text{I.1})$$

$H_{\text{kin}}$  is the operator for the kinetic energy and  $H_{\text{el.-core}}$  describes the attraction of the coulomb potential of the positive charged nucleus on the electrons.  $H_{\text{el.-el}}$  accounts for

the repulsive interaction between the electrons. In the case of  $N$  electrons and Gauss units they are given by the following expressions:

$$H_{\text{kin}} = \sum_{i=1}^N -\frac{1}{2m_e} \nabla_i^2, \quad H_{\text{core-el.}} = \sum_{i=1}^N -\frac{e^2 \cdot Z}{|\mathbf{x}_i|}, \quad H_{\text{el.-el.}} = \sum_{\substack{i,j=1 \\ i < j}}^N \frac{e^2}{|\mathbf{x}_i - \mathbf{x}_j|}. \quad (I.2)$$

The free electromagnetic field is described by  $H_{\text{field}}$  and the interaction of the field with the electrons is accounted by  $H_{\text{field-el.}}$ . Until now the question of treating the electromagnetic field either classical or quantized has not been answered. Of course the quantization of the electromagnetic field leads to a more accurate model than classical waves. To reduce the complexity of the model and the effort of numerical approaches a classical treatment is often used, verified due to the coherence and high photon number of an XFEL pulse. In case of XUV radiation the wavelength is still much larger compared to the size of an atom. Thus, a electric field constant with respect to  $\mathbf{x}$  but oscillating in time is assumed. Nevertheless, one should be aware that the classical field neglects spontaneous photoemission.

With this Hamilton operator at hand the photoionization of an atom is contained in the evolution of the  $N$ -electron wave function, which is determined by the time dependent Schrödinger equation. Therefore, the task for a theoretical description of photoionization is defined by solving the time dependent Schrödinger equation (TDSE) for the above written Hamilton operator.

$$i\hbar \frac{\partial}{\partial t} |\Psi\rangle = H |\Psi\rangle. \quad (I.3)$$

However, the solution of the TDSE in this case is a challenging mission. The analytical calculation of a wave function evolving under an explicit time dependent Hamilton operator is limited to a few special cases. Thus, for an intensive ultrashort laser pulse numerical approaches are the only possible strategy to trace photoionization, but are connected with an increasing computational effort for a rising number of electrons due to their interaction between themselves. Up to now in the case of a classical oscillating electric field a complete numerical solution of (I.3) exist in three dimensions for maximal two electrons [92] and in one dimension for three electrons [141]. Obviously, to investigate the response of atoms with more electrons to an intensive ultrashort laser pulse one has to apply approximating methods. In the following commonly used approaches are presented and their capabilities accounting for coherent quantum dynamics and electron-electron correlations are discussed.

### I.3.1. Rate-equations and cross sections

A well established method to describe the photoionization of an atom by XUV or X-ray photons are rate-equations, which couple the occupation numbers of different ion species and their electronic configurations via transition rates for ionization, excitation and relaxation processes. An introduction in their application in X-ray physics is given in [145]. The transition rate or cross section from an initial state  $|I\rangle$  to a final state  $|F\rangle$

is obtained by time dependent perturbation theory where the unperturbed system is represented by

$$H_0 = H_{\text{kin}} + H_{\text{core-el.}} + H_{\text{el.-el.}} + H_{\text{field}}. \quad (\text{I.4})$$

Both states  $|I\rangle$  and  $|F\rangle$  are assumed to be eigenstates of  $H_0$ . In the limit of long times compared to the period of a cycle of electromagnetic-field one arrives at Fermi's golden rule and the cross sections are mainly determined by the matrix element  $\langle I|H_{\text{field-el.}}|F\rangle$ .

For calculating the matrix elements the first difficulty consists in obtaining an explicit form of the states  $|I\rangle$  and  $|F\rangle$ . In particular for the electron subsystem analytical solutions for the correlated many-particle states are unknown and therefore one has to find an adequate analytical or numerical approximation as for example static Hartree-Fock calculations [35, 131, 156]. For the photon subsystem the easiest formalism is the classical treatment in which the electric field is considered as an external field and does not contribute to  $H_0$  at all. In the case of a quantized light field a convenient approach is to choose Fock states [145] to represent the photon subsystem of  $|I\rangle$  and  $|F\rangle$ . Subsequently, after one has obtained the photoionization cross sections, the equation of motion for the occupation numbers of specific electron configurations can be constructed by associating photoionization as increase or decrease in occupation [102, 103, 131]. Additionally, relaxation processes as the Auger effect, shake-off ionization and fluorescence can be included [35, 145].

With respect to coherent quantum dynamics rate equations are the lowest level for modelling the ionization process since they neglect them completely. Nevertheless their applicability on photoionization induced by XUV and X-ray photons has been successfully demonstrated for many experiments [35, 136, 149, 175], even for the novel FEL-sources where the high intensity might not fulfill the requirements of perturbation theory.

### I.3.2. Wave function based methods

This section briefly summarizes wave function based methods which in general solve a TDSE suitable to model photoionization, but are simplified for the numerical realisation. Since these schemes result in a wave function, obviously coherent quantum kinetics are taken into account. Instead, the approximation often affects the interaction and correlation between the electrons carried by the wave function. As illustration two simple well known examples can serve, the single active electron approximation [148] and the time dependent Hartree-Fock (TDHF) method [84]. For the single active electron approximation it is assumed that the electromagnetic field essentially couples with one electron of the atom, whereas all others are unaffected. In this way the many particle wave function has been reduced to a single particle problem. The TDHF approximation represents the wave function by a single Slater determinant constructed with time-dependent single particle orbitals. Thus, correlations between the electrons are neglected and the electron-electron interaction is included on a mean-field level.

In reference [65] a very general formalism to categorize and incorporate many of the commonly used wave function based methods is presented, called the time-dependent restricted-active-space configuration-interaction method. It systematically restricts the

number of Slater determinants by dividing the single particle basis set in partitions and allocates to every partition a minimal and maximal number of allowed particles. The many-particle Hilbert space of the restricted-active-space is spanned by Cartesian products of subspaces corresponding to pairs of a partition and particle number. For a product of subspaces holds that each particle number is in the allowed interval of the respective partition and the sum over all particle numbers of the product is equal to the total particle number. This scheme was originally established in quantum chemistry and extended for a time-dependent treatment of photoionization by the authors of [65]. It includes wave function based approximations as single- and two-active electron methods [75, 148] and time-dependent configuration interaction singles method [49].

Further, the multiconfigurational time-dependent Hartree-Fock [15, 29, 77, 108], time-dependent close-coupling [55] and the time-dependent R-matrix method [20] are recently applied on photoionization dynamics. Wave-function based methods are characterised in being flexible and adjustable to specific scenarios. Furthermore, testing the accuracy of these approaches is quiet convenient since often the wave function can be adjusted in small steps in direction of the exact solution. In this way its possible to verify convergence, as it has been carried out for e.g. the time-dependent multiconfigurational Hartree-Fock scheme [64]. In particular, the ionization dynamics of helium [56, 64], lithium [26, 27] and neon [56, 98, 161] have been investigated with wave-function based methods.

### I.3.3. Reduced many-particle methods

The last introduced class of theoretical methods used for the modelling of photoionization are reduced many-particle methods as the time-dependent density functional theory [142], the non-equilibrium Green's function [12] and the time-dependent reduced density-matrix formalism [147]. They are capable to account for coherent quantum kinetics and electron-electron interaction beyond the mean-field level and, opposed to the wave-function based methods, the computational effort does not critically depend on the number of particles. The time-dependent density functional theory has been successfully applied to the photonionization of atoms, describing the multiple-photon single ionization [165] and the knee-structure in the double ionization yield of helium [91, 162]. Nevertheless, still some open questions remain and are currently discussed. It is known that the commonly applied "adiabatic local density approximation" to the exchange-correlation kernel is not well suited for the treatment of Rabi oscillations [140], double excitations [101, 163] and photon energies beyond the optical regime [162]. However, recent investigations progress in the development of a non-adiabatic treatment [21, 37, 164]. Whereas the time-dependent density functional theory is a well established tool in atomic physics, the non-equilibrium Green's function and the time-dependent reduced density-matrix formalism were originally used for homogeneous many-particle systems. With increasing computational capacities, their application on inhomogeneous system came into reach and first studies were carried out to overcome the limitation of the wave function based methods on small systems [13, 147]. However, the corresponding enormous computational demands limit their application on one-

dimensional model atoms and up to now only a small number of publications concerning atomic photoionization [28, 63, 147] exists. To improve the computational performance a grid-based method has been applied instead of the common representation of the Green's function based on single particle orbitals, achieving first progress [11, 12].



# II

# Applied methods and models

To investigate the influence of quantum coherences and electron-electron correlations on photoionization induced by intensive femtosecond XUV-laser pulses, this work discusses and compares the results of several methods. The most advanced approach presented is the time-dependent density matrix formalism. The corresponding hierarchy of equation will be truncated one level above the time-dependent Hartree-Fock theory and thus also accounts for correlation between the electrons. Furthermore, the time-dependent Schrödinger equation is solved for one and two electrons. As the most simplifying model for the resonant two-photon ionization a "reduced level atom" is analysed, which incorporates the application of the Markov approximation and thereby leads to an analytical result for a harmonic laser excitation. Finally, one has to mention that all methods are applied on a one-dimensional atom model.

## II.1 One-dimensional atom models

One-dimensional atom models have been widely used in theoretical physics to survey the impact of intensive short laser pulses on atoms [51, 53, 74, 96, 97, 154, 159]. Due to the reduction to one dimension they allow the numerical treatment of atomic systems, which in the case of three dimensions would go beyond the computational possibilities. For example in the 90's one-dimensional atom models accessed the exact

solution of the correlated wave function of the time-dependent Schrödinger equation for a two electron atom [53] and also more recently for a three electron atom [141]. Additionally to the exact solution of the time-dependent Schrödinger equation, one-dimensional atom models were also adopted for the implementation of quantum kinetic approaches like the time dependent density functional theory [167], the Green's function approach [12] and the multiconfigurational time-dependent Hartree-Fock theory [63]. The computational requirements of these approaches are already quite demanding in a one-dimensional implementation. The same holds for the time-dependent density matrix formalism adopted in this thesis and motivates the usage of a one-dimensional atomic model [147]. Furthermore the exact numerical solution of the time-dependent Schrödinger equation for laser excited atoms represents an optimal benchmark for results involving further approximations [12, 91]. Of course one-dimensional atom models cannot provide quantitative results reproducible by experiments. Nevertheless they supported the interpretation and explanation of observed physical phenomena. In particular, the important role of electron-electron correlations in the knee-structure of the double ionization yields of helium induced by optical lasers [43, 172] has been manifested by theoretical investigations of one-dimensional atom models [91]. The re-scattering mechanism [94] was identified as the responsible process. One-dimensional atom models also contributed to the prediction of a second Knight doublet [52], which afterwards was confirmed experimentally [171].

For one-dimensional atom models one usually replaces the Coulomb potential. It is known that the Hamiltonian of an electron in a one-dimensional Coulomb potential of a positive charged core has an infinite eigenvalue [97]. To avoid this non-physical situation most publications on one-dimensional atoms utilise the so called "softcore" potential which shares many properties of the real Coulomb potential. For example the softcore potential also decreases with  $\frac{1}{r}$  and possesses near-threshold levels that scale like Rydberg levels. [159]. It is defined as

$$V_{\text{soft}}(x) = -\frac{V_0}{\sqrt{x^2 + \kappa^2}}, \quad (\text{II.1})$$

with the parameters  $V_0$  and  $\kappa$  representing the strength and the range to adjust the potential. In comparison with the real Coulomb potential in  $H_{\text{core-el.}}$  of equation (I.2)  $V_0$  can be interpreted as  $Z \cdot e^2$ . The parameter  $\kappa$  which is necessary to avoid the singularity is usually set equal to one Bohr radius  $a_B$ . With this notation the components of the Hamiltonian for the electrons of a one-dimensional atom read

$$T_{\text{kin}}(x) = -\frac{1}{2m_e} \frac{\partial^2}{\partial x^2}, \quad (\text{II.2a})$$

$$V_{\text{core}}(x) = \frac{-e^2 \cdot Z}{\sqrt{x^2 + a_B^2}}, \quad (\text{II.2b})$$

$$V_{\text{el}}(x - x') = \frac{e^2}{\sqrt{(x - x')^2 + a_B^2}}. \quad (\text{II.2c})$$

The interaction of the electrons with a linearly polarized radiation field is taken into account via the dipole coupling. The polarization axis of the field coincide with the retained single dimension. In this direction the strongest field induced dynamics are expected.

$$H_{\text{field}}(x) = ex \cdot \mathcal{E}(t). \quad (\text{II.3})$$

$\mathcal{E}(t)$  represents the amplitude of the electric field of the laser radiation. The aim of this work is to deal with the dynamics of a model atom evolving under the Hamilton operator  $H$ .

$$H = \sum_{i=1}^N T_{\text{kin}}(x_i) + \sum_{i=1}^N V_{\text{core}}(x_i) + \sum_{\substack{i,j=1 \\ i < j}}^N V_{\text{el.}}(x_i - x_j) + \sum_{i=1}^N H_{\text{field}}(x_i). \quad (\text{II.4})$$

Exceptions are made for calculations with more than one electron which neglect the electron-electron interaction. In this case  $V_{\text{el.-el.}}$  is discarded and  $V_0$  and  $\kappa$  are chosen to realise a screened core potential. Thus, the system exhibits a similar energetic structure and ionization thresholds as the corresponding correlated model.

In addition, another one-dimensional potential is applied to replace the Coulomb interaction between charged particles. It shall be denoted as "cosh-potential" and is given by

$$V_{1d}(x) = \frac{-U_0}{\cosh^2(\alpha x)}. \quad (\text{II.5})$$

In contrast to the softcore potential the cosh-potential is short ranged and does not possess a Rydberg like series of bound states. The parameters  $U_0$  and  $\alpha$  allow the adjustment of the strength and the range of the potential. Its advantage is the known analytic solution of the eigenvalue problem for the stationary single-electron Hamilton-operator [90]. Also the formulas for the matrix elements of momentum operator, position operator and the binary electron-electron interaction can be determined analytically. They are required for an expansion of the wave function or reduced density matrix in the eigenfunctions of the single-electron Hamilton operator.

Because the numerical implementation always implies a finite basis set, usually the system possesses reflecting or periodical boundaries. Concerning the ionization process ejected electrons which reach the boundaries lead to artificial results, in particular when they return to the atom core. In order to avoid this problem absorbing boundaries are introduced for the propagation of the wave function towards large times by the application of complex absorbing potentials [130, 168].

## II.2 Finite-element discrete variable representation

---

For the numerical implementation of the time-dependent Schrödinger equation as well as of the time-dependent reduced density matrix formalism one has to choose a set of

basis functions for the representation of the wave function or the reduced density matrix. In the progression of this thesis, the eigenstates of the stationary field-free single-particle Hamiltonian, the momentum operator and the position operator were considered as basis functions and have been tested according to their numerical performance and stability. The usage of the eigenstates of the stationary Hamiltonian is motivated by the cosh-potential (equ. (II.5)) which provides analytical expressions for the field-free eigenstates and the required matrix elements. The choice of this set of basis functions appears further promising because it allows one to assign the matrix elements of the electron-electron interaction to individual processes [122] and thus enables the transparent application further simplifications and approximations. In particular, this proceeding was supposed to apply for the electron-electron interaction which is the most challenging obstacle in the implementation of the reduced density matrix formalism beyond the Hartree-Fock level. Thus, one would have been able to neglect certain parts of the four-point functions appearing in the equation of motion of the reduced density matrix formalism to reduce the computational demand. However, the calculation is already quite demanding at the Hartree-Fock level of the reduced density matrix formalism in this basis set. The matrix of the electron-electron interaction represents a fully occupied tensor of fourth order. The evaluation of the corresponding terms requires the numerical execution of three summations for each element of the reduced density matrix in the equations of motions. Thus the computation time of the time derivative of the reduced one- and two-particles density matrices in an implicit time propagation scheme scales for  $N_b$  basis functions with  $\propto N_b^5$  and  $\propto N_b^7$ .

To overcome this obstacle, the momentum space as well as the position space have been tested, due to their sparser representation of the matrix of the electron-electron interaction. The momentum space leads to a collapse of one of summations concerning the electron-electron interaction as a consequence of the conservation of momentum. As result the most time expensive contribution for the determination of the interaction between the electrons themselves scales one order lower compared to the representation in the eigenstates of the stationary single-particle states. In addition, the calculation in the momentum space benefits from the diagonal form of the kinetic energy and the momentum operator. As known, plane waves work well for short ranged potentials like cosh-potential (equ. (II.5)) whereas in case of a long ranged softcore potential they lead to a singularity for a momentum equal zero. Another aspect is that the equation of motion can be easily integrated in time by a finite differences scheme if the wave function or the reduced density matrix is represented by plane waves or by the stationary single-particle eigenstates. Instead, in the position space the application of finite differences on time-dependent Schrödinger equation results in a disadvantageous stability condition between the values of the time and space steps [123]. Consequently, the time propagation requires a specific treatment. Nevertheless, the striking argument is given by the sparsest representation of the matrix of the electron-electron interaction in the position space. Bearing this in mind, finally the finite-element discrete variable representation (FEDVR) [126] has been chosen as basis set, which is closely related to the position space and conserves the advantages of the latter. In the FEDRV, strongly localized polynomials defined in finite elements describe the dynamic variable and

provide the connection between neighboured finite elements. Recently, this method is used successfully for several challenging numerical tasks concerning atoms interacting with ultrashort intensive laser pulses. Examples are the solution of time dependent Schrödinger equation for helium in three dimensions [40], the Green's function [11] and the time-dependent multiconfigurational Hartree-Fock method [63, 64]. For numerical applications the FEDVR provides a high accuracy and is substantially more efficient than a finite-difference Numerov method [121]. In particular, the parallel calculation of via large computer cluster is highly supported by the FEDVR [68, 152] and therefore confirms the FEDVR to fit for the task of the present thesis.

In the following a short summary of the properties of the FEDVR is given. The atom shall be placed in a box with the length  $L$  which is divided into  $N_{FE}$  finite-elements:

$$[r^i, r^{i+1}] \quad i = 0 \dots N_{FE} - 1. \quad (\text{II.6})$$

Every finite element includes  $N_{GL}$  Gauss-Lobatto points

$$r^i \leq x_m^i \leq r^{i+1} \quad i = 0 \dots N_{FE} - 1, m = 0 \dots N_{GL} - 1, \quad (\text{II.7})$$

which are defined by the Gauss-Lobatto quadrature rule with the corresponding weights  $w_m^i$ . The Gauss-Lobatto quadrature replaces the integral a summation and is accurate for polynomials up to degree  $2N_{GL} - 3$ .

$$\int_{r_i}^{r^{i+1}} dx g(x) \approx \sum_{m=0}^{N_{GL}-1} g(x_m^i) w_m^i. \quad (\text{II.8})$$

In contrast to the Gaussian quadrature the first and the last point of the Gauss-Lobatto quadrature lies on the boundaries of the integral. In the unit interval  $[-1, 1]$  the remaining points of the Gauss-Lobatto quadrature rule are determined by the zeros of the first derivative of the Legendre polynomial  $P_{N_{GL}-1}(x)$  of order  $N_{GL} - 1$ . The weights in the unit interval are given by the following formula.

$$w_m = \frac{2}{n(n-1)(P_{N_{GL}-1}(x_m))^2}. \quad (\text{II.9})$$

The points  $x_m$  and weights  $w_m$  of the unit interval are mapped on  $x_m^i$  and  $w_m^i$  of the finite elements via

$$x_m^i = \frac{1}{2}((r^{i+1} - r^i)x_m + r^{i+1} + r^i), \quad (\text{II.10a})$$

$$w_m^i = \frac{w_m}{2}(r^{i+1} - r^i). \quad (\text{II.10b})$$

The basis functions are constructed with the Lobatto shape functions  $f_m^i(x)$  which are defined by the Lagrange polynomial [105]. The latter interpolates a function equal one at  $x_m^i$  and equal zero at the remaining Gauss-Lobatto points of the finite element.

$$f_m^i(x) = \begin{cases} \prod_{l \neq m} \frac{x - x_l^i}{x_m^i - x_l^i} & \text{for } x \in [r^i, r^{i+1}] \\ 0 & \text{else.} \end{cases} \quad (\text{II.11})$$

Adopting the quadrature rule for the integration in scalar products leads to the orthogonality of the functions. For an integrand containing a Lobatto shape function the property

$$f_m^i(x_{m'}^i) = \delta_{i,i'} \delta_{m,m'}, \quad (\text{II.12})$$

is essential for the usage of the quadrature rule. Now, the normalized set of basis functions of the FEDVR is built with the help of the Lobatto shape functions.

$$\chi_m^i = \frac{f_m^i(x)}{\sqrt{w_m^i}} \quad \text{with} \quad m = 1 \dots N_{GL} - 2 \quad i = 1 \dots N_{FE} - 1, \quad (\text{II.13a})$$

$$\chi_0^i = \frac{f_{N_{GL}-1}^i(x) + f_0^{i+1}(x)}{\sqrt{w_{N_{GL}-1}^i + w_0^{i+1}}} \quad \text{with} \quad i = 0 \dots N_{FE} - 2. \quad (\text{II.13b})$$

The functions  $\chi_m^i(x)$  only exist in one finite element whereas the bridge-functions  $\chi_0^i(x)$  connect two neighbouring finite elements. In the next step, the operators  $V_{\text{core}}(x)$  (eq. (II.2)) and  $H_{\text{field}}(x)$  (II.3)) for the one-dimensional model atom have to be expressed by the FEDVR basis set. Due to the strong localization of the basis functions in the position space local operators keep their diagonal form, if the quadrature rule (II.8) and equation (II.12) are applied for the respective integrals. Combining a pair of indices  $(i, m)$  in one index  $n$ , the following formulas are received for the one particle operators of the core potential  $V_{\text{core}}(x)$  (eq. (II.2b)) and the electric field  $H_{\text{field-el.}}(x)$  (eq. (II.3)).

$$V_{n_1, n_2}^{\text{core}} = \int dx \chi_{n_1}(x) V_{\text{core}}(x) \chi_{n_2}(x) = \delta_{n_1, n_2} V_{n_1}^{\text{core}}, \quad (\text{II.14})$$

$$H_{n_1, n_2}^{\text{field}} = \int dx \chi_{n_1}(x) H_{\text{field}}(x) \chi_{n_2}(x) = \delta_{n_1, n_2} H_{n_1}^{\text{field}}, \quad (\text{II.15})$$

$$\text{with} \quad V_{n_1}^{\text{core}} = V_{\text{core}}(x_{n_1}) \quad \text{and} \quad H_{n_1}^{\text{field}} = H_{\text{field}}(x_{n_1}).$$

For the two particle interaction  $V_{\text{el.-el.}}(x - x')$  the representation in the FEDVR basis set leads also to a diagonal form.

$$\begin{aligned} V_{n_1, n_2, n_3, n_4}^{\text{el.}} &= \int dx \int dx' \chi_{n_1}(x) \chi_{n_2}(x') V_{\text{el.}}(x - x') \chi_{n_3}(x) \chi_{n_4}(x') \\ &= \delta_{n_1, n_3} \delta_{n_2, n_4} V_{n_1, n_2}^{\text{el.}} \quad \text{with} \quad V_{n_1, n_2}^{\text{el.}} = V_{\text{el.}}(x_{n_1} - x_{n_2}). \end{aligned} \quad (\text{II.16})$$

The diagonal form of this operators is a great advantage in the numerical implementation. More care is needed for the operator of the kinetic energy  $T_{n_1, n_2}^{\text{kin}}$ , because the derivatives of the basis functions are not continuous [126]. Since the basis functions are polynomials, the formulas of the matrix elements of the kinetic energy are simple analytic expressions. One receives a sparse block diagonal structured matrix which is explicitly given in [11, 152] and supports the adoption of a parallel implementation.

## II.3 Time-dependent Schrödinger equation

The exact description of the ionization dynamics evolving under the defined one-dimensional Hamiltonian  $H$  (eq. (II.4)) is obtained via the solution of corresponding TDSE. However, for practical reasons the number of electron has to be small enough to ensure that the numerical requirement is still feasible by the computational capacities. To verify the results obtained with approximative approaches and to explore their validity the solution of the one-dimensional TDSE equation has been determined for the one and two electron Hamiltonian  $H$ . The solution for one or two electrons without  $H_{\text{el}}$  is preferentially compared with approximations concerning the coherent properties of the ionization as it is the case for rate equations and in the generic model defined in section II.5. For an atom with two interacting electrons the solution of TDSE takes the correlation completely into account. Thus, the TDSE represents a benchmark for the investigation of electron-electron correlations.

A split operator method [14, 41, 93, 123] was choose out of the large number of existing time propagation schemes for the TDSE. In this method the time propagation operator  $U(H(t), dt)$  acts successively for small time steps  $dt$  on the wave function.

$$|\Psi(t + dt)\rangle = U(H, t, dt)|\Psi(t)\rangle, \quad (\text{II.17})$$

$$\text{with } U(H(t), dt) = \exp(-iH(t)dt/\hbar). \quad (\text{II.18})$$

During the small time step, it is assumed that the Hamiltonian  $H(t)$  is constant and the time dependence enters only parametrically at each time step. The propagation operator  $U(H(t), \delta t)$  is determined by dividing  $H$  into a time independent and a time dependent part ( $H_1$  and  $H_2(t)$ ).

$$U(H_1 + H_2(t), dt) \approx U\left(H_1, \frac{dt}{2}\right)U(H_2(t), dt)U\left(H_1, \frac{dt}{2}\right) + O(dt^3). \quad (\text{II.19})$$

In the framework of the present task  $H_1$  and  $H_2(t)$  shall be identified in the following manner:

$$H_1 = H_{\text{kin}} + H_{\text{core}} \quad \text{and} \quad H_2(t) = H_{\text{el}} + H_{\text{field}}(t). \quad (\text{II.20})$$

With representation of the wave function through the FEDVR basis this approach allows an efficient numerical implementation. The determination of the exponential operator requires the diagonal form of the underlying Hamiltonian. Therefore the separation of  $H$  should result in a time-dependent part  $H_2(t)$ , which is already diagonal in the FEDVR basis set. Since this requirement is fulfilled by  $H_{\text{el}}$  and  $H_{\text{field}}$  the exponential matrix can be easily determined at each time step without solving the corresponding eigenproblem. Instead, a diagonal form of the time-independent part  $H_1$  in the FEDVR basis set is not needed. Only at the start of the propagation the sparse matrix containing the kinetic energy and the core potential must be diagonalized. For a small time step the

corresponding time propagation operator is represented by a sparse matrix. Further, the parts of operators  $H_1$  for the respective electrons commute and the time propagation operator  $U(H_1, \delta t)$  splits into two identical operators, which act on the two different subspaces of wave function, according to the respective coordinate. The time propagation operators support a parallel numerical adoption due to their sparse form.

## II.4 Reduced density matrix formalism

---

The reduced density matrix (RDM) formalism is an established tool for many-particle physics applied for laser excitation of semiconductors and molecules [6, 83, 134] and in the field of nuclear physics [62]. In this thesis it will be tested on the photoionization of atoms by an XUV-laser pulse. To the best of the knowledge of the author only the reference [147] is concerned with this issue. In contrast to this contribution which uses an expansion based on Hartree-Fock orbital, here the FEDVR shall represent the dynamic variables as it has been carried out for the non-equilibrium Green's function approach in the references [11, 12]. The reduced density matrix formalism enables a coherent treatment of the dynamics of the electrons induced by an intense laser pulse and provides a scheme to account for the interaction between the electrons themselves on different levels. Its advantage is that the computational effort does not depend on the particle number which is the obstacle for the direct solution of TDSE for larger atoms. The dynamical variables are the expectation values of normal ordered creation and annihilation operators  $a_j^\dagger$  and  $a_j$ .

$$\rho_{\mathbf{a},\mathbf{b}} = \langle \Psi | a_{\mathbf{a}}^\dagger a_{\mathbf{b}} | \Psi \rangle, \quad (\text{II.21a})$$

$$\rho_{\mathbf{a},\mathbf{b},\mathbf{c},\mathbf{d}} = \langle \Psi | a_{\mathbf{a}}^\dagger a_{\mathbf{b}}^\dagger a_{\mathbf{c}} a_{\mathbf{d}} | \Psi \rangle, \quad (\text{II.21b})$$

$$\rho_{\mathbf{a},\mathbf{b},\mathbf{c},\mathbf{d},\mathbf{e},\mathbf{f}} = \langle \Psi | a_{\mathbf{a}}^\dagger a_{\mathbf{b}}^\dagger a_{\mathbf{c}}^\dagger a_{\mathbf{d}} a_{\mathbf{e}} a_{\mathbf{f}} | \Psi \rangle, \quad (\text{II.21c})$$

⋮

Here, the operators correspond to electrons and therefore fulfil anticommutation rules for Fermions. The bold index  $\mathbf{a}$  is assigned with a pair  $(n_a, \sigma_a)$  consisting of the respective spin  $\sigma_a$  and FEDVR basis function  $n_a$ . The dynamic variables are denoted as two-, four- and six-point reduced density matrix, due to the number of involved operators. An also commonly used naming is reduced one, two and three particle density matrixes where the specification for one particle is often omitted. The equations of motion are obtained through the Heisenberg equation for operators.

$$i\hbar \dot{a} = [a, H]. \quad (\text{II.22})$$

For an atom interacting with a laser the reduced density matrix of the electrons contains a large part of the desired information like the polarisation and the ionization yields. Also the expectation value of the energy according to the Hamiltonian of equation (II.4)

can already be determined with the knowledge of the four-point function without the need for reduced density matrices of higher order. Due to the interaction between the electrons the reduced density matrix formalism does not yield in a closed set of equations for the reduced one particle matrix. Instead, the equations of motion form a hierarchy up to the density matrix for all particles of the system, denoted as Bogolyubov-Born-Green-Kirkwood-Yvon-hierarchy. At each level the hierarchy the corresponding reduced  $n$ -particle density matrix requires the knowledge of reduced density matrix for  $(n + 1)$ -particles. Of course, this hierarchy has to be truncated to comply with the numerical possibilities. To assure a meaningful and controlled condition for the truncation, it is necessary that the reduced variables  $\rho_{a,b,c,\dots}$  are separated in correlated and uncorrelated terms. The uncorrelated terms are constructed with variables of lower order [173]. To this end one uses in case of the four-point function

$$\rho_{a,b,c,d} = \rho_{a,d}\rho_{b,c} - \rho_{a,c}\rho_{b,d} + C_{a,b,c,d}, \quad (\text{II.23})$$

with  $C_{a,b,c,d}$  representing the correlated fraction. The time-dependent Hartree-Fock (TDHF) theory is obtained by using this expression in the equation of motion for the one particle density matrix without correlated contribution  $C_{a,b,c,d}$ . One main issue of the present thesis is the application of the density matrix formalism beyond the Hartree-Fock level to explore its potential for an application on the ultra fast ionization process. Therefore also  $C_{a,b,c,d}$  has to be determined which requires in the present framework a the reconstruction of the six-point fraction. Following a decomposition described in [7, 173] gives

$$\begin{aligned} \rho_{a,b,c,d,e,f} = & \rho_{c,d}C_{a,b,e,f} - \rho_{b,d}C_{a,c,e,f} + \rho_{a,d}C_{b,c,e,f} \\ & - \rho_{c,e}C_{a,b,d,f} + \rho_{b,e}C_{a,c,d,f} - \rho_{a,e}C_{b,c,d,f} \\ & + \rho_{c,f}C_{a,b,d,e} - \rho_{b,f}C_{a,c,d,e} + \rho_{c,d}C_{a,b,e,f} \\ & + \rho_{c,d}(\rho_{b,e}\rho_{a,f} - \rho_{b,f}\rho_{a,e}) - \rho_{c,e}(\rho_{b,d}\rho_{a,f} - \rho_{b,f}\rho_{a,d}) \\ & + \rho_{c,f}(\rho_{b,d}\rho_{a,e} - \rho_{b,e}\rho_{a,d}) + C_{a,b,c,d,e,f}, \end{aligned} \quad (\text{II.24})$$

With these decompositions (equ. (II.23) and (II.24)) one arrives at a closed equation system for the one- and two-particle density matrix if the term  $C_{a,b,c,d,e,f}$ , which carries the contribution of the correlation to the six-point functions, is discarded. Details of the derivation of the equations of motion, the numerical implementation and results are presented in chapter VI.

## II.5 Generic model for Rabi-assisted ionization

---

The influence of coherent quantum mechanics on the ionization process of XUV radiation has been denoted as one issue of this thesis. Rabi oscillations represent a prime example for coherent dynamics which are usually observed in laser driven atoms [57] and quantum dots [124]. With the advent of free electron lasers, which deliver intense

radiation with an high degree of coherence, the excitation of Rabi oscillations with XUV and X-ray photons got into the focus of recent investigations [76, 116, 132, 133, 143, 146]. A photon energy enabling a two-photon ionization most likely additionally induces Rabi oscillations. In the latter, the excitation can be close to the resonance of a transition between the ground state and an excited state. With respect to this situation, a generic model is derived. It describes the Rabi cycling of electrons between the two bound states and gives rise to a single-photon ionization of the upper state, as sketched in figure II.1. In the end, an analytic solution is obtained which requires the following approximations:

1. A reduced number of bound states
2. Neglecting off-resonant transitions
3. The rotating wave approximation
4. The Markov approximation

Even though the derivation uses the one-dimensional Hamiltonian defined in section II.1 the generic model is not limited to one-dimensional atom models and can be extended to three dimensions. For each of the approximations the solutions are calculated numerically in order to identify their respective range of validity and to pinpoint the dominating processes.

The eigenfunctions of the field-free Hamiltonian of the atom are chosen as basis set for the representation of the Hamiltonian  $H$ . It is separated in a set  $\{|n\rangle\}$  of bound states with negative discrete Eigenvalues  $\hbar\omega_n$  and a set  $\{|v\omega\rangle\}$  corresponding to the continuum with positive Eigenvalues  $\omega$ . The index  $v$ , accounts for possible degeneracies of the continuum.

$$\begin{aligned}
H = & \sum_{n=0}^{\infty} \hbar\omega_n |n\rangle\langle n| + \int_0^{\infty} d\omega \sum_v \hbar\omega |v\omega\rangle\langle v\omega| + \sum_{n=0}^{\infty} \sum_{n'=0}^{\infty} \hbar\mathcal{E}(t) \mu_{n,n'} |n\rangle\langle n'| \\
& + \int_0^{\infty} d\omega \int_0^{\infty} d\omega' \sum_{v,v'} \hbar\mathcal{E}(t) \mu_{\omega v, \omega' v'} |v\omega\rangle\langle v'\omega'| \\
& + \sum_{n=0}^{\infty} \int_0^{\infty} d\omega \sum_v \hbar\mathcal{E}(t) \mu_{n, \omega v} |n\rangle\langle v\omega| + \sum_{n=0}^{\infty} \int_0^{\infty} d\omega \sum_v \hbar\mathcal{E}(t) \mu_{n, v\omega}^* |v\omega\rangle\langle n|. \quad (\text{II.25})
\end{aligned}$$

The respective dipole matrix elements are  $\hbar\mu_{n,n'} = \langle n | e^{\sum_{i=0}^N x_i} | n' \rangle$  for two bound states,  $\hbar\mu_{n, \omega v} = \langle n | e^{\sum_{i=0}^N x_i} | v\omega \rangle$  for the coupling to the continuum and  $\hbar\mu_{\omega v, \omega' v'} = \langle v\omega | e^{\sum_{i=0}^N x_i} | v'\omega' \rangle$  within the continuum. The electric field of the laser  $\mathcal{E}(t)$  shall be monochromatic at frequency  $\omega_L$  with an amplitude  $\mathcal{E}_0$ :

$$\mathcal{E}(t) = \theta(t) \mathcal{E}_0 e^{-i\omega_L t} + c.c.. \quad (\text{II.26})$$

Here  $\theta(t)$  is the Heaviside function. In the first approximation step, the number of excited bound states will be reduced by limiting the sum indices  $n$  and  $n'$  to  $N_{\text{exc}}$ . Especially for a strong off-resonant excitation more than one of the excited bound states might play an important role in the ionization process. The time-dependent Schrödinger equation

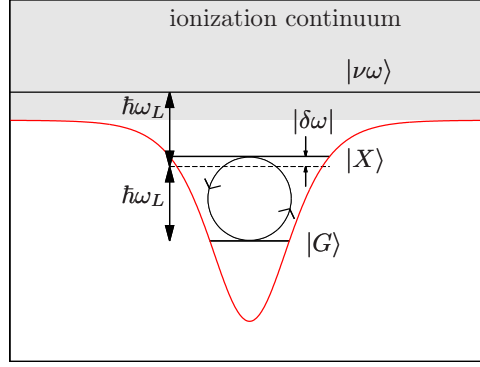


**Figure II.1.:** Schematic illustration of a Rabi-assisted ionization process. The photon energy is close or in resonance to a transition between the initial occupied state  $|G\rangle$  and an excited state  $|X\rangle$  to enable the existence of Rabi oscillations. The situation represents an excitation below the excited states corresponding to  $\delta\omega < 0$ .

defined by the Hamiltonian of equation (II.25) with a limited number of excited states and initially in the ground state will be denoted as "reduced atom". The solution of this approach will be obtained numerically.

The photon energy of the laser can be tuned also close or in resonance to one excited state  $|n_{\text{exc}}\rangle$ . Therefore, in addition to the ground state one bound state  $|n_{\text{exc}}\rangle$ , fulfilling  $\omega_{n_{\text{exc}}} - \omega_0 \approx \omega_L$ , and the continuum are essential to describe the dominating dynamics. In the following the two remaining bound states are denoted as  $|G\rangle$  ( $= |0\rangle$ ) and  $|X\rangle$  ( $= |n_{\text{exc}}\rangle$ ). Furthermore, transitions between the ground state and the continuum and within the continuum will be neglected. The resulting Hamilton operator reads

$$H = \hbar\omega_G|G\rangle\langle G| + \hbar\omega_X|X\rangle\langle X| + \int_0^\infty d\omega \sum_{\nu} \hbar\omega |\omega\nu\rangle\langle \nu\omega| + \mathcal{E}(t) \mu_{X,G}|X\rangle\langle G| \quad (\text{II.27})$$

$$+ \hbar\mathcal{E}(t) \mu_{X,G}^*|G\rangle\langle X| + \int_0^\infty d\omega \sum_{\nu} \hbar\mathcal{E}(t) \mu_{X,\omega\nu}|X\rangle\langle \nu\omega| + \int_0^\infty d\omega \sum_{\nu} \hbar\mathcal{E}(t) \mu_{X,\nu\omega}^*|\nu\omega\rangle\langle X|.$$

It includes the transition of electrons between the ground state and the excited state and between the excited state and the continuum. The wave function shall be represented in the following form:

$$|\Psi\rangle = a_G e^{-i(\omega_G - \delta\omega)t} |G\rangle + a_X e^{-i\omega_X t} |X\rangle + \int_0^\infty d\omega \sum_{\nu} a_{\omega\nu} e^{-i\omega t} |\omega\nu\rangle. \quad (\text{II.28})$$

$\delta\omega = \omega_L - \omega_X + \omega_G$  is the detuning of the laser frequency  $\omega_L$  with respect to the transition between the two bound states. The corresponding time-dependent Schrödinger equation for (II.27) and (II.28) leads to the equations of motion for the coefficients  $a_G$ ,  $a_X$  and  $a_{\omega\nu}$  for  $t > 0$ . It is denoted as "resonant approximation without rotating wave approximation":

$$\dot{a}_G = -i\mathcal{E}_0\mu_{X,G}^* a_X(1 + e^{-2i\omega_L t}) - i\delta\omega a_G, \quad (\text{II.29a})$$

$$\begin{aligned} \dot{a}_X = & -i\mathcal{E}_0\mu_{X,G} a_G(e^{2i\omega_L t} + 1) \\ & -i\mathcal{E}_0 \int_0^\infty d\omega \mu_{X,\omega\nu} a_{\omega\nu} (e^{i(\omega_X - \omega + \omega_L)t} + e^{i(\omega_X - \omega - \omega_L)t}), \end{aligned} \quad (\text{II.29b})$$

$$\dot{a}_{\omega\nu} = -i\mathcal{E}_0\mu_{\omega\nu,X} a_X (e^{-i(\omega_X - \omega + \omega_L)t} + e^{-i(\omega_X - \omega - \omega_L)t}). \quad (\text{II.29c})$$

For solving equation (II.29) the following initial conditions for the coefficients  $a_G$ ,  $a_X$  and  $a_{\omega\nu}$  are implied:

$$|a_G| = 1 \quad a_X = a_{\omega\nu} = 0 \quad \text{for } t < 0. \quad (\text{II.30})$$

In the next step the rotating wave approximation (RWA) will be applied by neglecting all the exponential functions which are assumed to oscillate on a faster time scale than the coefficients  $a_G$ ,  $a_X$  and  $a_{\omega\nu}$ . Consequently, their averaged contribution add up to zero. This case is assumed to apply to  $e^{\pm 2i\omega_L t}$  and  $e^{\pm i(\omega_X - \omega - \omega_L)t}$ . On the contrary, the exponent of  $e^{\pm i(\omega_X - \omega + \omega_L)t}$  passes during the integration through zero. Thus this term evolves on a slow time scale and contributes to the dynamics of  $a_G$ ,  $a_X$  and  $a_{\omega\nu}$ . Taking this considerations into account one arrives at

$$\dot{a}_G = -i\mathcal{E}_0\mu_{X,G}^* a_X - i\delta\omega a_G, \quad (\text{II.31a})$$

$$\dot{a}_X = -i\mathcal{E}_0\mu_{X,G} a_G - i\mathcal{E}_0 \int_0^\infty d\omega \mu_{X,\omega\nu} a_{\omega\nu} e^{i(\omega_X - \omega + \omega_L)t}, \quad (\text{II.31b})$$

$$\dot{a}_{\omega\nu} = -i\mathcal{E}_0\mu_{\omega\nu,X} a_X e^{-i(\omega_X - \omega + \omega_L)t}. \quad (\text{II.31c})$$

The set of equations of motion (eq. (II.31)) is denoted as "resonant approximation" and the solution is obtained numerically. Further simplification can be achieved by integrating the equation of the continuum coefficients (eq. (II.31c)) with the initial conditions (eq. (II.30)).

$$a_{\omega\nu} = -i\mathcal{E}_0\mu_{\omega\nu,X} \int_0^t a_X(t') e^{-i(\omega_X - \omega + \omega_L)t'} dt'. \quad (\text{II.32})$$

The result can be substituted into equation (II.31b) leading to

$$\dot{a}_X = -i\mathcal{E}_0\mu_{X,G} a_G - \mathcal{E}_0^2 \int_0^t d\tau \gamma(\tau, \omega_L) a_X(t - \tau), \quad (\text{II.33a})$$

$$\text{with } \gamma(\tau, \omega_L) = \int_0^\infty d\omega |\mu_{X,\omega\nu}|^2 e^{i(\omega_X - \omega + \omega_L)\tau}. \quad (\text{II.33b})$$

The elimination of the continuum coefficients has led to a closed set of equations for  $a_G$  and  $a_X$  ((eq. II.31a) and eq. (II.33a)) by introducing the memory kernel  $\gamma(\tau, \omega_L)$  (eq. (II.33b)). Transforming them into the Laplace space with respect to the initial conditions (eq. (II.30)) these equations become algebraic. One arrives at

$$a_G(s) = \frac{s + \mathcal{E}_0^2 \gamma(s, \omega_L)}{s^2 + \mathcal{E}_0^2 [s\gamma(s, \omega_L) + |\mu_{X,G}|^2] - i\delta\omega [s + \mathcal{E}_0^2 \gamma(s, \omega_L)]}, \quad (\text{II.34a})$$

$$a_X(s) = \frac{-i\mathcal{E}_0\mu_{X,G}}{s^2 + \mathcal{E}_0^2 [s\gamma(s, \omega_L) + |\mu_{X,G}|^2] - i\delta\omega [s + \mathcal{E}_0^2 \gamma(s, \omega_L)]}. \quad (\text{II.34b})$$

$a_G(s)$ ,  $a_X(s)$  and  $a_{\omega\mu}(s)$  denote the Laplace transforms of the time-dependent functions  $a_G(t)$ ,  $a_X(t)$  and  $a_{\omega\mu}(t)$ . These analytic results (II.34) represent an approximative solution for the time-dependent Schrödinger equation corresponding to the Hamiltonian (eq. (II.25)). The accuracy depends on the validity of the reduced number of bound states and the RWA. For further insight it is preferable to obtain an analytic solution in the time domain. This can be achieved by using the Markov approximation which simplifies the integral over the memory kernel by presuming different time scales for  $a_X$  and  $\gamma(\tau, \omega_L)$ . If the memory kernel decreases on a time scale much faster than changes of  $a_X$  take place, one can approximate  $a_X(t - \tau) \sim a_X(t)$ . For all other values of  $\tau$  the memory kernel  $\gamma(\tau, \omega_L)$  is close to zero and  $a_X$  does not affect the integral.

$$\int_0^t d\tau \gamma(\tau, \omega_L) a_X(t - \tau) \approx \int_0^t d\tau \gamma(\tau, \omega_L) a_X(t) \approx \gamma_0(\omega_L) a_X(t), \quad (\text{II.35a})$$

$$\text{with } \gamma_0(\omega_L) = \int_0^\infty d\tau \gamma(\tau, \omega_L). \quad (\text{II.35b})$$

In the last step also the upper limit of the integral was extended involving only a small error for a fast decaying memory kernel. The Markov approximation implies that the memory kernel in the Laplace space  $\gamma(s, \omega_L)$  loses its dependence on  $s$  ( $\gamma_0(\omega_L) \doteq \gamma(s=0, \omega_L)$ ). This simplifies the transformation of equation (II.34) in the time domain. With the introduction of

$$\tilde{\Omega}_0 = \mathcal{E}_0 \mu_{X,G}, \quad \Gamma_0 = \frac{1}{2} |\mathcal{E}_0|^2 \gamma_0(\omega_L), \quad (\text{II.36a})$$

$$\Gamma^+ = \Gamma_0 + i \frac{\delta\omega}{2}, \quad \Gamma^- = \Gamma_0 - i \frac{\delta\omega}{2}, \quad \tilde{\Omega}^2 = |\Omega_0|^2 - \Gamma^{+2}, \quad (\text{II.36b})$$

and the Markov approximation the results in the Laplace space (II.34) can be rewritten as

$$a_G(s) = \frac{s + \Gamma^-}{(s + \Gamma^-)^2 + \tilde{\Omega}^2} + \frac{\Gamma^+}{\tilde{\Omega}} \frac{\tilde{\Omega}}{(s + \Gamma^-)^2 + \tilde{\Omega}^2}, \quad (\text{II.37a})$$

$$a_X(s) = -i \frac{\tilde{\Omega}_0}{\tilde{\Omega}} \frac{\tilde{\Omega}}{(s + \Gamma^-)^2 + \tilde{\Omega}^2}. \quad (\text{II.37b})$$

The inverse Laplace transformation yields in the analytical solution for the time domain.

$$a_G(t) = e^{-\Gamma^- t} \left( \cos(\tilde{\Omega} t) + \frac{\Gamma^+}{\tilde{\Omega}} \sin(\tilde{\Omega} t) \right), \quad (\text{II.38a})$$

$$a_X(t) = -i \frac{\tilde{\Omega}_0}{\tilde{\Omega}} e^{-\Gamma^- t} \sin(\tilde{\Omega} t). \quad (\text{II.38b})$$

The occupations perform damped Rabi oscillations unaffected by the sign of  $\tilde{\Omega}$ . Obviously, the damping reflects the photoionization. The ionization in the resonant approximation is defined by  $P_I = 1 - |a_G|^2 - |a_X|^2$ . One has to note that the later examined occupation

probabilities  $|a_G|^2$  and  $|a_X|^2$  will oscillate twice as fast as the complex coefficients. The corresponding frequencies shall be

$$\Omega_0 = 2\tilde{\Omega}_0 \quad \text{and} \quad \Omega = 2\tilde{\Omega}. \quad (\text{II.39})$$

Of course, the obtained analytical solution (II.38) contains also the isolated two-level system for a vanishing coupling to the continuum ( $\gamma_0 \rightarrow 0$ ). In this case the Rabi frequency of  $|a_G|^2$  and  $|a_X|^2$  is denoted as

$$\Omega_{2LS}^2 = \Omega_0^2 + \delta\omega^2. \quad (\text{II.40})$$

# III

## Ionization of resonantly driven atomic states

Photoionization pathways which include a resonant coupling between two bound atomic states are predestined to show signatures of coherent quantum dynamics under the intense radiation of recent XFELs. Already the analytic solution of the generic model developed for these conditions in section II.5 predicts Rabi oscillations between the two bound states accompanied by the ionization of the atom. For a detailed investigation of the ionization of resonantly driven atomic states a one-dimensional atom model is applied in the following. In particular, the validity of the approximations of the generic model is verified in the high intensity regime of XFELs by the comparison between different levels of theory. The content of this chapter has been published by the author and co-workers in reference [73].

### III.1 Non-interacting electrons

---

First, the two electron model will be explored without accounting for the interaction between the electrons themselves. In this case the wave function  $\Psi(x_1, \sigma_1; x_2, \sigma_2; t)$  is a single Slater determinant for all times. The resulting Hamiltonian is obtained by neglecting the electron-electron interaction in equation (II.4) and using a different

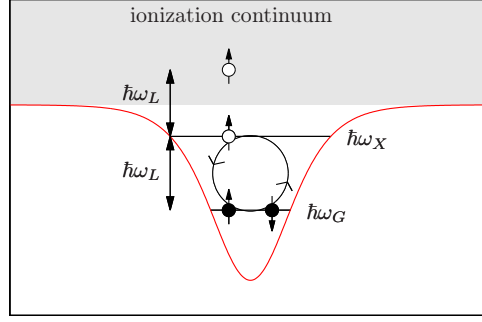


**Figure III.1.:** Schematic view of a two electron atom model with two discrete states performing Rabi oscillations that compete with ionization processes. The lower state is initially occupied and resonantly coupled with the excited state.

parametrization for the softcore potential.

$$H = H_0(x_1) + H_0(x_2) + e(x_1 + x_2) \cdot \mathcal{E}(t), \quad (\text{III.1})$$

$$\text{with } H_0(x) = -\frac{1}{2m_e} \frac{\partial^2}{\partial^2 x} + V_{\text{soft}}(x). \quad (\text{III.2})$$

In order to obtain a similar ionization threshold and transition energy for non-interacting electrons as for the standard parametrization of two interacting electrons (eq. (II.4)) the potential strength is set to  $V_0 = 1.8 E_{Ryd} a_B$  and the potential range to  $\kappa = 0.73 a_B$ . This choice induces  $E_G = -21$  eV and  $E_X = -7$  eV for the two lowest orbitals of the corresponding stationary single particle Schrödinger equation of  $H_0$ . Both orbitals are resonantly coupled by an electric field  $\mathcal{E}(t)$  with  $\hbar\omega_L = E_X - E_G$ .

$$\mathcal{E}(t) = \theta(t) \mathcal{E}_0 e^{-i\omega_L t} + c.c.. \quad (\text{III.3})$$

The system shall initially occupy the ground state, leading to a spin singlet state.

$$\Psi(x_1, \sigma_1; x_2, \sigma_2; t) = \varphi(x_1, t) \varphi(x_2, t) \frac{(\delta_{\sigma_1 \downarrow} \delta_{\sigma_2 \uparrow} - \delta_{\sigma_1 \uparrow} \delta_{\sigma_2 \downarrow})}{\sqrt{2}}. \quad (\text{III.4})$$

The orbital  $\varphi(x, t)$  is determined by the solution of the time-dependent Schrödinger equation for a single particle.

$$i\hbar \frac{\partial}{\partial t} \varphi(x) = (H_0(x) + ex \cdot \mathcal{E}(t)) \varphi(x), \quad (\text{III.5})$$

which is solved numerically without any further approximations. At this point one has to recall that the generic model developed in section II.5 for  $\delta\omega = 0$  delivers an approximated solution for the time-dependent Schrödinger equation (III.5). For the adoption of the analytic solution the energetically lowest single particle eigenstate of  $H_0(x)$  takes the place of the state  $|G\rangle$  and the second energetically lowest orbital is interpreted as the excited state  $|X\rangle$ . The simplicity of the analytic results allows to analyse the damped Rabi oscillations. The damping represents the ionization of the atom

and is mainly determined by  $\Gamma$ . This contribution scales proportional to  $|\mathcal{E}_0|^2$  which is usually interpreted as a single-photon ionization according to lowest order perturbation theory. However, the ionization of the ground state via a single-photon absorption is not included in the approximations made for the analytic solution (II.38). Instead, a two-photon absorption is necessary to eject one electron which results in a scaling  $\propto |\mathcal{E}_0|^4$  in leading order perturbation theory. This prediction is no contradiction to the derived analytic results which reflects the perturbation behaviour during the first Rabi cycle for  $\Omega t \ll \pi$ . In this regime the electrons are transferred from the ground state to the excited bound state and finally to the continuum. For later times an oscillatory exchange of the electrons between the two bound states sets in, which cannot be captured by leading order perturbation theory. A further contribution to the damping of the Rabi oscillations stems from the complex value of  $\Gamma$ . Determining  $\Omega$  by taking the root of  $|\Omega_0|^2 - \Gamma^2$ , obviously  $\Omega$  is real for  $\Gamma = 0$  but in general picks up a finite imaginary part for  $\Gamma \neq 0$ . The finite value  $\text{Im}(\Omega)$  induces additionally exponentially components on the cosine and sinus functions and thus also contributes to the damping. Furthermore, the equations (II.36) predict a deviation of the Rabi frequency  $\Omega$  from the value  $\Omega_0$  in the isolated two level system.

Using the single particle orbitals of  $H_0$  the required dipole moment  $\mu_{X,G}$  and the memory kernel  $\gamma(\tau)$  are calculated. With these values at hand the solution of the Markov approximation for the coefficients  $a_G$  and  $a_X$  is fully determined. In addition also the resonant approximation (eq. (II.31)) is solved numerically. Compared with the exact solution of the time-dependent Schrödinger equation the resonant approximation invoked several simplifications specified in section II.5. These were the reduction to two bound states, the negligence of transitions between the ground state and the continuum states, the omission of the coupling between continuum states themselves and the rotating wave approximation.

Figure III.2 shows the ground state occupation of the two electron atom as a function of time for three different intensities. The direct numerical solutions of equation (III.5) (blue solid line) are compared with results provided by the generic model. The red dashed curve represents numerical results of the resonant approximation and the dotted green curve is given by the analytic solution obtained via the Markov approximation. At the lowest applied intensity of  $I = 3.52 \cdot 10^{12} \text{ W/cm}^2$  (fig. III.2 (a)) all three approaches quantitatively coincide and the ground state occupations perform damped Rabi oscillations. As expected for increasing intensity the results at  $I = 1.27 \cdot 10^{14} \text{ W/cm}^2$  in figure III.2 (b) exhibit faster oscillations and a stronger damping. Also first deviations between the exact numerical solution and the approximations of the generic model appear. The result of the complete time-dependent Schrödinger equation has a slightly stronger damping representing a higher ionization. But still in all three curves of figure III.2 (b) the Rabi periods coincide and the influence of the Markov approximation is not noticeable. However, the situation changes drastically for  $I = 1.41 \cdot 10^{15} \text{ W/cm}^2$  shown in figure III.2 (c). In this case the results of the generic model underestimate the damping and reveal faster oscillations. Nevertheless, it is remarkable how close both curves of the generic model are to each other and instead deviate much stronger from the exact solution.

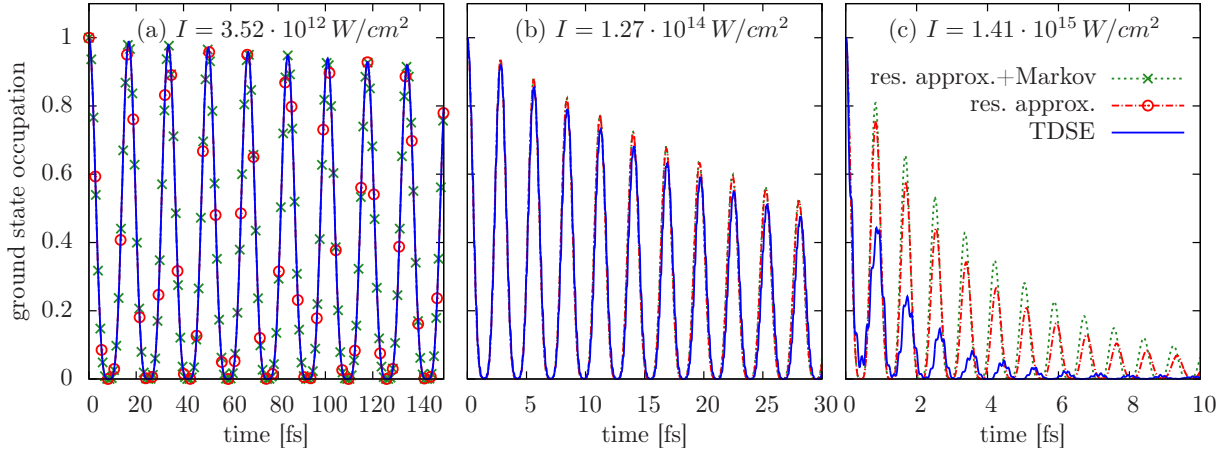


**Figure III.2.:** Ground state occupation for two non-interacting electrons as a function of time for three intensities. Three levels of theory are displayed: The direct numerical solution of the Schrödinger equation (blue solid line) and the generic model, first accounting only for resonant contributions (red dashed dotted line or circles) and second including additionally the Markov approximation (green dotted line or crosses).

The results of the generic model qualitatively capture most of the features of the complete numerical solution, but fail quantitatively in the high intensity regime. Evidently, under these conditions the assumptions of the approximations applied in the generic model are not valid any more. It is close at hand that the negligence of the direct dipole coupling between the ground state and the continuum as well as the complete omission of further bound states decrease the number of possible ionization paths. In the same manner acts the RWA by keeping only resonant terms in the equations of motion. It is, however, amazing how strong these non-resonant contributions increase the ionization although the excitation is Fourier-limited and therefore spectrally narrow.

## III.2 Interacting electrons

In the following the discussion is extended to the dynamics of interacting electrons. The corresponding Hamiltonian is defined in equation (II.4) with  $N = 2$  electrons using the standard parametrization for the softcore potential. Figure III.3 (a) shows the ground state occupation probability as a function of time for two intensities. As before, the ground state occupation performs damped Rabi oscillations. The damping and frequency of the Rabi oscillations increase with rising intensity. For a detailed quantitative comparison with the results of non-interacting electrons the Fourier transforms of the time traces are performed. The spectra are shown in figure III.3 (b) and (c) and have a rich structure that differs for calculations with and without interaction between the electrons. In both cases the Rabi oscillations in the time domain correspond to the dominating peak. Its position shall be denoted as  $\Omega_R$ . First, one recognizes the different

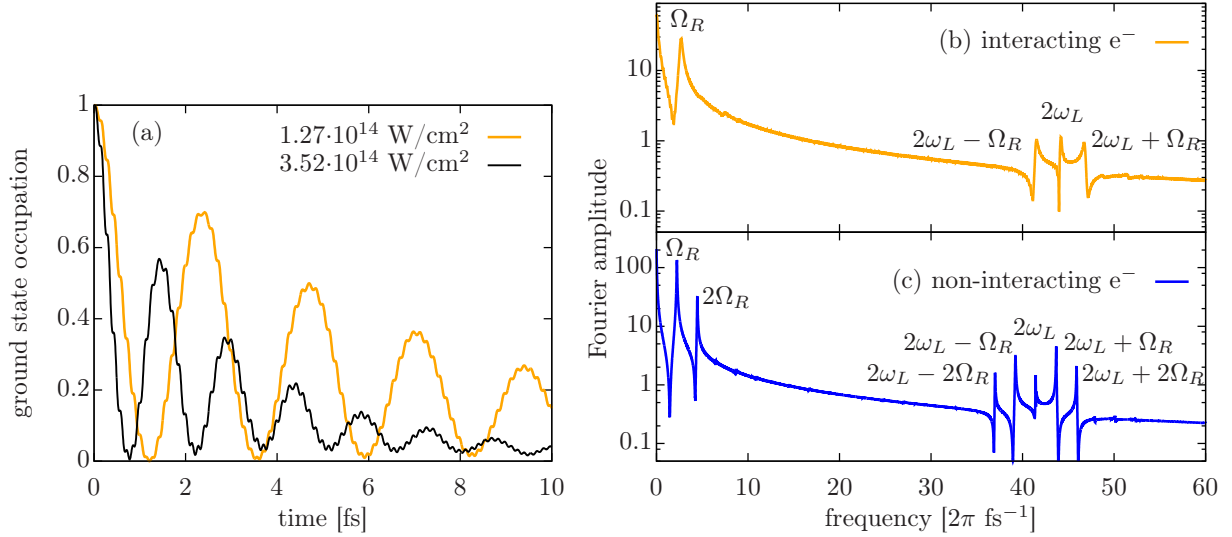


**Figure III.3.:** Figure (a) shows the ground state occupation for a system of two interacting electrons obtained by the exact solution of the Schrödinger equation for two intensities as indicated. The right panel displays the Fourier transformations of the ground states dynamics for  $I = 1.27 \cdot 10^{14} \text{ W/cm}^2$  with (b) and without electron-electron interaction (c).

values of  $\Omega_R$  for interacting and non-interacting electrons due to slightly different dipole couplings between the ground state and the excited state. Furthermore, both spectra exhibit peaks at  $2\omega_L$  and  $2\omega_L \pm \Omega_R$  corresponding to counter-rotating contributions which are usually neglected by the rotating wave approximation (e.g. see equation (II.29)). The spectrum corresponding to the dynamics of non-interacting electrons includes additional peaks at  $2\Omega_R$  and  $2\omega_L \pm 2\Omega_R$ . Formally, they are generated by the product of the two single particle orbitals constructing the Slater determinant. Therefore the probability of the two particle ground state is given by the absolute fourth power of the occupation of the lowest single particle orbital leading to the observed higher harmonics.

In addition to  $\Omega_R$  also the ionization rate represented by the damping of the Rabi oscillations can be extracted out of the spectrum. It shall be denoted as  $\Gamma_R$  and is determined by the Full-Width-at-Half-Maximum of the peak at  $\Omega_R$ . In figure III.4 the intensity dependence of  $\Gamma_R$  and  $\Omega_R$  is displayed for calculations with and without electron-electron interaction. Besides,  $\Gamma_R$  and  $\Omega_R$  are extracted for the generic model corresponding to non-interacting electrons invoking the resonant approximation with and without the Markov approximation. For all approaches  $\Gamma_R$  starts to rise linearly for low intensities. However, at high intensities a super linear intensity dependence is found for almost all levels of theory. Only in the case of the Markov approximation  $\Gamma_R$  rises linearly in the whole applied intensity range. In particular the deviation from the linear intensity dependence of  $\Gamma_R$  is most pronounced for the direct solution of non-interacting particles whereas the resonant approximation only differs less from the behaviour of the analytic solution. For the interacting particles the extracted damping rate exceeds the ones of all other approaches. Figure III.4 (b) displays the intensity dependence of  $\Omega_R$  normalized to  $\Omega_0$ . With rising intensity the renormalized value of  $\Omega_R$  decreases

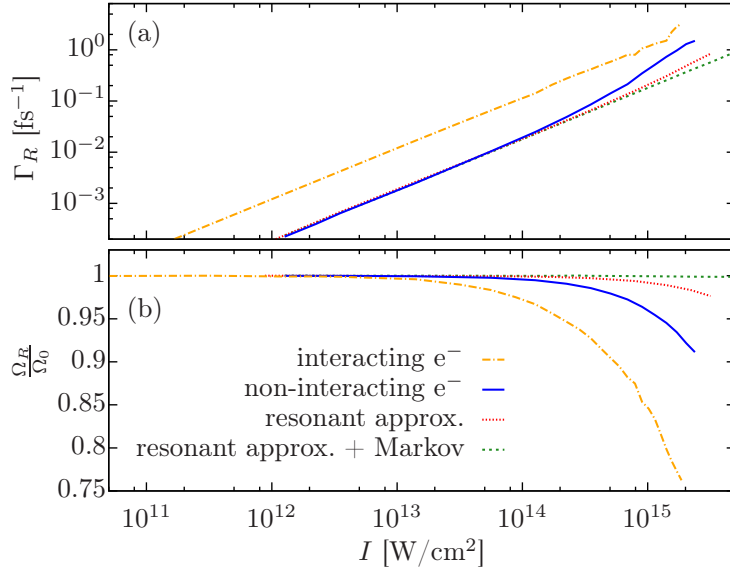


**Figure III.4.:** Intensity dependency of the damping (a) and the Rabi frequency (b). The latter is normalized to the Rabi frequency expected for an isolated two-level system. Results are displayed for a two-electron system obtained by the exact solution of the Schrödinger equation with (orange dashed dotted lines) and without (solid blue lines) electron-electron interaction. For non-interacting electron  $\Gamma_R$  and  $\frac{\Omega_R}{\Omega_0}$  are also obtained via the generic model using the resonant approximation (red dotted lines) and the Markov approximation (green dashed lines).

and reveals together with figure III.4 (a) the relation between  $\Omega_R$  and  $\Gamma_R$ . One can clearly see that high ionization rates are accompanied by a reduced Rabi frequency  $\Omega_R$  according to the value  $\Omega_0$  of an isolated two-level system. It is also remarkable that for the Markov approximation  $\Omega_R$  does not visibly deviate from  $\Omega_0$  even though the renormalization of the Rabi frequency is manifested in the analytic solution (eq. (II.36)). Instead non-Markovian dynamics are necessary to induce a sufficient ionization for an appreciable renormalization. This observation is further supported by the direct solution of the Schrödinger equation for non-interacting particles. Here, as already mentioned above, additional off-resonant ionization paths contribute at high intensities and result in a further reduction of  $\Omega_R$  compared to the resonant approximation. In the case of interacting electrons, the strongest renormalization is found at an intensity of  $I \gtrsim 10^{15} \text{ W}/\text{cm}^2$ . There  $\Omega_R$  decreases to  $\sim 75\%$  of its renormalized value.

### III.3 Impact on the ionization dynamics

Of course, the degree of ionization is not directly influenced by the specific population of bound atomic states and does not differ between electrons which are either in the excited bound state or in the ground state. Nevertheless, it is obvious that in the recent scenario an excited state is ionized by absorbing only one photon where in contrast two

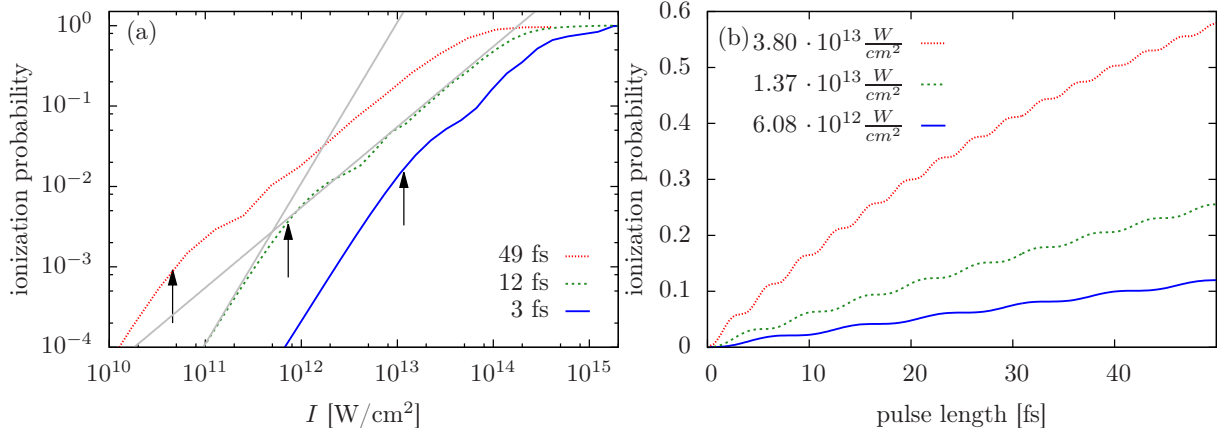


**Figure III.5.:** Ionization probability of the model atom with two non-interacting electrons. (a): As a function of the intensity  $I$  for three finite pulse durations. (b): As a function of the pulse length for three intensities. The grey lines in (a) mark a strict linear or quadratic intensity. The arrows indicate the intensity corresponding to pulse area of  $A = \pi$ .

photons are needed to eject one electron out of the ground state. Thus, in this section the ionization of the model system is analysed with respect to a temporal finite excitation and its temporal evolution. The ionization probability  $P_I$  is for this propose defined as

$$P_I = 1 - P_{bound}, \quad (\text{III.6})$$

with the probability  $P_{bound}$  for both electrons occupying bound states. Thus,  $P_I$  includes single and double ionization.

Figure III.5 (a) displays the  $P_I$  for different durations of square pulses calculated for the non-interacting electrons. The results of all three pulse durations exhibit a transition between two different regimes marked by the arrows. On the right side of the arrows the ionization grows almost linearly with the intensity and is slightly modulated by small oscillations. This behaviour coincides with the observations of the previous section. There, the damping of the Rabi oscillations represented the ionization rate and also scaled linearly with the intensity. In addition  $P_I$  is also influenced whether the respective pulse area leads to an averaged higher occupation of either the ground or of the excited state leading to the small modulations of the ion yield. On the contrary a quadratic intensity scaling is found at the left side of the arrows as expected for the second order perturbation theory. It is close at hand that the transition between different regimes of ionization indicated by the position of the arrows is related to the onset of the first Rabi oscillation. Precisely, the arrows mark the intensity of a pulse area  $A = \pi$  for each individual pulse, corresponding to a half Rabi cycle. On the left side of the arrows ( $A < \pi$ ) the ionization probability rises quadratically and monotonically with intensity. In this regime the occupation of the excited bound state only rises during the pulse without being transferred back to the ground state. Subsequently, an electron of the excited bound state is passed to the continuum. For such a two-step process the lowest order perturbation theory predicts a quadratic intensity scaling of the ion yield which coincides with the present observation. Furthermore, this characteristic intensity dependence is

also captured by the generic model.  $P_I$  can be expressed with the help of the analytic solution and expanded with respect to  $\mathcal{E}_0$ . The leading order term in  $\mathcal{E}_0$  verifies  $P_I \propto I^2$  at low intensities. The relation between the modulations superimposed for  $A > \pi$  (fig. III.5 (a)) and the Rabi oscillations can be accessed more directly in figure III.5 (b). There the ion yields are plotted as a function of the pulse duration for three intensities and reveal signatures of the alternating occupation of the two coupled bound states. A stepwise increase of the ionization only occurs while the excited state is significantly occupied. The increasing frequency of the modulations with rising intensity further confirms the relation to Rabi cycles.

Even though figure III.5 manifests that measurable quantities are affected by Rabi oscillations the experimental realisation is still challenging since the properties of the pulses emitted by XFEL lasers strongly fluctuate. The pulse shape as well as the peak intensities vary during the operation and the emittance of squared pulses is at this moment out of reach. In particular the appearance of the Rabi oscillations in the ion yields as a function of time is not feasible at the moment. More promising for an experimental realisation appears the transition between the quadratic and linear intensity scaling of the ion yields. First measurements at SACLA [146] confirmed a linear intensity scaling for photon energies resonant to the  $1s^2$  and  $1s2p$  states of helium although the crossover was not observed. In addition theoretical investigations [143] determined the influence of the fluctuating XFEL pulse properties on the intensity dependence of the ion yields and found that the transition between a quadratic and a linear intensity scaling could still be observed.

# IV

## Ionization of off-resonantly driven atomic states

In the following, the analysis is extended to photon energies inducing ionization pathways with off-resonantly driven transitions between atomic bound states. The knowledge of this situation is of importance since in experiments the photon energy might slightly deviate from the resonance condition. In order to evaluate the stability of the features induced by Rabi oscillations of chapter III, a detuning between the laser and the resonance frequency should be considered. Furthermore, ionization paths including excited states can also contribute to the ionization process induced by XFELs. Even though the laser frequency is above the first ionization threshold of the neutral target atom, the binding energy of the bound electrons in subsequently produced ions increases with the charge state of the ions and possibly exceeds the photon energy [136, 137]. When the ions are no longer ionized by a single-photon absorption, the photon energy might be close to a transition energy between excited ion states. Thus, the ionization via off-resonantly driven atomic states can occur at a later point in the interaction between the radiation and the atom.

Depending on the photon energy, the discussion can be divided into two different regimes as illustrated in figure IV.1. For a negative detuning  $\delta\omega < 0$  (fig. IV.1 (a)), which

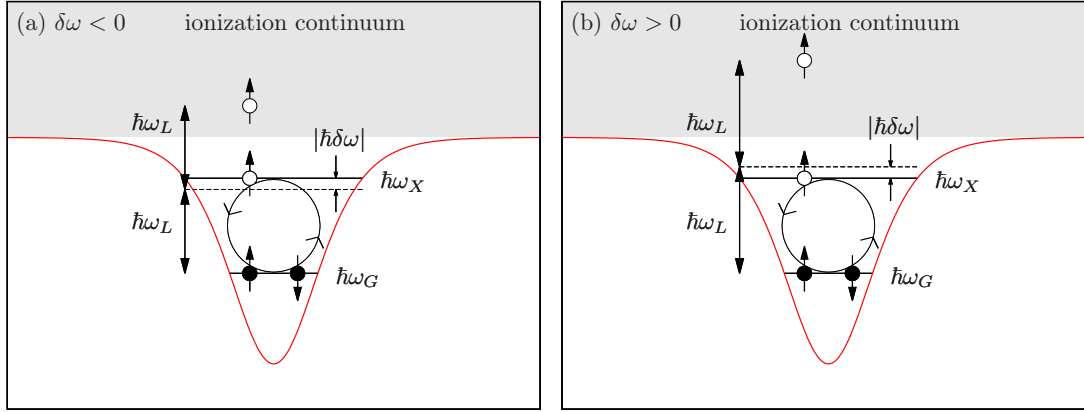


**Figure IV.1.:** Schematic view of the generic model of section II.5 applied on a two electron atom for negativ (a) and positive (b) detuning.

implies  $\omega < \omega_X - \omega_G$ , the photon energy is smaller than the transition energy between the ground state and the first excited state, but still sufficient to ionize the ground state via a two-photon absorption. In the other case, for a positive detuning  $\delta\omega > 0$  (fig. IV.1 (b)), a single-photon excitation of the ground state reaches above the first excited state. For  $\delta\omega < 0$  the reduction of the atom to two bound states and a continuum may be still justified whereas for  $\delta\omega > 0$  further excited bound states are probably involved in the ionization dynamics for sufficient larger detunings.

The one-dimensional two electron atom applied in chapter III for a resonant laser excitation is investigated using the different levels of the generic model as well as the complete TDSE. In this manner one can systematically pinpoint the contribution of the involved processes. At first, the analytic solution of the generic model shall be discussed for  $\delta\omega \neq 0$ . In section II.5 one arrived at equations (II.36) and (II.38). As known for the isolated two level system the derived analytic solution for the Rabi-assisted ionization predicts a decrease of the amplitude of the Rabi oscillations for increasing detuning. Therefore in general a complete inversion between the ground state and the excited state is not achieved in a Rabi cycle. An enhancement of the fraction of electrons rotating between the two bound states can be realised with a higher electric field strength of the laser pulse. Interestingly, the results for  $a_G(t)$  and  $a_X(t)$  are not independent on the sign of  $\delta\omega$  in contrast to an isolated two level system since  $\gamma_0$  and therefore  $\Gamma_0$ ,  $\Gamma^+$  and  $\Gamma^-$  are functions of the laser frequency. Usually, rising the laser frequency leads to a smaller ionization cross section for excitations far away from the ionization threshold resulting in a decreasing ionization rate  $\Gamma_0$ . Furthermore, unfolding the obtained expression for the Rabi frequency

$$\tilde{\Omega} = \pm \sqrt{|\tilde{\Omega}_0|^2 + \frac{\delta\omega^2}{4} - \Gamma_0^2 - i\Gamma_0\delta\omega}, \quad (\text{IV.1})$$

reveals an additional influence of the detuning  $\delta\omega$  on the Rabi frequency  $\Omega$  compared to the resonant case. In the latter the renormalization with respect to the Rabi frequency of the isolated two level system was only affected by the term  $\Gamma_0^2$ . The question whether

the renormalization is smaller or larger than one was exclusively answered by the stationary properties of the atom contained in  $\gamma_0$ . The applied model leads to smaller Rabi frequencies compared to the isolated two level system. Due to the last term  $i\Gamma_0\delta\omega$  in equation (IV.1) for an off-resonantly driven atom the sign of the detuning  $\delta\omega$  might induce Rabi cycles rotating slower as well as faster than in the isolated two level system.

Up to now, in this thesis Rabi oscillations have been discussed only between the ground state and the first excited state. In the following discussion of an off-resonantly driven system the appearance of Rabi processes is not restricted to one pair of states. To distinguish several couplings, a Rabi process between the stationary eigenstate  $n$  and  $n'$  of the field free Hamiltonian is characterised by the respective detuning  $\delta\omega^{n\leftrightarrow n'}$  and the frequency  $\Omega^{n\leftrightarrow n'}$ . The Rabi frequency of the corresponding isolated system equation (II.40) is rewritten as

$$\tilde{\Omega}_{2LS}^{n\leftrightarrow n'}{}^2 = \tilde{\Omega}_0^{n\leftrightarrow n'}{}^2 + \delta\omega^{n\leftrightarrow n'}{}^2 \quad \text{with} \quad \tilde{\Omega}_0^{n\leftrightarrow n'} = \mathcal{E}_0\mu_{n,n'}. \quad (\text{IV.2})$$

Quantities without a specification in the superscript belong to ground state and first excited state.

## IV.1 Negative laser detuning

At first the validity of the generic model will be tested for negative detunings at a low intensity. Figure IV.2 shows the time traces of the ground state occupation performing damped Rabi oscillations for detunings of  $\hbar\delta\omega = -0,27$  eV,  $\hbar\delta\omega = -0,82$  eV and  $\hbar\delta\omega = -1,63$  eV at an intensity of  $I = 3,17 \cdot 10^{13}$  W/cm<sup>2</sup>. With a stronger detuning the amplitude of the Rabi oscillations decreases and the Rabi frequency increases, as known for the isolated two level system. Driving the model atom resonantly at a low intensity the previous chapter revealed the quantitative agreement between the Markov approximation (green dotted line and crosses), the resonant approximation (red line) and the complete solution of the time-dependent Schrödinger equation (blue line). On the contrary, for the off-resonant case quantitative small deviations appear between the different levels of theory in the Rabi frequency and in the ionization already at rather low intensities and are growing with increasing detuning. The first Rabi cycles in figure IV.2 (a) indicate a higher Rabi frequency for the results of the solution of the complete Schrödinger equation than for the results of the resonant approximation. This observation holds also for results obtained for the detunings  $\hbar\delta\omega = 0,82$  eV in figure IV.2 (b) and  $\hbar\delta\omega = 1,63$  eV in figure IV.2 (c) and implies a renormalization of the Rabi frequency as found for the resonantly driven system, but in the opposed direction. In addition figure IV.2 (c) exhibits deviations for the ionization rates of the different levels of theory. The averaged ground state occupation during a Rabi cycle decays slightly faster for the solution of the complete TDSE than for the results obtained with the generic model. For a further clarification of this observation the total ionization probability<sup>1</sup>

<sup>1</sup>The calculated ionization probability includes single and double ionization as defined in section III.3

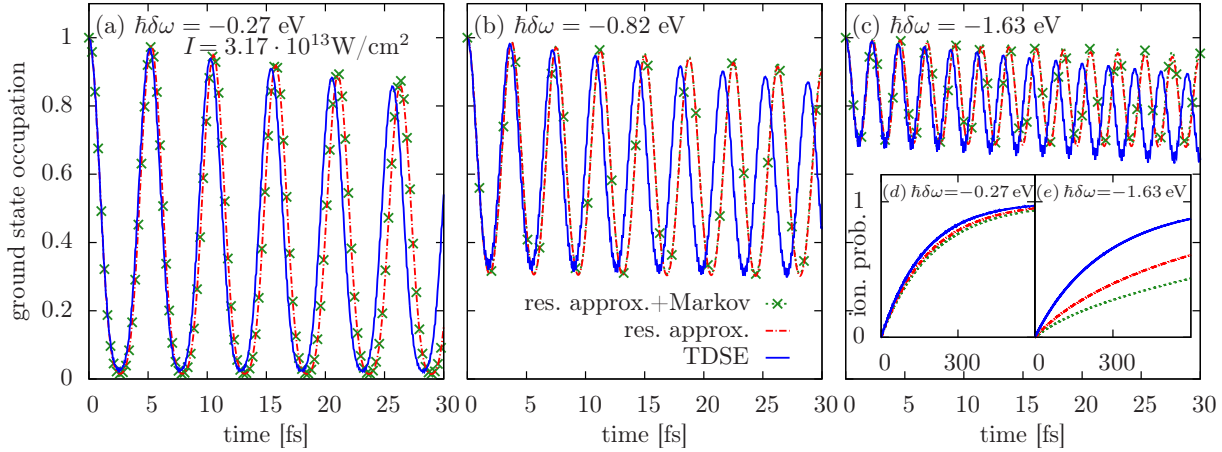


**Figure IV.2.:** Ground state occupation ((a)-(c)) and ionization probability ((d) and (e)) for two non-interacting electrons as a function of time for different detunings at an intensity  $I = 3.17 \cdot 10^{13} \text{ W/cm}^2$ . Three levels of theory are displayed: The direct numerical solution of the Schrödinger equation (blue solid line) and the generic model, first accounting only for resonant contributions (red dashed dotted line) and second additionally including the Markov approximation (green dotted line or crosses).

is displayed as a function of time on a longer time scale, plotted figure IV.2 (d) and (e). For a small detuning of  $\hbar\delta\omega = -0.27 \text{ eV}$  all approaches have roughly the same ionization yields, whereas for  $\hbar\delta\omega = -1.63 \text{ eV}$  the two approximations underestimate the ionization in comparison with the exact solution. In contrast to the resonant excitation conditions for  $\hbar\delta\omega = -1.63 \text{ eV}$  large discrepancies exist also between the resonant approximation with and without the Markov approximation (green and red curve in fig. IV.2 (e)). Interestingly, already for rather low intensities the Markov approximation becomes quantitatively invalid at a high detuning, probably caused by the faster Rabi oscillations. They are degrading the applicability of separated time scales between the memory kernel and the expansion coefficient of the excited state. Making no use of the Markov approximation obviously improves the results but still underestimates the ionization yields.

In figure IV.3 (a) and (b) the ground state dynamics are displayed for a moderate intensity  $I = 1.72 \cdot 10^{14} \text{ W/cm}^2$  and a high intensity  $I = 3.52 \cdot 10^{14} \text{ W/cm}^2$  at a detuning of  $\hbar\delta\omega = -1.63 \text{ eV}$ . The Rabi frequency and the amplitude of the oscillations increase with rising intensity, as known for the isolated two level system and predicted by the analytic solution. It was found above that at a high detuning the resonant approximation and the Markov approximation fail already at the lowest applied intensities. In order to converge further to the exact solution, figure IV.3 additionally contains results of the resonant approximation without the RWA (orange line). It is clearly visible that this step does not significantly alter the results of the ground state occupation compared to the results of the resonant approximation with the RWA. The frequency of the Rabi cycles, their amplitude and the ionization are essentially the same with or without the RWA. Only the fast laser induced oscillations with a very small amplitude are additionally superimposed. Confirming the applicability of the RWA, this observation points to the failure of the

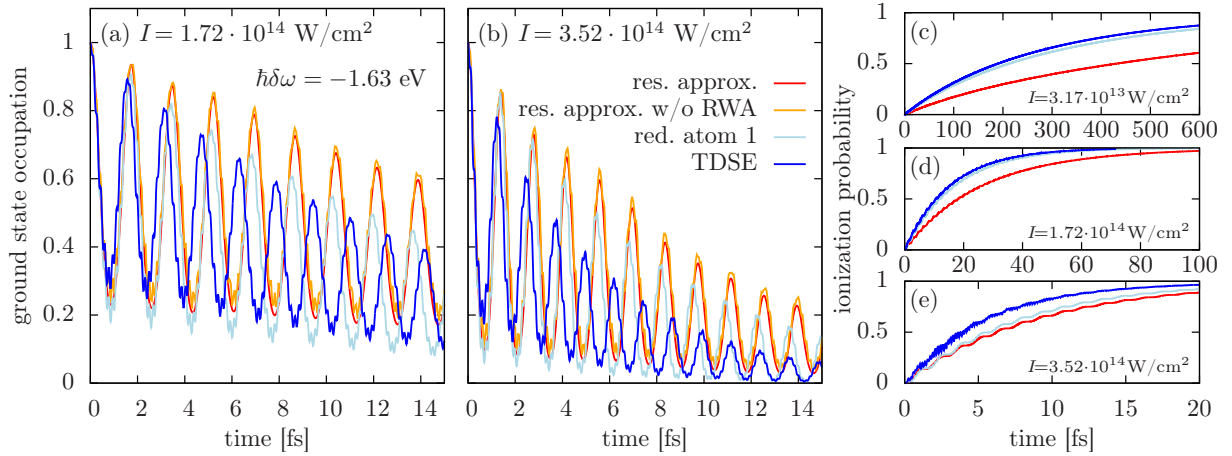


**Figure IV.3.:** Ground state occupation for two non-interacting electrons as a function of time at a detuning of  $\hbar\delta\omega = -1.63$  eV for  $I = 1.72 \cdot 10^{14}$  W/cm<sup>2</sup> (a) and  $I = 3.52 \cdot 10^{14}$  W/cm<sup>2</sup> (b). Plots (d) and (e) show the corresponding ionization probability and in addition also for  $I = 3.17 \cdot 10^{13}$  W/cm<sup>2</sup> (c). Four levels of theory are displayed: The direct numerical solution of the Schrödinger equation (blue line), the reduced atom with one excited single particle orbitals (light-blue line) and the resonant approximation with the RWA (red line) and without RWA (orange line).

remaining simplifications of the resonant approximation. These are the limitation to two bound states and the negligence of transitions between the ground state and continuum states and between continuum states themselves.

In order to identify the failing approximation the ensemble of different levels of theory will be extended by the "reduced atom" (eq. (II.25)). The reduced atom includes all possible transitions for the ground state, the first excited state and the continuum. In figure IV.3 the corresponding results are represented by the light-blue curves. The time evolution of the ionization probability show an excellent agreement with the numerically exact solution of the time-dependent Schrödinger equation at  $I = 3.17 \cdot 10^{13}$  W/cm<sup>2</sup> and  $I = 1.72 \cdot 10^{14}$  W/cm<sup>2</sup> (fig. IV.3(c) and (d)). This observation manifests a non negligible contribution of the direct coupling between the ground state and the continuum at a low intensity, enabling a direct two-photon ionization. As long as the applied intensity is low and therefore the Rabi oscillations do not completely deplete the ground state, the direct two-photon ionization also contributes in addition to the Rabi-assisted ionization. Therefore at an intensity of  $I = 3.52 \cdot 10^{14}$  W/cm<sup>2</sup> (fig. IV.3 (e)) the influence of the direct two-photon ionization decreases, as confirmed by the similar ionization dynamics of the reduced atom and the resonant approximation. The remaining deviations between both approximations and the complete solution of the TDSE in Figure IV.3 (e) are due to the growing importance of off-resonant ionization pathways in the high intensity regime. Although the reduced atom with one excited single particle orbital reproduces ionization yields at low and intermediate intensities, differences still occur in the time traces of the ground state occupation. In the results presented in figure IV.3 (a) and (b) for the reduced atom, the Rabi cycles rotate still slower than for the complete TDSE.

To investigate the influence of the further bound states, figure IV.4 displays results

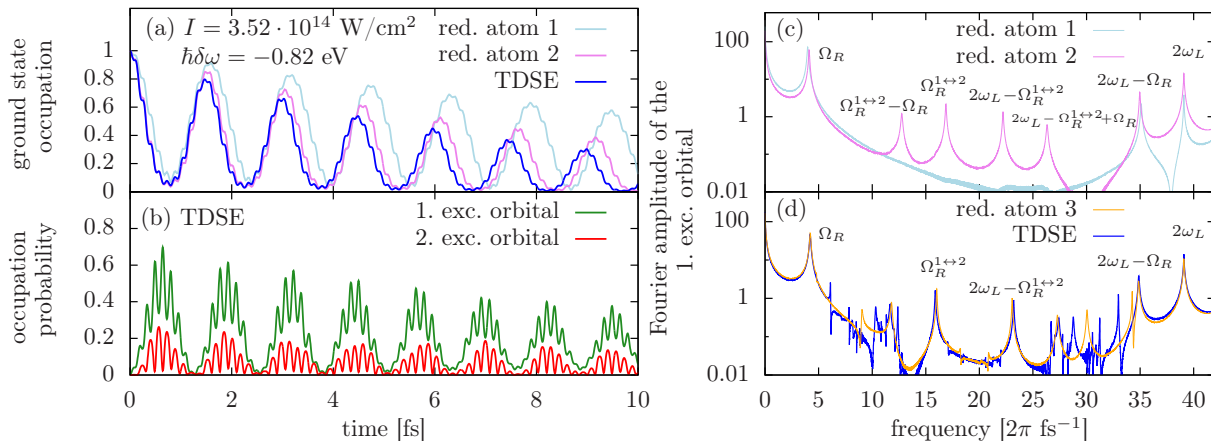


**Figure IV.4.:** Results at an intensity  $I = 3.52 \cdot 10^{14} \text{ W/cm}^2$  and a detuning  $\hbar\delta\omega = -0.82 \text{ eV}$  are obtained via the numerical solution of the TDSE for different numbers of bound states. (a): Time traces of the ground state in the presence of one (light-blue line), two (violet) and all available (blue line) single particle states. (b) shows the occupation of the second (green line) and third (red line) single particle orbital as a function of time for the complete TDSE. The Fourier transforms of second single particle orbital are plotted in (c) for one (light-blue line) and two (violet line) single particle states and in (d) for three (orange line) and all (blue line) available bound states.

obtained by increasing the number of included excited states up to three for an intensity  $I = 3.52 \cdot 10^{14} \text{ W/cm}^2$  and a detuning  $\hbar\delta\omega = -0.82 \text{ eV}$ . In figure IV.4 (a) the evolution of the ground state occupation is shown for one (light-blue lines), two (violet lines) and all numerically available excited single particle orbitals (blue lines). It is clearly visible that the presence of the second excited single particle orbital significantly improves the agreement with the complete solution of the time-dependent Schrödinger equation. The damping of the Rabi frequency as well as the Rabi period become much closer to the exact solution. In figure IV.4 (b) one can see the occupation probability of the second and third single particle orbital obtained with the complete TDSE. Both signals are strongly affected by a fast frequency component. The Fourier transformation of the time trace confirms that the frequency of the fast oscillations can be identified with  $2\omega_L$ . It corresponds to the enhanced quivering movement induced by the interaction of the electric field with the more loosely bound electron in the first excited single particle orbital. This behaviour is passed further to the occupation of the second excited single particle orbital. Only if an electron is transferred by a Rabi cycle in the first excited orbital the occupation of the second excited orbital performs also the fast oscillations which are necessary to represent the first excited orbital in the field distorted core potential.

A more detailed analysis is provided by the Fourier transforms of the first excited single particle orbitals displayed in figure IV.4 (c) and (d). The results for the reduced atom (light-blue curve in fig. IV.4 (c)) including the lowest excited single particle states show three maxima at  $\Omega_R$ ,  $2\omega_L - \Omega_R$  and  $2\omega_L$ . Taking account of the second excited single particle orbital (violet curve in fig. IV.4 (c)) leads to the appearance of several additional peaks. In particular, one can identify an additional fundamental frequency  $\Omega_R^{1\leftrightarrow 2}$  at

$16.9 \text{ } 2\pi\text{fs}^{-1}$ , which is quite close to the expected Rabi frequency  $\Omega_{2LS}^{1\leftrightarrow 2} = 17.9 \text{ } 2\pi\text{fs}^{-1}$  for an isolated off-resonantly coupled two level system composed of the first and the second excited single particle orbital. This deviation can be identified as the renormalization caused by the ionization of the atom. The appearance of  $\Omega_R^{1\leftrightarrow 2}$  confirms the possibility of a step-ladder Rabi mechanism proposed in [118] for the vibrational levels of electronic states in a  $\text{H}_2$  molecule. In the investigated model atom this mechanism might contain two off-resonantly driven steps, one from the ground state to the first excited state and subsequently to the second excited state. This kind of process is supported by the negative detuning which reduces the absolute detuning  $\delta\omega^{1\leftrightarrow 2}$  for the second step. Indeed the corresponding Rabi frequency  $\Omega_R^{1\leftrightarrow 2}$  is observed in the Fourier-spectrum but the time traces are not significantly affected. The position of the remaining new peaks is given by the differences between  $\Omega_R^{1\leftrightarrow 2}$  and the peaks of the reduced system with one excited single particle orbital. Surprisingly, a contribution at the frequency  $\Omega_R + \Omega_R^{1\leftrightarrow 2}$  is not found. In addition, the existence of the second excited single particle orbital significantly increases the amplitude of the  $2\omega_L$  oscillations and assists the formation of the field-strained first excited state as observed in the time evolution. Figure IV.4 (d) displays results for the reduced atom including three excited single particle states and for the complete solution of the Schrödinger equation. Taking a third excited single particle state into account leads to the appearance of further frequency components in the spectrum. The TDSE reveals an additional rich structure due to the Rydberg like series of the further bound states. However, due to their small amplitudes they do not affect the time traces of the occupation probability. Only the position of  $\Omega_R^{1\leftrightarrow 2}$  compared to the results of one and two excited single particle states is shifted to frequencies of  $16.0 \text{ } 2\pi\text{fs}^{-1}$  (red. atom  $N_{exc} = 3$ ) and  $15.9 \text{ } 2\pi\text{fs}^{-1}$  (TDSE).

### IV.1.1. Renormalization for negative detuning

The previous section revealed the important contribution of the direct two-photon ionization to the ion yield. However, the Rabi frequencies still differ for the different levels of theory. For a further insight in the renormalization of the Rabi frequency and its dependence on the intensity, figure IV.5 displays the quotient between the Rabi frequencies  $\Omega_R$  for models accounting for ionization and  $\Omega_{2LS}$  for an isolated two level system. The latter is extracted from the Fourier transformations of the time evolution of the ground state. Results for three different negative detunings are obtained by the direct solution of the complete TDSE (blue curves), the solution of the Schrödinger equation for a reduced number of single particle states (light-blue and violet curves) and the Markov-approximation (green curves). As already mentioned, the direction of the renormalization is related to the sign of the detuning. In contrast to the resonant case the results in figure IV.5 exhibit for almost all applied intensities and detunings a Rabi frequency larger than in case of an isolated two level system and a non monotonic curve progression. This behaviour can be verified by the analytic expression (IV.1) for the Rabi frequency  $\Omega$ . The term  $\Gamma_0^2$  caused for resonant excitation conditions a renormalization smaller than one. Now additionally the term  $i\delta\omega\Gamma_0$  contributes to the renormalization. The latter scales linearly with the intensity and is affected by the sign of the detuning.

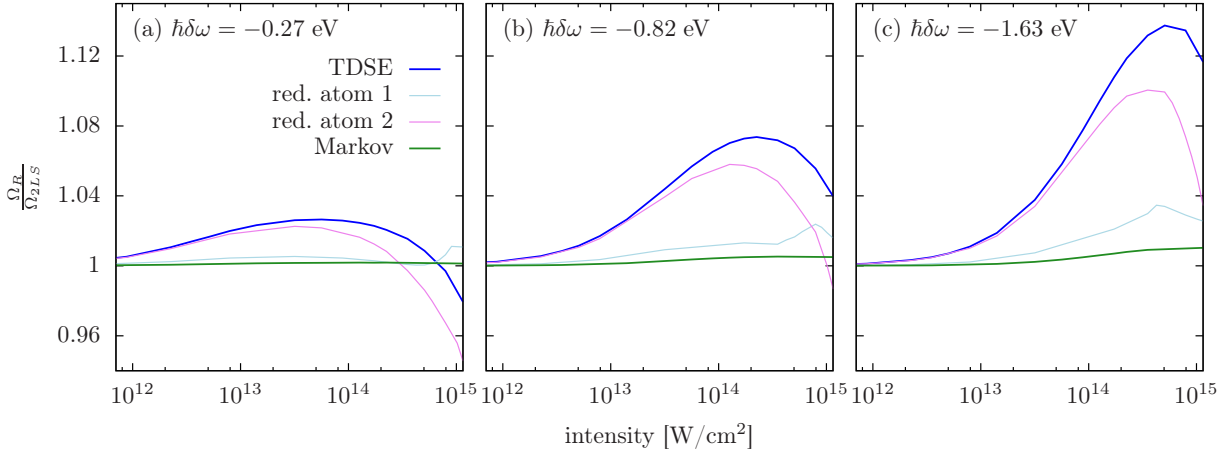


**Figure IV.5.:** Intensity dependence of the Rabi frequency normalized with respect to the expected Rabi frequency for an isolated off-resonantly driven two level system. Results are obtained for the detunings  $\hbar\delta\omega = -0.27$  eV (a),  $\hbar\delta\omega = -0.82$  eV (b) and  $\hbar\delta\omega = -1.63$  eV (c) via the numerical solution for the complete time-dependent Schrödinger equation (blue curve), the time-dependent Schrödinger equation with two (light-blue curve) and three (violet curve) single particle orbitals and for the analytic solution (green curve).

Obviously, it is responsible for the initial rise above one of the renormalization and also explains the larger values of renormalization for an increased detuning. However, the term  $\Gamma_0^2$  gains in importance for high intensities because of its quadratic intensity dependence and induces a decrease of the renormalization. As observed in the case of resonant excitation conditions, for  $\hbar\delta\omega = -0.27$  eV the renormalization finally becomes even smaller than one. Furthermore, the comparison with the results containing one or two excited single particle states manifest an increasing influence of the further neglected bound states on the renormalization. This observation might at first appear inconsistent to the declared relation between the renormalization and the ionization, since similar ionization dynamics were found for the reduced atom and for the exact solution<sup>2</sup>. However, one has to recall the part of the further excited states which do not take part in the Rabi cycle but are involved in the quivering motion induced by the oscillating electric field as observed in figure IV.4 (b). Even though this process does not contribute to the ionization it could be interpreted as further losses from the point of view of the two coupled states and thus affects the renormalization.

### IV.1.2. Influence on the ionization yields

Representing a recent accessible quantity and providing information about contributing processes the final ionization yields are discussed as a function of intensity for finite pulses with a negative detuning. In section III.3 a transition between quadratic and linear intensity scaling was found for a resonant excitation due to the onset of Rabi

<sup>2</sup>As an example in figure IV.3 (d) for  $\hbar\delta\omega = -1.63$  eV at  $I = 1.72 \cdot 10^{14}$  W/cm<sup>2</sup> the ionization dynamics of the complete TDSE and the reduced atom with one excited single particle state show almost no quantitative differences.

oscillations. It is close at hand to verify this feature for an off-resonantly driven atom due to the following additional aspects. For a resonant excitation the quadratic scaling at low intensities of the ionization yields could be almost exclusively attributed to a sequential two-photon ionization in which the atom absorbs one photon to transfer an electron to the first excited state and afterwards a second photon for the transition into the continuum. In contrast, one has to recall that in the off-resonant case the direct two-photon process also contributes to the ion yields and is characterized by a quadratic intensity scaling. These additional ionization paths are enhanced beside the Rabi processes because the Rabi oscillations do not completely deplete the ground state. Therefore, it is not ensured that the presence of Rabi oscillations leads automatically to a linear intensity scaling as in the case of a resonant laser excitation.

In figure IV.6 each plot shows the ionization yields in dependence of the intensity for different pulse durations at a fixed detuning. The envelope of the pulse is a rectangle with smoothed edges during the first and the last five field oscillations. Decrease and rise follow the right and left edge of a Gaussian curve with  $\sigma^2 = 5T_L/3.5$ .  $T_L$  represents the period of one field oscillation. For a negative detuning of  $\hbar\delta\omega = -0.27$  eV, displayed in figure IV.6 (a), the curves for all pulse durations clearly exhibit a crossover between different intensity scalings. Also the position of the transition moves to a lower intensity for increasing pulse duration for  $\hbar\delta\omega = -0.27$  eV and pulse durations of 3 fs (blue line), 6 fs (red line) and 12 fs (green line). Similar to a resonant excitation, this behaviour reflects the onset of Rabi oscillations at a pulse area of  $A = \pi$ . However, in the curve for  $\hbar\delta\omega = -0.27$  eV and a pulse duration 36 fs (orange line) the intensity of the crossover does not shift to smaller intensities as expected. Compared to the ion yields of the 12 fs pulse the transition takes place at roughly the same intensity. A similar behaviour is found for a detuning of  $\hbar\delta\omega = -0.82$  eV (fig. IV.6 (b)). At least for pulse durations of 3 fs, 6 fs and 12 fs one observes an intensity scaling below a quadratic scaling before saturation effects become of importance. Nevertheless a strict linear regime is not established. Only by rising the pulse duration from 3 fs to 6 fs the weak crossover shifts as expected for the onset the Rabi cycles. For  $\hbar\delta\omega = -1.63$  eV (fig. IV.6 (c)) the ion yields do not reveal a transition between different intensity scalings. One can summarize that for an increasing absolute value of the detuning and the pulse duration the crossover loses its sharpness and is not correlated with the pulse area.

This observation reflects the competition between the two ionization pathways contributing to the off-resonantly driven atom, on the one hand the direct two-photon ionization and on the other hand the Rabi-assisted ionization. Which process dominates critically depends on the characteristics of the Rabi cycles in the off-resonant case. These are the dependence of the amplitude of the oscillations on the electric field strength and the contribution of the detuning to the Rabi frequency. In particular, the latter leads to a limiting value of the Rabi frequency for low intensities. This value defines a critical pulse duration at which for all intensities at least one Rabi cycle should be present, even though with a very small amplitude.

$$\lim_{\mathcal{E}_0 \rightarrow 0} \Omega = \delta\omega \quad \Rightarrow \quad t_p^c = \frac{2\pi}{\delta\omega}. \quad (\text{IV.3})$$

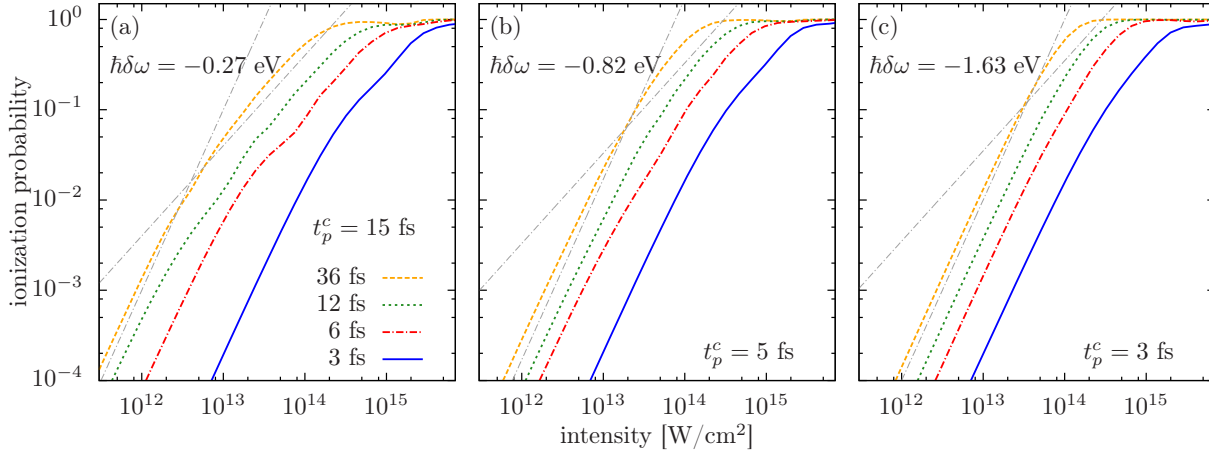


**Figure IV.6.:** Ionization yields after a laser pulse as a function of intensity for the detunings  $\hbar\delta\omega = -0.27$  eV (a),  $\hbar\delta\omega = -0.82$  eV (b) and  $\hbar\delta\omega = -1.63$  eV (c) obtained via the numerical solution of the complete time-dependent Schrödinger equation. The corresponding pulse durations are 36 fs (orange dashed line), 12 fs (green dotted line), 6 fs (red dashed dotted line) and 3 fs (blue solid line). The grey lines mark a strict linear or quadratic intensity scaling and  $t_p^c$  denotes the maximal Rabi period in the case of  $\mathcal{E}_0 = 0$  for each detuning, respectively.

The critical pulse lengths for the applied detunings are given in the corresponding plots of figure IV.6. Obviously, for pulse duration equal or larger than the critical value, the position of the transition between the linear and quadratic intensity scaling is no longer exclusively determined by the pulse duration and the corresponding pulse area. Instead, only the intensity has to be large enough to realise a notable amplitude of the Rabi oscillations resulting in a linear intensity scaling. This behaviour is demonstrated in figure IV.6 (a). Ion yields are plotted for pulse durations which are almost equal (green line, 12 fs) as well as larger (orange line, 36 fs) than the critical value ( $t_p^c = 15$  fs). In agreement with the previous considerations the position of the crossover between the quadratic and the linear intensity scaling is found for both pulse durations approximately at the same intensity. One recognizes a smooth crossover for pulse lengths above the critical value, because the sufficient amplitude of the Rabi oscillations to establish a linear intensity scaling cannot be declared in a precise condition. In contrast, for the results, at which the critical pulse area argument holds, the transition is rather sharp. Therefore the slope of the curve first starts to deviate slightly from the quadratic scaling and bends itself over a large intensity interval until the Rabi oscillations finally dominates and the linear scaling regime occurs.

For  $\hbar\delta\omega = -0.82$  eV and  $\hbar\delta\omega = -1.63$  eV in figures IV.6 (b) and (c) the ion yields deviate from the quadratic intensity scaling, but do not access the regime of a purely linear intensity scaling. A larger detuning results in a smaller critical pulse duration enabling Rabi oscillations for almost all applied pulses. Nevertheless, also a higher field strength is required to excite Rabi cycles which induce deviations from the quadratic intensity scaling. Thus, the direct two-photon ionization dominates until the intensity is sufficient to provide an adequate amplitude of the Rabi oscillations between the ground state and the first excited state. The results manifest that for  $\hbar\delta\omega = -0.82$  eV

and  $\hbar\delta\omega = -1.63$  eV the signal already saturates before the Rabi cycles dominate the ionization. Therefore the ionization scales with an exponent smaller than two without reaching a strict linear intensity dependence. The characteristic intensity, at which deviations from the quadratic intensity scaling for pulse lengths larger than the critical pulse length occur, is related to the amplitude of the Rabi oscillations and depends on the detuning. Figure IV.6 indicates that for an increasing detuning the position of the crossover shifts to higher intensities, as expected.

## IV.2 Positive laser detuning

---

Now the frequency of the laser will be adjusted for an excitation of the ground state above the first excited single particle state without surpassing the third excited single particle state, which is the energetically next state with a non-vanishing dipole coupling. Consequently, for a sufficient high detuning the third excited single particle state takes part in the dynamics and affects the ionization process by the realisation of a additional Rabi process. At first, the validity of the different approximations of the generic model is verified by a comparison with the complete time-dependent Schrödinger equation. Figure IV.7 displays results for two non-interacting electrons obtained with the complete TDSE, the resonant approximation and the analytic solution at a low intensity of  $I = 3.17 \cdot 10^{13}$  W/cm<sup>2</sup>. The time evolution of the ground state is plotted for the detunings  $\hbar\delta\omega = 0.82$  eV (fig IV.7 (a)) and  $\hbar\delta\omega = 1.63$  eV (fig. IV.7 (b)), revealing damped Rabi oscillations with decreasing amplitude for an increasing detuning, as expected. For both detunings the results of the Markov and the resonant approximation coincide with each other during the first 20 fs. In comparison with the results of the resonant approximation, the dynamics of the complete TDSE exhibit oscillations with similar amplitudes but smaller frequencies.

The ionization dynamics received via the Markov and the resonant approximation differ only slightly from each other for the applied detunings in figures IV.7 (c)-(d). For  $\hbar\delta\omega = 0.27$  eV the results of the generic model match quite well those of the complete TDSE (fig. IV.7 (c)). On the contrary, for the enlarged detunings of  $\hbar\delta\omega = 0.82$  eV and  $\hbar\delta\omega = 1.63$  eV differences between the ion yields of TDSE and the resonant approximations occur on long time scales although a qualitatively good agreement for the ground state occupations was found during the first Rabi cycles at  $\hbar\delta\omega = 0.82$  eV (fig. IV.7 (b)). Surprisingly, the Markov approximation as well as the resonant approximation surpass the ion yields of the complete TDSE, even though they include a smaller number of transitions. For a negative detuning the opposed behaviour has been observed because the resonant approximation does not account for the direct two-photon ionization of the ground state. Thus, adding a corresponding rate probably might improve the resonant approximation in case of a negative detuning. Nevertheless, for the current positive detuning a such simple extension probably will not work since it further increases the ion yields of the resonant approximation. In addition, for the largest applied detuning  $\hbar\delta\omega = 1.63$  eV the ionization rate of the TDSE seems to become almost constant. Most

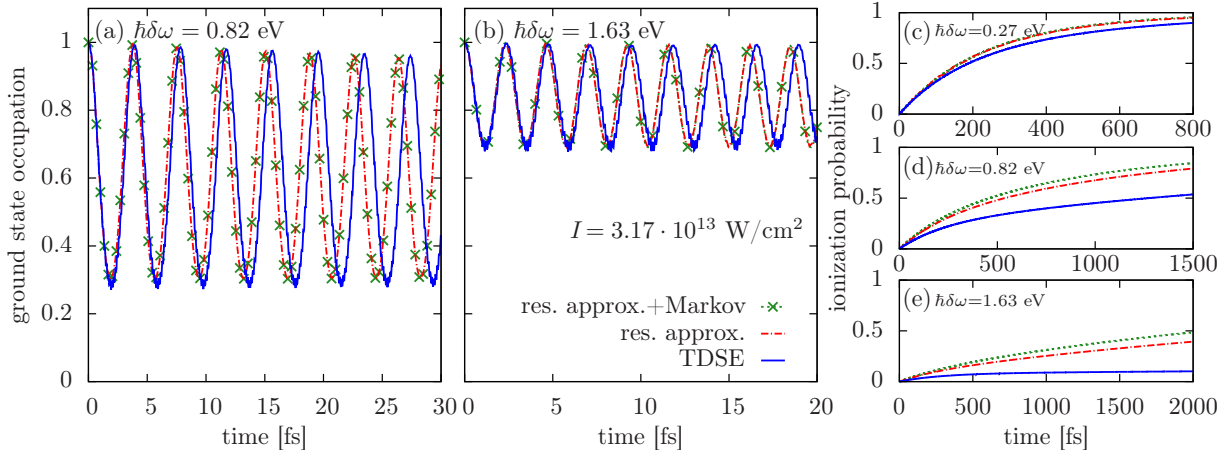


**Figure IV.7.:** Ground state occupation ((a) and (b)) and ion yields ((c) - (e)) as a function of time for two non-interacting electrons at an intensity of  $I = 3.17 \cdot 10^{13} \text{ W/cm}^2$ . The results are obtained via the Markov approximation (green lines and crosses) the resonant approximation (red lines) and the complete TDSE (blue lines). The laser frequency induces the detunings  $\hbar\delta\omega = 0.82 \text{ eV}$  for (a) and (d),  $\hbar\delta\omega = 1.63 \text{ eV}$  for (b) and (e) and  $\hbar\delta\omega = 0.27 \text{ eV}$  for (c).

likely, the reduced ionization for an even higher number of ionization pathways might be caused by the coherent superposition of additional bound states in the complete TDSE.

In order to explore the impact of the third excited single particle state in the dynamics, the detuning as well as the intensity of laser are increased. Thus, the photon energy moves closer to the transition between the ground state and the third excited single particle state. Consequently, the corresponding Rabi cycles oscillate with larger amplitudes. Figure IV.11 displays the ground state occupation ((a)-(d)) and the ion yields ((e) and (f)) obtained via the complete TDSE (blue line) and for the reduced atom including one (green line), two (red line) and three (orange line) excited states. The laser is adjusted to the detunings  $\hbar\delta\omega = 1.63 \text{ eV}$  (fig IV.8 (a), (b), (e)) and  $\hbar\delta\omega = 2.72 \text{ eV}$  (fig IV.8 (c), (d), (f)) at an intensity  $I = 3.52 \cdot 10^{14} \text{ W/cm}^2$ . One has to note that the second excited state does not couple to the ground state due to a vanishing dipole matrix element. The time traces of the ground state are dominated by the Rabi cycles of the first excited state. For  $\hbar\delta\omega = 1.63 \text{ eV}$  the Rabi cycles of the reduced atom including one excited single particle oscillate the fastest. The second excited single particle orbital contributes essentially to the renormalization and results in almost the same Rabi frequency as the complete TDSE. Surprisingly, for  $\hbar\delta\omega = 2.72 \text{ eV}$  in figure IV.8 (c) the amplitude of the Rabi oscillations does not decay monotonically in the results for more than two excited single particle orbitals. Instead, an additional modulation is superimposed onto the amplitudes of the Rabi cycle between the ground state and the first excited state. Although the signature appears with the presence of the third excited state, still quantitative deviations from the results of the complete TDSE are observed. Using a larger time scale (fig. IV.8 (b) and (d)) the modulations of the amplitudes of the Rabi oscillations become also visible at  $\hbar\delta\omega = 1.63 \text{ eV}$ . The different frequencies of the modulations observed for the applied excitation conditions indicate a dependence on the detuning. Due to the relation to

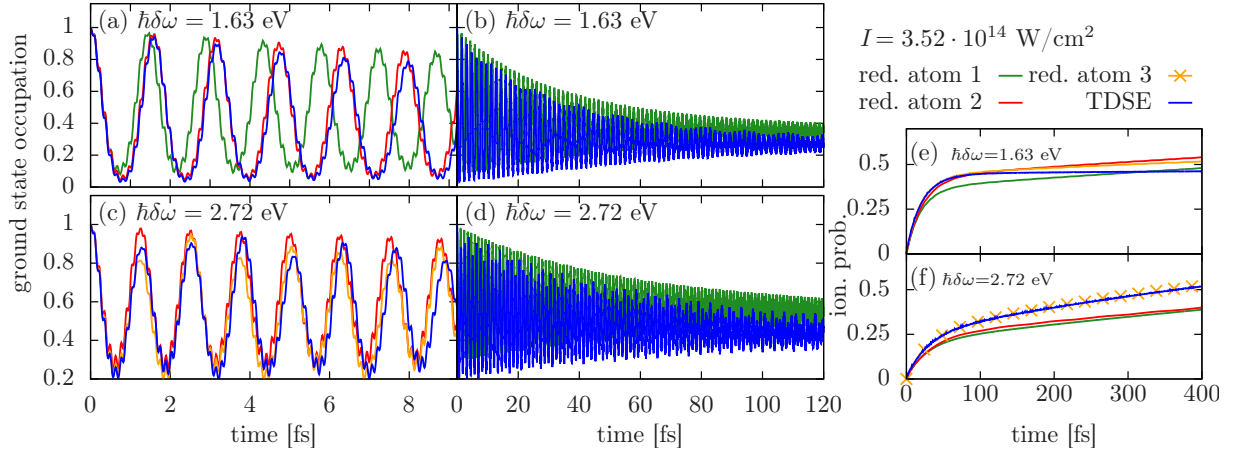


**Figure IV.8.:** The plots (a) - (d) display the time evolution of the ground state occupation as a function of time for the detunings  $\hbar\delta\omega = 1.63$  eV and  $\hbar\delta\omega = 2.72$  eV on a small and large time scale obtained at an intensity  $I = 3.52 \cdot 10^{14}$  W/cm<sup>2</sup> for the TDSE and the reduced level system including two, three and four bound single particle states. The corresponding time dependency of the ion yields is plotted in figures (e) and (f).

the presence of the third excited single particle state, it is close at hand to identify the modulations as beats between the two Rabi cycles of the ground state with the first and third excited state.

Figures IV.8 (e) and (f) display the time evolution of the ion yields for the reduced atom containing one, two and three excited single particle states and the complete TDSE. For  $\hbar\delta\omega = 2.72$  eV (fig. IV.8 (f)) the results including one and two excited single particle states show a qualitative similar ionization as the complete TDSE. A good quantitative agreement is achieved with the extension of the reduced atom to three excited single particle states. Initially the atom is ionized up to 25% in the first 50 fs followed by a strongly reduced ionization rate. The ionization dynamics of the complete TDSE and the reduced atom seem to pass through two regimes. In contrast, the Markov and the resonant approximation (fig. IV.7 (d) and (e)) follow an exponentially increasing ionization with one global ionization rate. In the case of  $\hbar\delta\omega = 1.63$  eV figure IV.8 (e) this signature is even more pronounced. After a steep increase in the first 50 fs, reaching a value of approximately 50%, the ionization becomes almost constant in the case of the complete TDSE. For all numbers of excited states the reduced atom reproduces the initial step rise and the following strongly reduced ionization rate. However, the ionization rate of the second regime does not become as low as for the complete TDSE. This signature denoted as stabilization of the atom or suppression of ionization has been discussed in literature since a long time [47, 85] and has already been observed in a one-dimensional model atom for a two-photon ionization [160]. The applied photon energy in reference [160] realises a similar excitation condition as in the current analysis. Also the reported characteristic peak-splitting of the probability distribution of the wave function in the position space [160] is also found for the present discussed excitation conditions, confirming the observation of the established suppression of ionization.

In order to identify the coexistence of two Rabi processes as the source of the beats

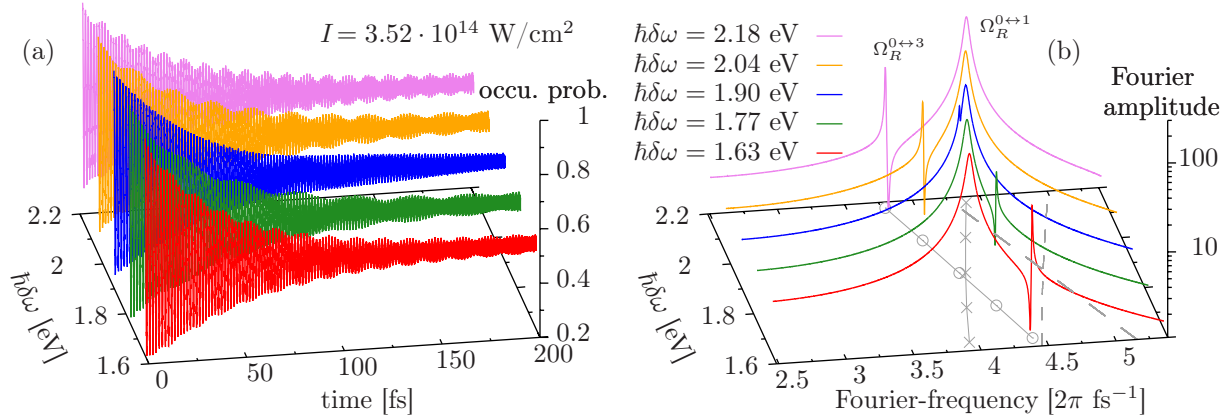


**Figure IV.9.:** Occupation probability of the energetic lowest single particle orbital as a function of time (a) and the corresponding Fourier transformation (b) at an intensity  $I = 3.52 \cdot 10^{14} \text{ W/cm}^2$  for different detunings obtained via the complete TDSE. The position of the broad peaks in graph (b) represents the Rabi frequency  $\Omega_R^{0\leftrightarrow 1}$  of an electron rotating between the two lowest single particle orbitals. The frequency  $\Omega_R^{0\leftrightarrow 3}$  of the Rabi oscillations between the lowest and the third excited single particle orbital corresponds to the narrow peaks. The respective detuning and Fourier frequency of the peaks are marked additionally by grey crosses for  $\Omega_R^{0\leftrightarrow 1}$  and grey circles for  $\Omega_R^{0\leftrightarrow 3}$ . The Rabi frequencies expected for the two isolated two level systems consisting of the particular states of the atom model are illustrated by the two grey dashed lines.

in the ground state dynamics, figures IV.9 (a) and (b) display the time traces of the energetic lowest single particle orbital and the corresponding Fourier transformation. The results are obtained via the complete TDSE at an intensity  $I = 3.52 \cdot 10^{14} \text{ W/cm}^2$  for different detunings. The spectra in figures IV.9 (b) reveal a broad and a narrow peak. The broad peaks correspond to the Rabi frequency  $\Omega_R^{0\leftrightarrow 1}$  of the oscillations between the lowest and first excited single particle orbital. These peaks are moving to higher Fourier-frequencies with increasing detuning. The photon energies of the applied detunings are always smaller than the transition energy from the ground state to the third excited state. Therefore the corresponding detuning  $\delta\omega^{0\leftrightarrow 3}$  is negative. With rising  $\delta\omega$  the absolute value of  $\delta\omega^{0\leftrightarrow 3}$  decreases and consequently the corresponding Rabi frequency is reduced. Indeed, this signature is found for the narrow peak, whose position is denoted as  $\Omega_R^{0\leftrightarrow 3}$ . It is shifted to lower Fourier-frequencies for increasing  $\delta\omega$  and passes the position of  $\Omega_R^{0\leftrightarrow 1}$ . This observation is further illustrated by the grey crosses and circles in fig. IV.9 (b) which project the position of the peak in the plane of  $\delta\omega$  and the Fourier-frequency. For a coexistence of two Rabi processes, the time traces of the ground state occupation might exhibit oscillating contributions of the sum and the difference of the two respective Rabi frequencies. Clearly visible, for  $\hbar\delta\omega = 1.90 \text{ eV}$  the values of both Rabi frequencies almost coincide. In this case, the time evolution of the occupation of the lowest single particle orbital (blue line in fig. IV.9 (a)) performs damped Rabi oscillations without additional modulations. However, modulations in the time traces appear for photon energies inducing two differing Rabi frequencies. The frequency of the modulations is growing with increasing distance between the two Rabi peaks. Obviously, the modulations of the amplitude of the Rabi oscillations stem from the superposition of two coexisting Rabi

processes of the ground state. The frequency component of the modulation represents the difference in frequency between the two superimposed processes and originate from the formation of the absolute squared value of the expansion coefficient of the ground state. Furthermore, also the Rabi frequencies  $\Omega_{2LS}^{0\leftrightarrow 1}$  and  $\Omega_{2LS}^{0\leftrightarrow 3}$  expected for the respective isolated two level systems are displayed in figure IV.9 (b) by the dashed grey lines. As already observed above, the coupling with a positive detuning between the energetic lowest and first excited single particle state induces a slower Rabi frequency  $\Omega_R^{0\leftrightarrow 1}$  for the complete TDSE than for the respective isolated two level system. Surprisingly, the same observation is made for the Rabi frequency  $\Omega_R^{0\leftrightarrow 3}$  between the lowest and the third excited single particle state, even though they are driven with a negative detuning which previously led to a renormalization larger than one (see section IV.1.1). The intersection point between the dashed grey lines marks the detuning which realises the equality of both Rabi frequencies in the case of two independent isolated two level systems. The solid grey lines of the results obtained via the time-dependent Schrödinger equation cross each other at approximately the same value for the detuning. Thus, in the present model the renormalization of the Rabi frequencies neither affects the frequency of the Rabi beats nor the corresponding required photon energy. Nevertheless, for two coexisting Rabi oscillations with opposed renormalization the respective photon energy might be essentially shifted compared to an isolated two level system. In this case, the beats might prove as a signature suited to demonstrate quantitative deviations of the Rabi frequency due to the ionization. Also these Rabi beats represent a possibility to slow down the rather fast Rabi oscillation and would facilitate the access to the latter by experiments.

### IV.2.1. Renormalization for positive detuning

In the following, the renormalization of the Rabi frequency induced by the coupling to the continuum is analysed for the different levels of theory. Therefore the Rabi frequency  $\Omega_R$  for electrons oscillating between the ground state and the first excited state is extracted out of the Fourier spectra and normalized to the Rabi frequency  $\Omega_{2LS}$  given by the corresponding isolated two level system. Figures IV.10 (a) and (b) display the corresponding quotient of  $\Omega_R$  and  $\Omega_{2LS}$  as a function of intensity for two detunings  $\hbar\delta\omega = 0.27$  eV and  $\hbar\delta\omega = 0.82$  eV. The results are obtained via the complete TDSE, the analytic solution and the reduced atom model including up to four excited single particle orbitals. For both detunings the renormalization reveals a similar dependence on the intensity. At low intensities the results for all approaches are close to one and fall below one with increasing intensities, confirming a smaller Rabi frequency in the models than for the isolated two level system. In comparison with the complete TDSE the analytic results obtained via the Markov approximation (green line) substantially underestimate the deviation from the isolated two level system. Also the reduced atom model including the first excited single particle state does not reach the renormalization of the TDSE, but becomes closer with an increasing number of bound states. As in the case of a negative detuning the second excited single particle orbital has a large contribution to the renormalization. However it does not take part in a Rabi process, because its dipole matrix element to the ground state is equal zero and a transition

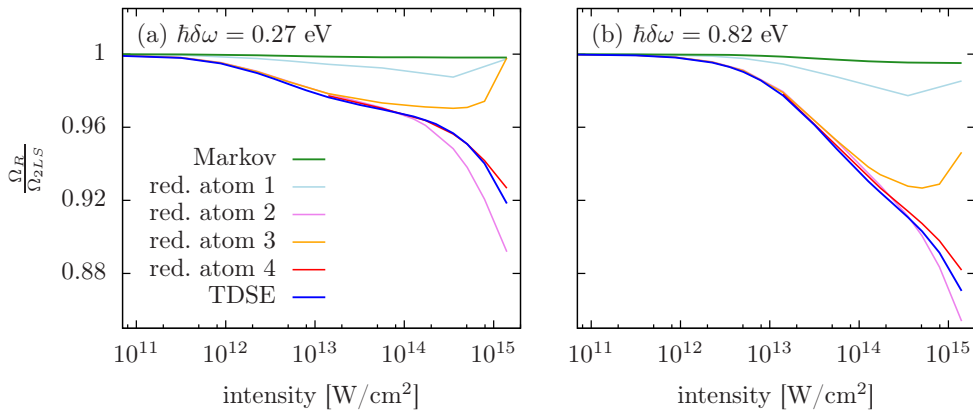


**Figure IV.10.:** Intensity dependence of the Rabi frequency normalized with respect to the expected Rabi frequency for an isolated off-resonantly driven two level system. Results are obtained for the detunings  $\hbar\delta\omega = 0.27$  eV (a) and  $\hbar\delta\omega = 0.82$  eV (b) via the numerical solution for the complete time-dependent Schrödinger equation (blue line), the reduced atom with one (light-blue line), two (violet line), three (orange line), four (red line) excited single particle orbitals and for the analytic results.

with the first excited single particle orbital is driven strongly off-resonant. Instead the second excited single particle orbital is involved in the oscillating motion induced by the electric field when an electron occupies the first single particle state during a Rabi cycle. Interestingly, for a positive detuning the extension to the third excited single particle orbital does not lead to a continuous convergence of the renormalization to the results obtained via the complete TDSE. The received renormalization qualitatively resembles the behaviour obtained with the reduced atom model including only one excited state. The initial decay of the quotient  $\Omega_R/\Omega_{2LS}$  below one is followed by an increase at high intensities. Surprisingly, the observation manifests that a qualitatively correct determination of the renormalization of the Rabi frequency is not achieved by including only the excited state which takes part in the respective Rabi process. Instead also the energetically following state is required to reproduce the results of the complete TDSE. In comparison with the resonantly driven atom model one observes a qualitatively slightly different behaviour of the renormalization. Here, after an initial decrease the slope of the quotient  $\Omega_R/\Omega_{2LS}$  stays almost constant and slightly recovers in the interval  $[10^{12} : 10^{14}]$  W/cm<sup>2</sup> for  $\delta\omega = 0.27$  eV. In contrast, without detuning the renormalization has shown a monotonically decreasing slope.

### IV.2.2. Influence on the ionization yields

In this section the intensity dependence of the ion yields is analysed for different pulse durations and positive detunings. Figure IV.11 displays the ion yields after a laser pulse as a function of intensity for pulse durations of  $t_p = 36$  fs,  $t_p = 12$  fs,  $t_p = 6$  fs and  $t_p = 3$  fs and positive detunings of  $\hbar\delta\omega = 0.27$  eV (a),  $\hbar\delta\omega = 0.82$  eV (b) and  $\hbar\delta\omega = 1.63$  eV (c). The applied pulse form is a rectangle with smoothed edges during the first and the last five field oscillations. Fall and rise follow a Gaussian curve with

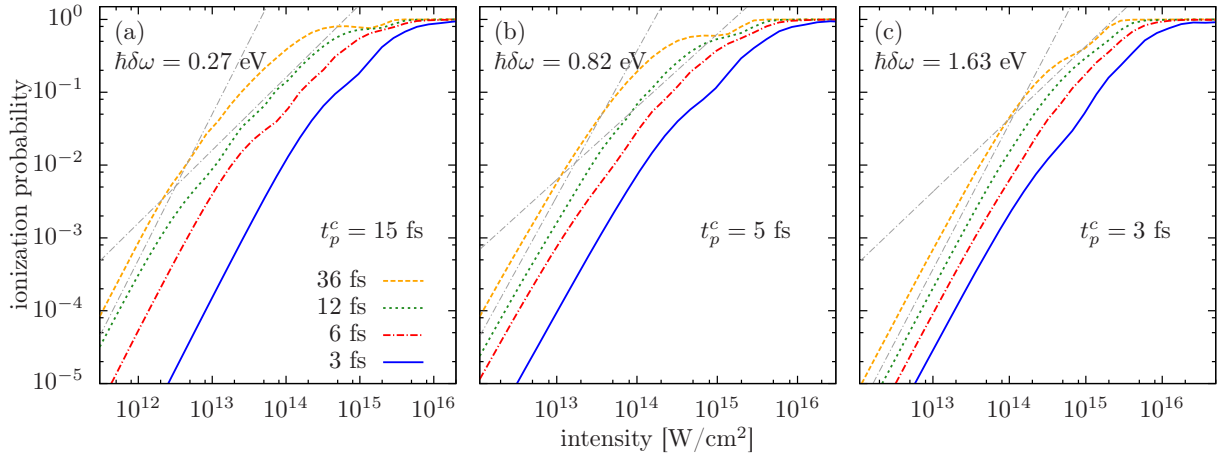


**Figure IV.11.:** Ionization yields after a laser pulse as a function of the intensity for the detunings  $\hbar\delta\omega = 0.27$  eV (a),  $\hbar\delta\omega = 0.82$  eV (b) and  $\hbar\delta\omega = 1.63$  eV (c) obtained via the numerical solution of the complete time-dependent Schrödinger equation. The corresponding pulse durations are 36 fs (orange dashed line), 12 fs (green dotted line), 6 fs (red dashed dotted line) and 3 fs (blue solid line). The grey lines mark a strict linear or quadratic intensity scaling and  $t_p^c$  denotes the maximal Rabi period in the case of  $\mathcal{E}_0 = 0$  for each detuning, respectively.

$\sigma^2 = 5 \cdot T_L/3.5$  where  $T_L$  is the period of one field oscillation. The results reveal a similar behaviour as observed for negative detuning. All curves start with a quadratic intensity scaling at low intensities but in most cases deviate with rising intensity from their initial behaviour before the saturation of the yields is reached. The curves for a pulse duration smaller than the corresponding critical pulse length  $t_p^c = 15$  fs resemble the situation of a resonant excitation. There, the position of the crossovers between different intensity scalings depends on the onset of the Rabi cycles and is determined for each pulse length, respectively. Figure IV.11 (a) for  $\hbar\delta\omega = 0.27$  eV nicely illustrates this behaviour for the pulse lengths of 3 fs, 6 fs and 12 fs. Since the ground state is usually not completely depleted for  $\delta\omega \neq 0$ , the direct two-photon ionization contributes to the ion yields in addition to the Rabi-assisted ionization. Therefore a strict linear intensity scaling is not achieved. For the ion yields induced by a laser pulse longer than the critical pulse length (eq. (IV.3)) the Rabi oscillations are present for all field strengths and are in a competition with the direct two-photon ionization. Here, the initial quadratic intensity scaling of the ion yields is affected at an intensity which is sufficient to provide reasonable Rabi amplitudes to exceed the direct two-photon ionization. Consequently, for pulses longer than the critical pulse length the intensity at which the crossover takes place does not depend on the pulse length. This is clearly visible in figure IV.11 (c) for the applied pulse lengths. In comparison with the results for a negative detuning, the crossover is more pronounced for a positive detuning because the ionization cross-section decreases with increasing photon energy. Thus, the ion yields saturate at higher intensities for a positive detuning and the regime of Rabi-assisted ionization is enlarged.

By rising the photon energy one can replace the excited state which is preferentially involved in the Rabi oscillations. For  $\hbar\delta\omega = 4.90$  eV the transition between the ground state and the first excited state is now driven strongly off-resonant. Instead, the laser

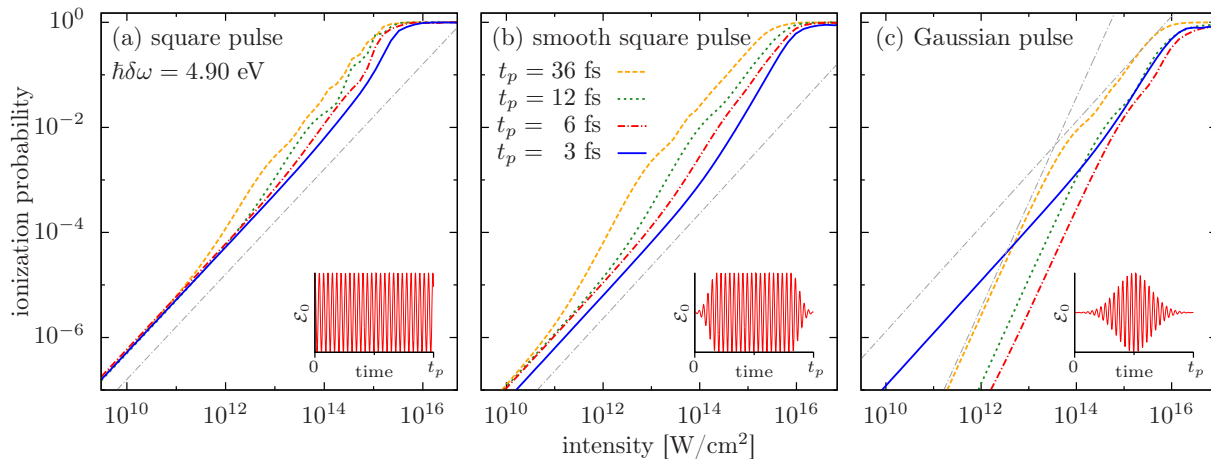


**Figure IV.12.:** Ionization yields after a laser pulse as a function of the intensity for different pulse forms with a detuning of  $\hbar\delta\omega = 4.95$  eV and four pulse durations of 36 fs (orange dashed line), 12 fs (green dotted line), 6 fs (red dashed dotted line) and 3 fs (blue solid line). The applied pulse forms are a squared pulse (a), a smooth squared pulse (b) and a Gaussian pulse (c) sketched in the respective insets. The grey lines mark a strict linear intensity scaling and in (c) additionally a quadratic intensity scaling. The insets sketch the corresponding envelope electric field of the laser.

excites the ground states electrons to the single excited state constructed with the third excited single particle orbital ( $\hbar\delta\omega^{0\leftrightarrow 3} = -0.052$  eV). In addition, also the couplings between the ground state and the other Rydberg-like states as well as the continuum are enhanced. The ion yields generated by a laser pulse with  $\hbar\delta\omega = 4.90$  eV are plotted in figure IV.12 as a function of the intensity. Pulse durations  $t_p$  of 36 fs (orange dashed lines), 12 fs (green dotted lines), 6 fs (red dashed dotted lines) and 3 fs (blue solid lines) have been applied for a squared pulse (a), a smooth square pulse (b) and a Gaussian pulse (c). The different shapes of the pulses strongly affect the ion yields. For a Gaussian shaped pulse with  $t_p \geq 6$  fs the behaviour is similar to resonant excitation conditions. The ion yields start to increase quadratically with intensity indicating a two-photon ionization which is followed by linear intensity scaling due to the onset of the Rabi oscillations.

However, at low intensities the ion yields rise linearly for all applied pulse durations of a sharp or smooth squared pulse. The same behaviour is found for the Gaussian pulse with  $t_p = 3$  fs and contradicts the lowest order perturbation theory. With rising intensity the slope of these curves increases. For pulses longer than 6 fs the linear intensity scaling is regained before saturation is reached and is superimposed with oscillations due to Rabi cycles. Short pulse durations and sharply shaped pulses enhance the regime of the initial linear intensity scaling. Probably, this observation bases on the broadened energy distribution caused by the ultrashort pulses and their sharp temporal envelopes. Therefore the part of photons which have a sufficient high energy to realise a single-photon ionization is increased. In addition, the high detuning is connected with a photon energy closer to the ionization threshold. This fact further supports the contribution of photons with an higher energy than the one corresponding to the central frequency of the laser. Of course, this type of single-photon process is present in most ionization

scenarios which in general are supposed to result in a multi-photon ionization. However, the number of the contributing photons is usually extremely small and thus this process does in general not result in any significant features. Nevertheless, at a sufficient low intensity a process with a linear intensity scaling of the ion yields always wins against the remaining higher order ionization paths. The proposed mechanism inducing the single-photon ionization at low intensities is further confirmed by the results of figure IV.12. It is found that the range of the initial linear scaling is enlarged by shorter and sharper pulses due to their broader frequency distribution. Thus, an excitation commonly expected to perform a two-photon ionization process can cause a deviation from the expected quadratic intensity scaling for ultrashort pulses at low as well as at high photon fluxes. The results further show that the clear appearance of both transitions is not achieved easily since their respective demands on the pulse duration are opposed to each other. Short pulses support the linear intensity scaling at low intensities whereas long pulses increase the regime which is dominated by the Rabi oscillations.



# V

## The role of electron correlations

The investigations in the previous chapters elaborated primarily signatures in the ionization which base on the existence of coherences. In the following, we will focus on the correlations due to the interaction between the electrons and explore their role in the ionization dynamics at high intensities. To this end, the time-dependent Schrödinger equation and the time-dependent Hartree-Fock approach are solved numerically in one dimension for two electrons excited with a coherent femtosecond XUV laser pulse. The content of this chapter has been published by the author and co-workers in reference [74]. For the interaction between the core and the electrons and between the electrons themselves, the short-ranged cosh-potential defined by equation (II.5) is used instead of the softcore potential. The parameters are adjusted to  $U_0 = 6E_{Ryd}$  and  $\alpha = a_B^{-1}$ . This choice yields in a ground state energy ( $E_0 = -81$  eV) and ionization thresholds (single ionization  $I_p^{(1)} = 27$  eV, double ionization  $I_p^{(2)} = 54$  eV) comparable to those of the three dimensional helium atom. The electric field of the laser is represented as

$$\mathcal{E}(t) = \mathcal{E}_0 \cos(\omega t) \exp\left(-\frac{t^2}{2t_p^2}\right). \quad (\text{V.1})$$

The pulse duration is controlled by the parameter  $t_p$  and adjusted in such a way that the full width at half maximum of the field amplitude is 1.6 fs. The center of the pulse is placed at the origin of time.

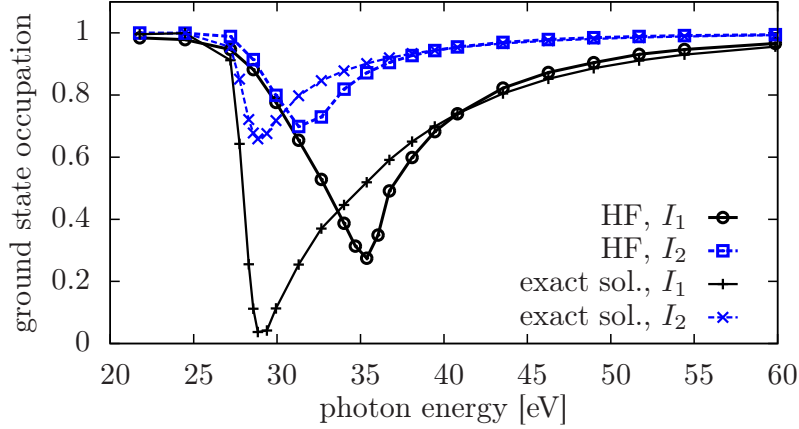


**Figure V.1.:** Occupation probability of the ground state as a function of the photon energy for the two intensities  $I_1 = 3.5 \cdot 10^{14} \frac{\text{W}}{\text{cm}^2}$  and  $I_2 = 5.6 \cdot 10^{13} \frac{\text{W}}{\text{cm}^2}$ .

## V.1 Dynamics of the ground state

An important quantity of interest is the occupation probability of the ground state as it reflects the total ionization yield and has a strong influence on X-ray scattering patterns. It is extracted from the wave function or the reduced density matrix by projecting them on the ground state. In figure V.1 the ground state occupation attained after the interaction with the radiation is displayed as a function of photon energy for two excitation intensities  $I_1 = 3.5 \cdot 10^{14} \frac{\text{W}}{\text{cm}^2}$  and  $I_2 = 1.3 \cdot 10^{14} \frac{\text{W}}{\text{cm}^2}$ . The results obtained with the numerically exact solution (blue and black crosses) are compared with those calculated via time-dependent Hartree-Fock theory<sup>1</sup> (blue squares and black circles). In both cases one receives  $\hbar\omega \approx 27$  eV for the one-photon single ionization threshold which results in a steep decrease of the ground state occupation for higher photon energies. For photon energies below this threshold only multi-photon ionization processes are possible resulting in a weak ionization. A sharp minimum above the threshold is present for all four curves and as expected the total ionization decreases for a reduction of the intensity. In the Hartree-Fock approximation the minimum is less pronounced and shifts to higher photon energies with rising intensity whereas in the exact calculation its position is almost independent on the intensity. Both calculations become more similar the lower the intensity is adjusted. For photon energies above 40 eV the Hartree-Fock curves essentially coincide with the exact results.

In order to understand the reason for the deviations between Hartree-Fock and Schrödinger equation calculations, the time evolution of the ground state occupations are displayed in figure V.2 for the higher intensity  $I_1$  of figure V.1 and for two laser frequencies. First, the results for an excitation at  $\hbar\omega = 38$  eV (figure V.2(a)) shall be discussed which is for both levels of the theory on the right side of the minimum of the

<sup>1</sup>Details concerning the derivation of the time-dependent Hartree-Fock theory are discussed in section VI.

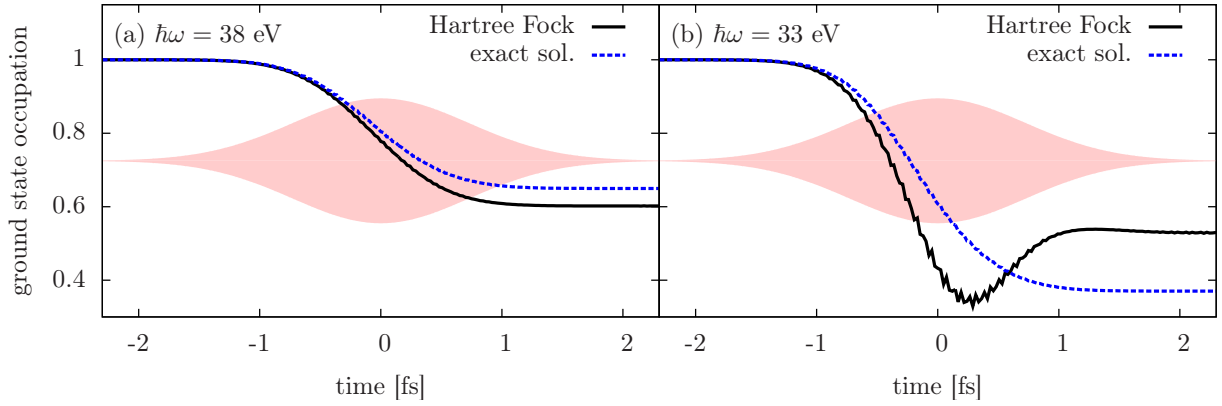


**Figure V.2.:** Time evolution of the ground state occupation  $P_0$  for excitations with an intensity  $I_1 = 3.5 \cdot 10^{14} \frac{\text{W}}{\text{cm}^2}$  and two frequencies: (a)  $\hbar\omega = 38$  eV, (b)  $\hbar\omega = 33$  eV. The red filled area represents the envelope of the electric field  $\mathcal{E}(t)$ .

final ground state occupation. In this case, the Hartree-Fock result agrees qualitatively well with the full calculation. During the laser pulse the occupation probability of the ground state decreases monotonically and finally reaches a value of about  $\sim 60\%$  after the pulse has passed.

In contrast, for an excitation close above the single ionization threshold (fig. V.2(b)) a non monotonic time evolution of the ground state occupation is found in the Hartree-Fock calculation. The atom is ionized until the ground state is populated with  $\sim 34\%$  probability, followed by the reoccupation of the ground state even though the atom is still driven by the laser pulse. In the contrary, the time-dependent Schrödinger equation shows a monotonic evolution of the ionization. A physical explanation of this feature of the Hartree-Fock approach is found by diagonalising the Hartree-Fock Hamiltonian at each time step. It must be noted, that the Hartree-Fock solution is equal to a mean-field treatment and thus the Hartree-Fock Hamiltonian depends parametrically on the time-dependent values of the reduced density matrix. Consequently, the energy eigenvalues obtained by the diagonalisation depend on time. These values effectively determine the ionization threshold [72, 74, 84]. Figure V.3 shows the time evolution of the lowest eigenvalue for an excitation energy of  $\hbar\omega = 33$  eV for the two intensities  $I_1$  and  $I_2$  applied in figure V.1. The lowest eigenvalue decreases with on going ionization because the screening of the core potential by the mean-field of the electrons is reduced which enhances the binding of the remaining electrons. At higher intensity the ionization threshold can therefore exceed the photon energy. Once this is realised single-photon processes are significantly suppressed and the ionization stops even though the pulse is still driving the system. From this time on only transient virtual excitations are generated which finally disappear after the pulse. This is seen as the recovery of the ground state occupation in Figure V.2 (b).

For sufficient high frequencies the ionization is not interrupted since the ionization threshold never becomes larger than the photon energy. This is illustrated in figure V.2 (a) where also the Hartree-Fock curve falls monotonically. The same holds for the lower intensities used in figures V.1 and V.3. This continuous descent of the threshold is not

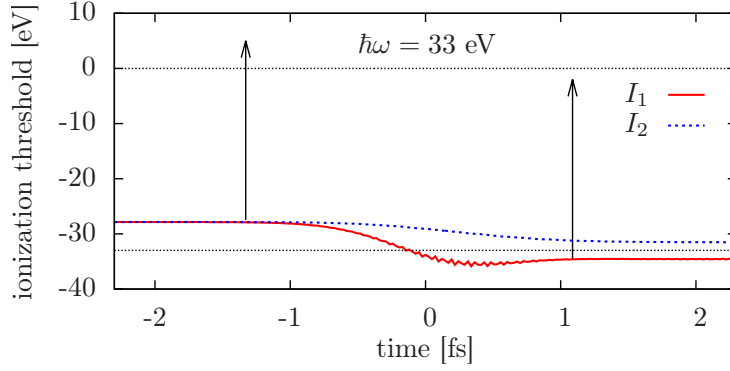


**Figure V.3.:** Time dependence of the lowest Hartree Fock eigenvalues obtained by diagonalising the mean field Hamiltonian at each time step for the two intensities  $I_1 = 3.5 \cdot 10^{14} \frac{\text{W}}{\text{cm}^2}$  and  $I_2 = 5.6 \cdot 10^{13} \frac{\text{W}}{\text{cm}^2}$ . The arrow represents the energy of a single-photon  $\hbar\omega = 33 \text{ eV}$ .

observed in the exact solution, because instead of a mean field charge distribution at the core the two electrons are treated as quantized charges. So either two electrons or one are at the core and a continuous transition between the first and the second ionization threshold does not take place. One expects that the differences between the Hartree-Fock approximation and the exact theory are most pronounced in the two electron system considered here. First, because for larger electron numbers a mean-field can build up more effectively because the contribution of a single electron is less important as in the two electron case. Second, the difference of the single-photon ionization thresholds between the ground state and the ion is largest in the present case.

## V.2 Few photon double-ionization

A phenomenon well-known for being affected by correlation effects is the double ionization of helium. In order to get more insight into the role of different ionization processes, it is worthwhile to analyse the momentum distribution of the emitted electrons, as different processes can be discriminated by corresponding characteristic  $k$ -space patterns. In the real space, parts of the wave function can be identified according to

$$\Psi^{\text{He}}(x_1, x_2) = \begin{cases} \Psi(x_1, x_2) & \text{for } |x_1| < a, |x_2| < a, \\ 0 & \text{else,} \end{cases} \quad (\text{V.2a})$$

$$\Psi^{\text{He}^+}(x_1, x_2) = \begin{cases} \Psi(x_1, x_2) & \text{for } |x_1| < a, |x_2| > a \text{ or } |x_1| > a, |x_2| < a, \\ 0 & \text{else,} \end{cases} \quad (\text{V.2b})$$

$$\Psi^{\text{He}^{2+}}(x_1, x_2) = \begin{cases} \Psi(x_1, x_2) & \text{for } |x_1| > a, |x_2| > a, \\ 0 & \text{else.} \end{cases} \quad (\text{V.2c})$$

An electron is considered as free when it is found at a distance larger than the threshold  $a$  from the core. The threshold is set to  $a = 5a_B$ . By transforming the double ionized part

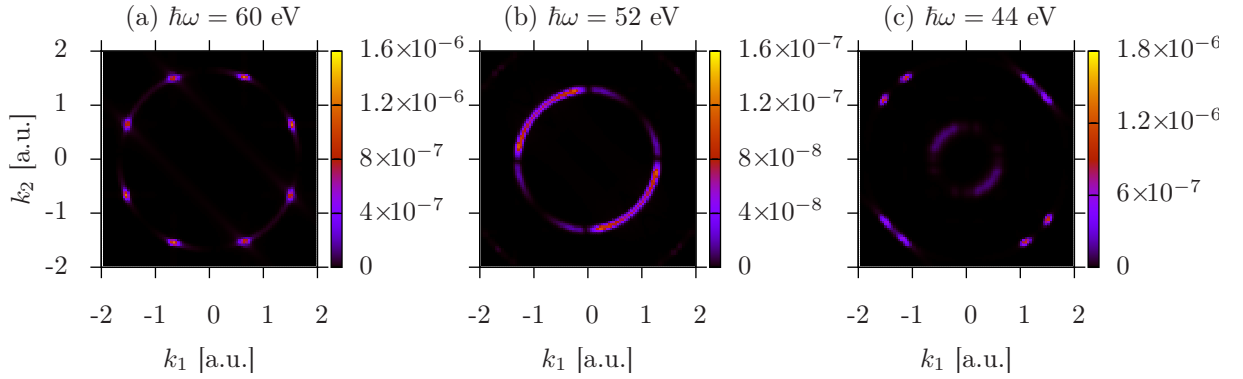


**Figure V.4.:** Absolute square of the two-electron wave function restricted to doubly ionized helium  $|\Psi^{\text{He}^{2+}}(k_1, k_2)|^2$  at a time  $t = 4.9t_p$  after the pulse maximum for an excitation intensity of  $I_1 = 3.5 \cdot 10^{14}$  W/cm<sup>2</sup> and photon energies (a) 60 eV, (b) 52 eV and (c) 44 eV.

$\Psi^{\text{He}^{2+}}(x_1, x_2)$  into the  $k$ -space, the momentum distribution of the two emitted electrons is found.

Of course, the two emitted electrons have to fulfil the energy conservation. For a helium atom which is initially in the ground state with energy  $E_0$  and absorbs  $n$  photons, the kinetic energies  $E_{kin}^1$  and  $E_{kin}^2$  of the two ejected electrons have to satisfy the following relation.

$$E_{kin}^{(1)} + E_{kin}^{(2)} = E_0 + n\hbar\omega, \quad (\text{V.3a})$$

$$\Rightarrow \frac{\hbar^2 k_1^2}{2m} + \frac{\hbar^2 k_2^2}{2m} = E_0 + n\hbar\omega. \quad (\text{V.3b})$$

Therefore, the electrons involved in a double ionization are distributed on circles in the  $k$ -space. This is illustrated in the figure V.4 where the probability  $|\Psi^{\text{He}^{2+}}(k_1, k_2)|^2$  is plotted for the corresponding momenta  $k_1$  and  $k_2$  at a time  $t = 4.9t_p$  after the pulse maximum. The results are in qualitatively good agreement with previous calculations that were performed using a 3D model [45, 69, 119].

With a photon energy of 60 eV (fig. V.4 (a)) it is possible to remove both electrons one after the other by a sequential single-photon ionization. In this case, the  $k_1$  and  $k_2$  values of the ejected electrons are determined by the energy conservation which defines their kinetic energy after they have overcome the first or the second ionization threshold by absorbing one photon. Thus, the momentum distribution for a sequential two-photon double ionization is characterised by sharp peaks on a circle.

The photon energy of 52 eV lies just below the second ionization threshold at  $I_p^{(2)} = 54$  eV and therefore the sequential photoionization is suppressed. In this case the dominating process is the non-sequential two-photon double ionization. The two electrons are released together from the core by absorbing two photons. It is known that this process is characterised by a continuous distribution of the momentum over the circle [54]. In contrast to the sequential double ionization the electrons emitted in the non-sequential process are strongly correlated in terms of the direction in which they are ejected. Due to their mutual Coulomb repulsion they clearly tend to leave the

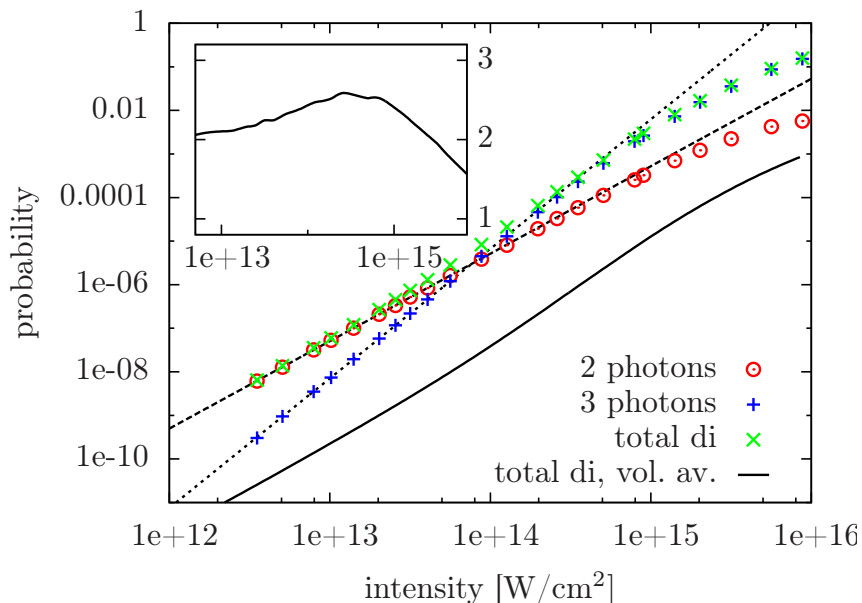


**Figure V.5.:** Contributions to the double ionization yields as a function of the laser intensity for the non-sequential two-photon process (red circles) and the sequential three photon (blue crosses) process as well as the total double ionization with and without volume averaging (green crosses) at  $\hbar\omega = 44$  eV. Fits (dashed and dotted lines) on the power law  $I^n$  in the region  $I < 10^{14}$  W/cm<sup>2</sup> result in  $n = 2$  and  $n = 3$  for the two- and three-photon processes respectively. The inset display the slop of the volume averaged total double ionization.

atom in the opposite directions. Another specific mark is the non-uniform partitioning of the momenta of the electrons implying that one gets almost all of the available energy whereas the other escapes with rather low velocity [67].

On lowering the photon energy further to 44 eV one observes a coexistence between a sequential and a non-sequential process indicated in figure V.4 (c). The inner ring corresponds to a sequential two-photon process and the outer ring reflects a sequential three-photon double ionization. In the latter, first one electron is removed via a single-photon ionization and afterwards two photons lift the remaining electron over the second threshold. Furthermore, a close look at the outer ring reveals that the peaks of electrons emitted in opposite directions are much sharper than those corresponding to an emission in the same direction. This is caused by the stronger influence of the Coulomb interaction on electrons moving side by side with similar velocities compared to the situation where they fly apart.

As know from perturbation theory the probability of the ionization yield usually follows a power law with an exponent given by the number of photons of the respective process. Consequently, the three-photon double ionization only significantly appears at high intensities whereas the two-photon process dominates at low intensities. For a quantitative verification a measure for the strength of the two processes is obtained by integrating the distribution  $|\Psi^{\text{He}^{2+}}(k_1, k_2)|^2$  over the corresponding circles for  $\hbar\omega = 44$  eV. The results are displayed in figure V.5. As expected, at low intensity the double ionization probability in case of the two-photon process rises with the square of the intensity

whereas for the three photon process the dependency is cubic. Both signals saturate above  $\sim 10^{15}$  W/cm<sup>2</sup> although the ionization probability is still below 10%.

In recent experiments with neon the intensity dependence of the total double ionization yield has been analysed [110]. At low intensities a quadratic scaling has been found while at elevated intensities the exponent is between two and three. Qualitatively, this is in accordance with obtained results for intensities below  $\sim 10^{15}$  W/cm<sup>2</sup>. Assuming that the total double ionization probability follows a power law of the form  $I^n$  the slope in a logarithmic plot should give the exponent  $n$ . This slope is plotted in the inset of Fig. V.5. The exponent first increases continuously from 2 to 2.6 until at higher intensities it falls even below 2. Obviously, for intensities above  $\sim 5 \cdot 10^{14}$  W/cm<sup>2</sup> an exponent between two and three does not indicate a competition between two- and three-photon processes of roughly equal strength. Instead, the three-photon process clearly dominates even though the total yield does not show a cubic intensity scaling due to the saturation of the signal.

### V.3 Time dependence of double ionization

---

Advancing the available radiation sources to ever shorter pulse durations makes the temporal evolution of ionization processes to a new focus of interest. First EUV pump EUV probe experiments [139] have analysed the fragmentation dynamics of  $N_2$  and pave the way towards fully time resolved measurements of ultra fast ionization processes. For ultra short excitations one expects theoretically that the quantum dynamics evolves through coherent superposition states during the pulse as well as shortly afterwards. On the contrary the time evolution can also be described by incoherent transition rates. If the rates are not introduced phenomenologically, they are usually calculated by using a golden rule type formula which involves a strict energy conservation between initial and final state. However, in the standard textbook derivations of the golden rule the energy conserving delta-function builds up in time. On short time scales deviations from this behaviour should occur due to the energy-time uncertainty. Indeed, signatures of energy-time uncertainty that result from femto-second laser excitations of semiconductors have recently been theoretically predicted and later measured [8].

In order to quantify such effects for the present system in figure V.6 the momentum distribution  $|\Psi^{\text{He}^{2+}}(k_1, k_2)|^2$  is plotted for different times for a photon energy of 52 eV along the line  $k = k_1 = -k_2$ , i.e. for the emission of two electrons with opposite momenta. From figure V.4 (b) it can be seen that along the line  $k = k_1 = -k_2$  two peaks occur that are symmetric around  $k = 0$ . Figure V.6 is restricted to the peak for positive  $k$  values. The curves have been normalized to their respective maxima in order to facilitate the comparison. As seen from the figure, at early times while the pulse is starting to rise, the width of the  $k$  distribution is more than twice the value found for times when the pulse has vanished. This is the characteristic signature of energy-time uncertainty. At early times the frequency of the pulse and therefore its energy is not yet well defined, resulting in a rather broad momentum distribution of the emitted electrons. At long times the

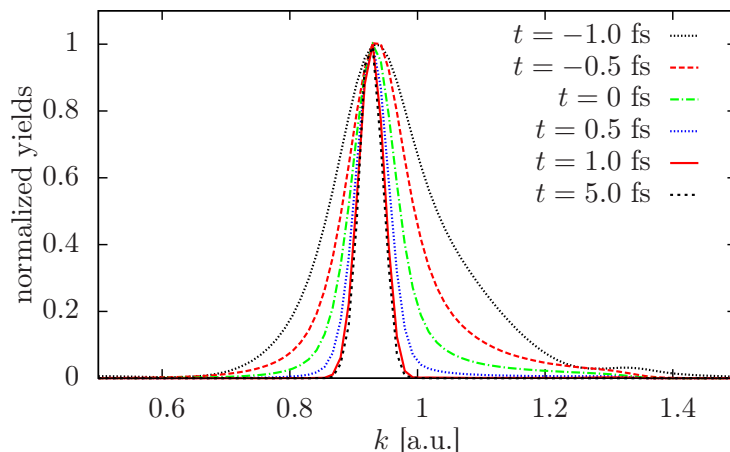


**Figure V.6.:** Momentum distribution of electrons emitted in opposite directions  $|\Psi^{\text{He}^{2+}}(k, -k)|^2$  with equal kinetic energies for different times specified in the figure.

width approaches a finite value which is determined by the finite spectral width of the incoming radiation. Interestingly, the distribution in figure V.6 is strongly asymmetric at early times with more weight at higher  $k$  values. This may be explained recalling that the threshold for single electron ionization affects the double ionization probability because single ionized states appear as virtual intermediate states. This should provide a double resonance structure near  $k = k_1 = -k_2 = 1.3$  atomic units. With strictly energy conserving processes this resonance cannot be reached for our excitation conditions. At short times, however, the energy-time uncertainty allows some excitations close to this threshold. The usual resonant enhancement near the threshold of these excitation tails explains the enhanced distribution at higher  $k$  values in figure V.6.

In order to learn more about the interplay of different ionization processes it is desirable to follow their time evolution separately. To this end one recalls that different double ionization processes result in characteristic traces in the  $k$ -space distribution. For example, two- and three-photon processes can be separated because they result in momenta distributed over rings with different radii (cf. figure. V.4). Further, processes emitting electrons in the same or in the opposite directions can be distinguished by analysing their momentum distribution restricted to either the first and third or to the second and fourth quadrant in the  $k_1 - k_2$  plane. This classification is related to the different double ionization processes. Electrons in a direct process are emitted mainly in opposite directions. Therefore, the distribution in the first and third quadrant can be attributed almost exclusively to sequential and virtual-sequential processes. Sequential processes emit electrons with equal probability in the same as in the opposite direction. Assuming that also virtual-sequential processes give contributions of similar order of magnitude in all quadrants, it follows from figure V.4 (b) that their contribution to the second and fourth quadrant is small compared to the total number of electrons recorded in this part of the momentum distribution. Thus, the distribution in these quadrants mainly reflects direct processes. By integrating over the respective areas in the  $k_1 - k_2$  plane one obtains a measure for the corresponding processes.

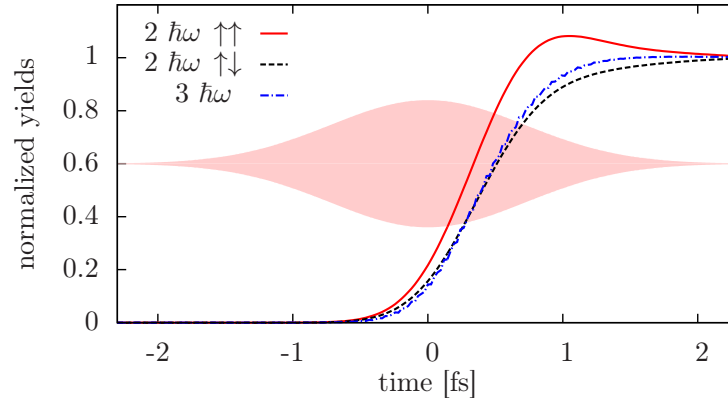


**Figure V.7.:** The graph displays the time evolution of different contributions to the double ionization: The two-photon process with electron emitted in the same ( $2\hbar\omega \uparrow\uparrow$ ) or in the opposite ( $2\hbar\omega \uparrow\downarrow$ ) direction and the three-photon process ( $3\hbar\omega$ ). The laser intensity is  $I_1 = 3.5 \cdot 10^{14} \frac{\text{W}}{\text{cm}^2}$  at a photon energy of  $\hbar\omega = 52$  eV. The signals are normalized to their long time values. The red filled area represents the envelope of the electric field  $\mathcal{E}(t)$ .

These integrated quantities are shown in figure V.7 as a function of time for an excitation intensity of  $3.5 \cdot 10^{14} \frac{\text{W}}{\text{cm}^2}$  and a photon energy  $\hbar\omega = 52$  eV. To improve the comparability all curves are normalized to their values at long time values. The ionization of all contributions in Fig. V.7 essentially sets in after the pulse has reached its maximum. This delay reflects the time electrons have to travel until they are separated enough from the core to be counted as emitted (cf. Eq. (V.2c)). The amplitudes of two-photon emission in the same direction and three-photon double ionization rise monotonically on essentially the same time scale. In contrast, emissions of two electrons in the same direction start slightly earlier and exhibit a non-monotonic time dependence. A possible explanation for this non-monotonic behaviour is the repelling interaction between the electrons emitted in the same direction. Therefore a certain probability exists that one of the electrons returns to the core area after it has left this region. In a previous study for excitations far below the second ionization threshold, the almost complete suppression of two-electron emission in the same direction, which is typically found at long times for these excitation conditions, has been attributed to this recapture process [45]. Our results in Fig. V.7 indicate that recapture processes are still noticeable but much weaker in the virtual-sequential regime studied here.



# VI

## Application of the reduced density matrix on photoionization

This chapter is concerned with the application of the time-dependent reduced density matrix (TDRDM) formalism on the electrons of an atom exposed to intensive XUV radiation. At first, the derivation of the equations of motion is outlined for the representation of the RDMs by the finite-element discrete variable representation. In order to account for the correlations between electrons in the ionization the hierarchy of equations is truncated one level above the Hartree-Fock theory, limiting the set of dynamical variables to the reduced one and two particle density matrices. The latter is further separated in correlated and uncorrelated contributions to allow the controlled truncation of the hierarchy of equations. Furthermore, the separation between the spin and basis function variables of the density matrix by a product ansatz will be discussed as well as the need for reliable initial conditions. To avoid the known numerical disadvantages of implicit finite difference methods a suitable time-propagation scheme is presented that benefits from the sparse representation of operators in the finite-element discrete variable representation. Finally, results of the ionization dynamics for atoms with two, four and six electrons are discussed. To the best of the knowledge of the author only Schäfer-Bung and Nest [147] have reported so far about the application of the TDRDM

formalism above the mean field level for the interaction between a laser pulse and a one-dimensional atom. Thus, differences in their realisation compared to following approach will be addressed in the respective sections.

## VI.1 Equations of motion

The first step in the derivation of the equations of motion in the reduced density matrix formalism is the determination of the time derivative of the annihilation and creation operators via the Heisenberg equation. For a shortened notation the Hamilton operator (equ. (II.4)) of the system is split in the electron-electron interaction  $V_{a,b}^{\text{el}}$ , the interaction with the laser field  $H_a^{\text{field}}$  and in a contribution  $H_{a,b}^0$  which combines the time-independent single particle operators for the kinetic energy and the potential of the core.

$$H_{a,b}^0 = T_{a,b}^{\text{kin}} + V_{a,b}^{\text{core}}. \quad (\text{VI.1})$$

Making use of the decompositions given in equations (II.23) and (II.24) results in a closed set of equations for the reduced one particle density matrix and the four-point correlations [7].

$$\begin{aligned} i\hbar \frac{\partial}{\partial t} \rho_{a,b} &= \sum_{b'} H_{b,b'}^0 \rho_{a,b'} - \sum_{a'} H_{a',a}^0 \rho_{a',b} + \left( H_b^{\text{field}} - H_a^{\text{field}} \right) \rho_{a,b} \\ &+ \left( \sum_c \left( V_{b,c}^{\text{el}} - V_{a,c}^{\text{el}} \right) \rho_{c,c} \right) \rho_{a,b} + \sum_c \left( V_{b,c}^{\text{el}} - V_{a,c}^{\text{el}} \right) \left( -\rho_{a,c} \rho_{c,b} + C_{a,c,c,b} \right), \\ i\hbar \frac{\partial}{\partial t} C_{a,b,c,d} &= \frac{1}{2} A \left[ \sum_{d'} H_{d,d'}^0 C_{a,b,c,d'} - \sum_{a'} H_{a',a}^0 C_{a',b,c,d} + \left( V_{c,d}^{\text{el}} - V_{a,b}^{\text{el}} \right) \rho_{a,d} \rho_{b,c} \right] \\ &+ \left( H_c^{\text{field}} + H_d^{\text{field}} - H_a^{\text{field}} - H_b^{\text{field}} \right) C_{a,b,c,d} + \left( V_{c,d}^{\text{el}} - V_{a,b}^{\text{el}} \right) C_{a,b,c,d} \\ &+ \sum_j \left( V_{c,j}^{\text{el}} + V_{d,j}^{\text{el}} - V_{a,j}^{\text{el}} - V_{b,j}^{\text{el}} \right) \rho_{j,j} C_{a,b,c,d} \\ &+ A \left[ \sum_j \left( V_{c,j}^{\text{el}} + V_{d,j}^{\text{el}} - V_{a,j}^{\text{el}} - V_{b,j}^{\text{el}} \right) \left( \rho_{a,j} C_{b,j,c,d} + \rho_{j,d} C_{a,b,j,c} \right) \right] \\ &+ A \left[ \rho_{b,c} \sum_j \left( V_{c,j}^{\text{el}} - V_{b,j}^{\text{el}} \right) \left( C_{a,j,j,d} - \rho_{a,j} \rho_{j,d} \right) \right]. \end{aligned} \quad (\text{VI.3})$$

The operator  $A$  defined by  $A[f_{a,b,c,d}] = f_{a,b,c,d} - f_{b,a,c,d} - f_{a,b,d,c} + f_{b,a,d,c}$  anti-symmetrizes a function  $f_{a,b,c,d}$ . Without the four-point correlations equation (VI.2) completely represents the time-dependent Hartree-Fock approach for the reduced one particle density matrix. Equation (VI.3) defines the evolution of the four-point correlations. The six-point correlation function  $C_{a,b,c,d,e,f}$ , which appears in the decomposition (II.24), is neglected. This kind of truncation of the hierarchy of the equations has been proposed by reference

[173]. In contrast to the Bogolyubov-Born-Green-Kirkwood-Yvon hierarchy the truncation induces non-linear equations. Although the reference [173] proved the compatibility of the truncation with the conservation laws for one and two particle operators, the trace relation

$$\rho_{1,1',2,2',\dots,j,j'} = \frac{1}{(N-j)!} \text{Tr}_{(j+1,\dots,N)} \{ \rho_{1,1',2,2',\dots,N,N'} \}, \quad (\text{VI.4})$$

for the reduced density matrices is violated. The reduction of the RDM formalism to the subdynamics of the  $j$ -particle RDMs and correlations is commonly denoted as SUB( $j$ ). Thus, the above implementation represents the SUB(2) level of the RDM formalism and has also been applied by Schäfer-Bung and Nest [147] in a similar manner. Instead of the four-point correlation function Schäfer-Bung and Nest determined the reduced two particle density matrix. Even though they formally used the same reconstruction of the three particle RDM, in this case uncorrelated contributions enter the one and the two particle RDM. The separation in correlated and uncorrelated parts of the RDMs avoids this redundant implication in the equation of motion of the four-point function. Besides, Schäfer-Bung and Nest represented the two particle RDM by products of two-electron determinants, using 20 spin orbitals obtained via stationary Hartree-Fock calculations.

### VI.1.1. Separation of spin and basis function variables

The derived equations of motion still combine the spin and FEDVR variable. In order to reduce the number of variables of the reduced density matrix and the four-point correlations, a product ansatz for the separation of the spin and the function basis set is proposed, which restricts the degree of freedom. The approach shall account for a non-polarized spin state, which is not affected by coherences concerning the spin. Bearing in mind that the applied Hamiltonian does not act on the spin, these conditions are conserved by the equations of motion if they are fulfilled by the initial state. For the reduced one particle density the following separation is proposed.

$$\rho_{\mathbf{a},\mathbf{b}} = \delta_{\sigma_a,\sigma_b} \rho_{n_a,n_b}. \quad (\text{VI.5})$$

In order to motivate the ansatz for the correlation  $C_{\mathbf{a},\mathbf{b},\mathbf{c},\mathbf{d}}$  the consequence of equation (VI.5) on the uncorrelated contribution of the four-point function  $\rho_{\mathbf{a},\mathbf{b},\mathbf{c},\mathbf{d}}$  is determined via the antisymmetrized product of  $\rho_{\mathbf{a},\mathbf{b}}$

$$\begin{aligned} \rho_{\mathbf{a},\mathbf{d}}\rho_{\mathbf{b},\mathbf{c}} - \rho_{\mathbf{a},\mathbf{c}}\rho_{\mathbf{b},\mathbf{d}} &= \delta_{\sigma_a,\sigma_d} \rho_{n_a,n_d} \delta_{\sigma_b,\sigma_c} \rho_{n_b,n_c} - \delta_{\sigma_a,\sigma_c} \rho_{n_a,n_c} \delta_{\sigma_b,\sigma_d} \rho_{n_b,n_d} \\ &= \frac{1}{2} (\delta_{\sigma_a,\sigma_d} \delta_{\sigma_b,\sigma_c} - \delta_{\sigma_a,\sigma_c} \delta_{\sigma_b,\sigma_d}) (\rho_{n_a,n_d} \rho_{n_b,n_c} + \rho_{n_a,n_c} \rho_{n_b,n_d}) \\ &\quad + \frac{1}{2} (\delta_{\sigma_a,\sigma_d} \delta_{\sigma_b,\sigma_c} + \delta_{\sigma_a,\sigma_c} \delta_{\sigma_b,\sigma_d}) (\rho_{n_a,n_d} \rho_{n_b,n_c} - \rho_{n_a,n_c} \rho_{n_b,n_d}). \end{aligned} \quad (\text{VI.6})$$

Obviously the uncorrelated contributions of the four-point function  $\rho_{\mathbf{a},\mathbf{b},\mathbf{c},\mathbf{d}}$  split into two parts. One consists of an antisymmetric spin and a symmetric orbit function and the other is built up by a symmetric spin and an antisymmetric orbit function. As identifiable

in equation (VI.6), the symmetry and the antisymmetry concerns a permutation within the pairs  $(\sigma_a, \sigma_b)$ ,  $(\sigma_c, \sigma_d)$ ,  $(n_a, n_b)$  and  $(n_c, n_d)$ . The same separation is adopted for the four-point correlation function.

$$\begin{aligned} C_{\mathbf{a},\mathbf{b},\mathbf{c},\mathbf{d}} = & (\delta_{\sigma_a,\sigma_d} \delta_{\sigma_b,\sigma_c} - \delta_{\sigma_a,\sigma_c} \delta_{\sigma_b,\sigma_d}) C_{n_a,n_b,n_c,n_d}^S \\ & + (\delta_{\sigma_a,\sigma_d} \delta_{\sigma_b,\sigma_c} + \delta_{\sigma_a,\sigma_c} \delta_{\sigma_b,\sigma_d}) C_{n_a,n_b,n_c,n_d}^A. \end{aligned} \quad (\text{VI.7})$$

$C_{n_a,n_b,n_c,n_d}^S$  and  $C_{n_a,n_b,n_c,n_d}^A$  are the symmetric and antisymmetric parts of the four-point correlations. Even though for a single Slater determinant, as it is the case in the Hartree-Fock theory, the product ansatz for spin and basis function variables is exact, a wave function including correlations invokes further contributions which are not caught by the applied ansatz. A physical interpretation is given by the following identities relating the spin terms with the singlet and triplet states  $\chi^S(\sigma_1, \sigma_2)$  and  $\chi_{m_S}^T(\sigma_1, \sigma_2)$ .

$$(\delta_{\sigma_a,\sigma_d} \delta_{\sigma_b,\sigma_c} - \delta_{\sigma_a,\sigma_c} \delta_{\sigma_b,\sigma_d}) = 2\chi^S(\sigma_a, \sigma_b)\chi^S(\sigma_c, \sigma_d) \quad (\text{VI.8})$$

$$\begin{aligned} (\delta_{\sigma_a,\sigma_d} \delta_{\sigma_b,\sigma_c} + \delta_{\sigma_a,\sigma_c} \delta_{\sigma_b,\sigma_d}) = & 2 [\chi_0^T(\sigma_a, \sigma_b)\chi_0^T(\sigma_c, \sigma_d) + \chi_1^T(\sigma_a, \sigma_b)\chi_1^T(\sigma_c, \sigma_d) + \\ & \chi_{-1}^T(\sigma_a, \sigma_b)\chi_{-1}^T(\sigma_c, \sigma_d)] \end{aligned} \quad (\text{VI.9})$$

Thus,  $C_{n_a,n_b,n_c,n_d}^S$  corresponds to the correlations carried by two electrons in the spin singlet state and  $C_{n_a,n_b,n_c,n_d}^A$  represents the correlations between two electrons in the spin triplet states. In the implementation of Schäfer-Bung and Nest [147] no explicit separation between spin and orbital variables is carried out, because they represented the reduced two particle density matrix by two-electron determinants. The reduced two particle density matrix constructed by products of two-electron determinants contains also spin configuration formed by products between singlet and triplet spin states. Thus, the approach of Schäfer-Bung and Nest implies contributions which are neglected by equation (VI.7). Inserting equations (VI.5) and (VI.7) into the equations of motion leads to a closed set of equation of  $\rho_{n_a,n_b}$ ,  $C_{n_a,n_b,n_c,n_d}^A$  and  $C_{n_a,n_b,n_c,n_d}^S$ .

$$\begin{aligned} i\hbar \frac{\partial}{\partial t} \rho_{n_a,n_b} = & \sum_{n_j} H_{n_b,n_j}^0 \rho_{n_a,n_j} - \sum_{n_j} H_{n_j,n_a}^0 \rho_{n_j,n_b} + (H_{n_b}^{\text{field}} - H_{n_a}^{\text{field}}) \rho_{n_a,n_b} \\ & + 2(\phi_{n_b} - \phi_{n_a}) \rho_{n_a,n_b} - \sum_{n_j} (V_{n_b,n_j}^{\text{el}} - V_{n_a,n_j}^{\text{el}}) \rho_{n_a,n_j} \rho_{n_j,n_b} \\ & + \sum_{n_j} (V_{n_b,n_j}^{\text{el}} - V_{n_a,n_j}^{\text{el}}) (C_{n_a,n_j,n_j,n_b}^S + 3C_{n_a,n_j,n_j,n_b}^A), \end{aligned} \quad (\text{VI.10a})$$

$$\begin{aligned}
i\hbar \frac{\partial}{\partial t} C_{n_a, n_b, n_c, n_d}^{S/A} &= \frac{1}{2} S/A \left[ \sum_{n_j} \left( H_{n_d, n_j}^0 C_{n_a, n_b, n_c, n_j}^{S/A} - H_{n_j, n_a}^0 C_{n_j, n_b, n_c, n_d}^{S/A} \right) \right] \\
&+ \left( H_{n_c}^{\text{field}} + H_{n_d}^{\text{field}} - H_{n_a}^{\text{field}} - H_{n_b}^{\text{field}} \right) C_{n_a, n_b, n_c, n_d}^{S/A} \\
&+ \left[ V_{n_c, n_d}^{\text{el}} - V_{n_a, n_b}^{\text{el}} + 2(\phi_{n_c} + \phi_{n_d} - \phi_{n_a} - \phi_{n_b}) \right] C_{n_a, n_b, n_c, n_d}^{S/A} \\
&- \sum_{n_j} \left( V_{n_c, n_j}^{\text{el}} + V_{n_d, n_j}^{\text{el}} - V_{n_a, n_j}^{\text{el}} - V_{n_b, n_j}^{\text{el}} \right) \left( \rho_{n_a, n_j} C_{n_b, n_j, n_c, n_d}^{S/A} \pm \rho_{n_b, n_j} C_{n_a, n_j, n_c, n_d}^{S/A} \right. \\
&\left. \pm \rho_{n_j, n_d} C_{n_a, n_b, n_j, n_c}^{S/A} + \rho_{n_j, n_c} C_{n_a, n_b, n_j, n_d}^{S/A} \right) + \frac{1}{2} \left( V_{n_d, n_c}^{\text{el.-el.}} - V_{n_a, n_b}^{\text{el}} \right) \left( \rho_{n_b, n_c} \rho_{n_a, n_d} \pm \rho_{n_a, n_c} \rho_{n_b, n_d} \right) \\
&+ \frac{1}{2} S/A \left[ \rho_{n_b, n_c} \sum_{n_j} \left( V_{n_c, n_d}^{\text{el}} - V_{n_b, n_j}^{\text{el}} \right) \left( C_{n_a, n_j, n_j, n_d}^S + 3C_{n_a, n_j, n_j, n_d}^A - \rho_{n_a, n_j} \rho_{n_j, n_d} \right) \right].
\end{aligned} \tag{VI.10b}$$

The mean field potential of the electron distribution is denoted as  $\phi_n = \sum_{n'} V_{n, n'}^{\text{el}} \rho_{n', n'}$ . Analogously to the operator  $A$  a function is symmetrized by the operator  $S$  via  $S[f_{a,b,c,d}] = f_{a,b,c,d} + f_{b,a,c,d} + f_{a,b,d,c} + f_{b,a,d,c}$ . The equations of motion imply that  $C_{n_a, n_b, n_c, n_d}^A$  and  $C_{n_a, n_b, n_c, n_d}^S$  are coupled among each other, indirectly, since both effect  $\rho_{n_a, n_b}$  and in a direct manner due to the last line of the equation (VI.10b).

### VI.1.2. Choice of the initial values

Starting the propagation of the equation of motion require the choice of initial values for  $\rho_{n_a, n_b}$ ,  $C_{n_a, n_b, n_c, n_d}^A$  and  $C_{n_a, n_b, n_c, n_d}^S$ , which define the state of the atom before it interacts with the radiation of the laser. Usually, the thermal energy of the target atoms in an XUV ionization experiment is small compared with the energetic gaps of the atomic states if the fine structure is neglected. Thus, using the ground state of the atom as starting point for the time evolution of the ionization dynamics represents a well justified and commonly applied approach. Nevertheless, one has to ensure that the initial values for the dynamic variables act as a stationary state in the equations of motion. Due to the truncation of the hierarchy of the equations of motion this property for equation (VI.10) is not even guaranteed for the reduced density matrix and the correlations extracted from the exact correlated ground state. To this end the dynamic variables are divided into two parts.

$$\rho_{n_a, n_b}(t) = \rho_{n_a, n_b}^0 + \delta\rho_{n_a, n_b}(t), \tag{VI.11a}$$

$$C_{n_a, n_b, n_c, n_d}^{S/A}(t) = C_{n_a, n_b, n_c, n_d}^{0, S/A} + \delta C_{n_a, n_b, n_c, n_d}^{S/A}(t). \tag{VI.11b}$$

$\rho_{n_a, n_b}^0$  and  $C_{n_a, n_b, n_c, n_d}^{0, S/A}$  define the initial values with respect to the ground state and  $\delta\rho_{n_a, n_b}(t)$  and  $\delta C_{n_a, n_b, n_c, n_d}^{S/A}(t)$  account for the dynamics induced by the laser field and are equal zero at time  $t = 0$ . Furthermore, one assumes that the initial values represent stationary solutions of the equations of motion. Inserted in the equations of motion without a laser field these values shall conform to  $\partial_t \rho_{n_a, n_b}^0 = 0$  and  $\partial_t C_{n_a, n_b, n_c, n_d}^{0, S/A} = 0$ . In this manner

equations are received for the field induced contributions  $\delta\rho_{n_a,n_b}(t)$  and  $\delta C_{n_a,n_b,n_c,n_d}^{S/A}(t)$  to avoid dynamics of the initial values. In the present thesis the initial ground state shall be restricted to the Hartree-Fock ground state, which neglects correlation between the electrons at the beginning, leading to  $C_{n_a,n_b,n_c,n_d}^{0,S/A} = 0$ . Adopting this approach on the Hartree-Fock level of the reduced density matrix formalism yields in:

$$\begin{aligned}
i\hbar \frac{\partial}{\partial t} \delta\rho_{n_a,n_b} &= \sum_{n_j} H_{n_b,n_j}^0 \delta\rho_{n_a,n_j} - \sum_{n_j} H_{n_j,n_a}^0 \delta\rho_{n_j,n_b} + \left( H_{n_a}^{\text{field}} - H_{n_b}^{\text{field}} \right) \rho_{n_a,n_b} \\
&+ 2 \sum_{n_j} \left( V_{n_b,n_j}^{\text{el}} - V_{n_a,n_j}^{\text{el}} \right) \left( \rho_{n_j,n_j}^0 \delta\rho_{n_a,n_b} + \delta\rho_{n_j,n_j} \rho_{n_a,n_b}^0 + \delta\rho_{n_j,n_j} \delta\rho_{n_a,n_b} \right) \\
&- \sum_{n_j} \left( V_{n_b,n_j}^{\text{el}} - V_{n_a,n_j}^{\text{el}} \right) \left( \rho_{n_a,n_j}^0 \delta\rho_{n_j,n_b} + \delta\rho_{n_a,n_j} \rho_{n_j,n_b}^0 + \delta\rho_{n_a,n_j} \delta\rho_{n_j,n_b} \right) \\
&- \sum_{n_j} \left( V_{n_b,n_j}^{\text{el-el}} - V_{n_a,n_j}^{\text{el}} \right) \left( \delta C_{n_a,n_j,n_j,n_d}^S + 3\delta C_{n_a,n_j,n_j,n_d}^A \right) \tag{VI.12}
\end{aligned}$$

One can easily see that without the presence of an electric field and for  $\delta\rho_{n_a,n_b}$  and  $C_{n_a,n_b,n_c,n_d}^{0,S/A}$  equal zero, the right hand side of equation (VI.12) does not induce any dynamics. The same proceeding is also applied for the equations of motions of the two particle correlations. In contrast, Schäfer-Bung and Nest used correlated initial values for the two particle RDM.

## VI.2 Time propagation scheme

---

At this point the direct numerical solution appears straightforward, propagating the ground state for example via a Runge-Kutta scheme in time. But as it has been discussed for the time-dependent Schrödinger equation in section II.3, propagation schemes basing on finite differences for the time do not apply in combination with the FEDVR due to the operator of the kinetic energy. In order to overcome this obstacle, a propagation scheme is proposed which avoids the direct acting of  $T_{kin}$  on  $\rho$  and  $C^{A/S}$ . Instead it makes use of the exponential operator of the kinetic energy. For a transparent notation the propagation scheme is illustrated for a simple scalar function  $g(t)$ . The function  $g(t)$  shall be the solution of the non-linear differential equation

$$\partial_t g(t) = K g(t) + \mathcal{F}(g(t), t). \tag{VI.13}$$

Compared with the equations of motion of  $\rho_{n_a,n_b}$  and  $C_{n_a,n_b,n_c,n_d}^{S/A}$  the numerically critical part, which contains the kinetic energy, is represented by the linear term with the constant  $K$  in the right hand side of equation (VI.13). The function  $\mathcal{F}$  depends non-linearly on  $g(t)$  and has an explicit time dependency. Thus it reflects the terms of the electron-electron interaction and the coupling with the electric field. In order to avoid the problems of linear term commonly the following transformation is performed.

$$g(t) = \exp(Kt) \tilde{g}(t). \tag{VI.14}$$

Inserting equation (VI.14) in (VI.13) results in a differential equation for  $\tilde{g}$ .

$$\partial_t \tilde{g}(t) = \exp(-Kt) \mathcal{F}(g(t), t). \quad (\text{VI.15})$$

The transformation eliminates the numerical instability of the kinetic energy, but one has to recall that in the equations of motion of  $\rho_{n_a, n_b}$  and  $C_{n_a, n_b, n_c, n_d}^{S/A}$  the simple exponential function  $\exp(-Kt)$  refers to the exponential operator of  $H_0$ . Although  $H_0$  has a sparse representation in the FEDVR basis set, with increasing time the exponential operator loses this property. Therefore the transformation of equation (VI.14) for  $C_{n_a, n_b, n_c, n_d}^{S/A}$  scales with  $N_b^5$ . Less important but still cumbersome is the need to recalculate the exponential operator at each time step out of the eigenfunctions of  $H_0$ . To bypass the obstacles in the following the differential equation is rewritten in a Volterra integral equation of second kind. To this end equation (VI.15) is integrated over the interval  $[t, \Delta t]$  and the result for  $g(t + \Delta t)$  is substituted into the transformation formula (VI.14).

$$\begin{aligned} g(t + \Delta t) &= \exp(K(t + \Delta t)) \left( \tilde{g}(t) + \int_t^{t+\Delta t} dt' \exp(-Kt') \mathcal{F}(g(t'), t') \right), \\ &= \exp(K\Delta t) \left( \exp(Kt) \tilde{g}(t) + \int_t^{t+\Delta t} dt' \exp(K(t - t')) \mathcal{F}(g(t'), t') \right), \\ &= \exp(K\Delta t) \left( g(t) + \int_0^{\Delta t} dt' \exp(-Kt') \mathcal{F}(g(t + t'), t + t') \right). \end{aligned} \quad (\text{VI.16})$$

Adapting the result on the equations of motions for  $\rho_{n_a, n_b}$  and  $C_{n_a, n_b, n_c, n_d}^{S/A}$  formula contains the exponential matrix only for small time steps and thus leads to an advantageously sparse representation of  $\exp(iH^0 \Delta t / \hbar)$ . The numerical solution can be carried out via explicit solvers as discussed in [32]. However, corresponding algorithms are usually not included in standard numerical libraries and so this approach requires its own implementation. In the frame work of this thesis a 4th order Runge-Kutta scheme has been adopted, following [32].

## VI.3 Results

---

In the following, results are presented which have been obtained by the time-dependent RDM formalism for the photoionization of atoms. To this end, one-dimensional model atoms consisting of two, four and six electrons are exposed to an ultrashort XUV laser pulse. Due to the high demands on computing resources, for first testing proposes a small FEDVR basis set is constructed with  $N_{Fe} = 30$  and  $N_{GL} = 4$ . In order to optimize the discretization of the system the length of the finite elements  $L_{FE}(i) = r^{i+1} - r^i$  is chosen with respect to the inhomogeneous system. Close at the core of the atom the length of the finite elements is adjusted to  $L_1 = 0.75 a_B$  and monotonically increases up to  $L_2 = 1.2 a_B$  as illustrated in figure VI.1. The small finite elements mapping the region of the core allow a reasonable resolution of the bound states, whereas the larger spacing outside

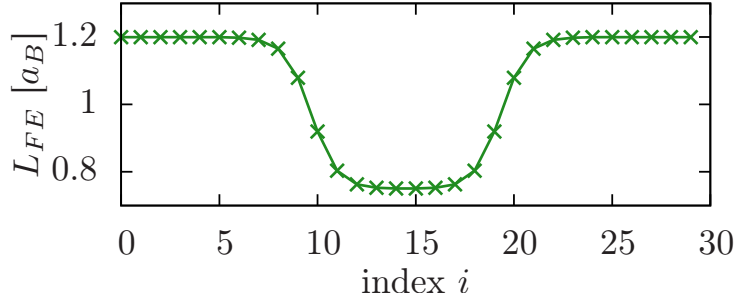


**Figure VI.1.:** The figure displays the length of the finite elements  $L_{FE}$  as a function of the index  $i \in [0 : N_{FE} - 1]$ . For the applied grid the length is determined by  $L_{FE}(i) = L_1 + (L_2 - L_1) \frac{1}{2} (1 + \tanh((L_1(i - N_{FE}/2) - 4a_B)/a_B))$  for  $i \in [N_{FE}/2 : N_{FE} - 1]$ , corresponding to  $r^i \geq 0$ . The negative  $r^i$  are obtained by the projection of the respective positive  $r^i$ . The formula realises a transition between  $L_1$  and  $L_2$  at a distance of  $4 a_b$  from the core.

of the core affects the properties of the ionization continuum. Due to the boundary conditions the complete size  $L$  of the system determines the energetic distance between the states of the continuum. Thus, the increasing size of the finite elements improves the density of states of the continuum, but on the contrary reduces the maximal available energy compared with finite elements of a constant size of  $L_1 = 0.75 a_B$ . Bearing this relation in mind, the applied grid enlarges the system as much as possible but still covers the continuum states with the energy required by the excitation conditions. Nevertheless, the chosen grid does not allow a reasonable description of the ionization, since the size  $L$  of the system is only  $31 a_B$  and an artificial behaviour must be expected. In particular, the ejected electrons easily reach the borders of the system and are reflected back to the core. Thus, impact ionization might influence the ionization dynamics and interferes with the observation of the desired relaxation mechanisms of the ion as Auger decays. Furthermore, the kinetic energy of the released electrons will probably be affected after the ionization process due to scattering processes between the free electrons.

In addition, the small system is unsuited for a long range potential like the softcore potential. Instead, the short ranged cosh potential is applied for the interaction of the electrons with the core and among themselves. The atom is exposed to a Gaussian-shaped laser.

$$\mathcal{E}(t) = E_0 \sin(\omega t) \exp[-(t - t_0)^2 / 2t_p^2]. \quad (\text{VI.17})$$

The pulse length  $t_p$  is set to 0.83 fs and maximum of the pulse is at  $t_0 = 1.21$  fs. The analysis is restricted to photon energies enabling a single-photon ionization of the bound electrons. Since the Hartree-Fock ground state is chosen as the initial state, the ionization potential of the each orbital used for the construction of the according Slater determinant is given by the corresponding Hartree-Fock eigenvalue. The quantity of interest shall be the projection of the reduced density matrix on the Hartree-Fock orbitals of the ground state.

	$E_1^{HF}$ [eV]
small grid	-27.709
converged	-27.705

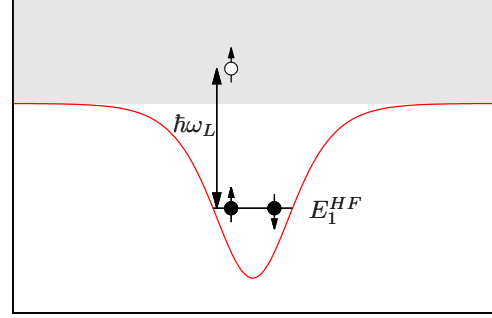


**Figure VI.2.:** The figure at the right hand side shows a schematic view of the one-dimensional two electron atom model for the applied laser excitation. In case of the TDHF as well as for the TDRDM both electrons initially occupy the lowest stationary Hartree-Fock orbital. The corresponding eigenvalue  $E_1^{HF}$  represents the single-photon ionization threshold. The table on the left side contains the results of the lowest Hartree-Fock orbital for the small grid and the converged results.

### VI.3.1. Two electron atoms

The one-dimensional model of helium interacting with a laser field is a well known system showing signatures of electron-electron correlations in the ionization dynamics, as discussed in chapter V. For the core potential as well as for the electron-electron interaction the same parametrization is applied as in chapter V.

$$V_k(x) = \frac{-6E_{Ryd}}{\cosh^2(x/a_B)}, \quad V_{el}(x_1 - x_2) = \frac{6E_{Ryd}}{2\cosh^2((x_1 - x_2)/a_B)}. \quad (\text{VI.18})$$

Figure VI.2 displays a schematic view of the initial ground state and the excitation conditions. The eigenvalue of the single particle orbital corresponding to the Hartree-Fock ground state is given in the table of figure VI.2 for the applied small grid and for a converged calculation. Obviously, the applied small grid delivers reasonable results for the energy of the orbitals of the ground state. Similar to chapter V, the photon energy shall enable a single-photon ionization process. It has been found that correlations between the electrons occur in particular in the vicinity of the ionization threshold. Therefore, this scenario represents a suitable framework for the investigation of the reduced density matrix formalism. However, the adoption of the reduced density matrix formalism on a two particle system is critical, because the system is already exact described by the one and two particle density matrix. Thus, the hierarchy of equation ends with the two-particle RDM and does not include the RDM for three or more particles. As a matter of fact, contributions resulting from reconstruction of equation (II.24) are not reliable. For example, the equation of motions VI.10 induce also a non zero contribution of the asymmetric part  $C_{n_a, n_b, n_c, n_d}^A$  and therefore violates the conservation of the initial spin singlet state of the two electrons.

Figure VI.3 (a) displays the time traces of the ground state occupation for an excitation close to the ionization threshold at  $\hbar\omega = 33$  eV and  $I = 3.52 \cdot 10^{14}$  W/cm<sup>2</sup>. Obviously, the calculation of the SUB(2) (grey dashed line) of the RDM formalism diverges, most

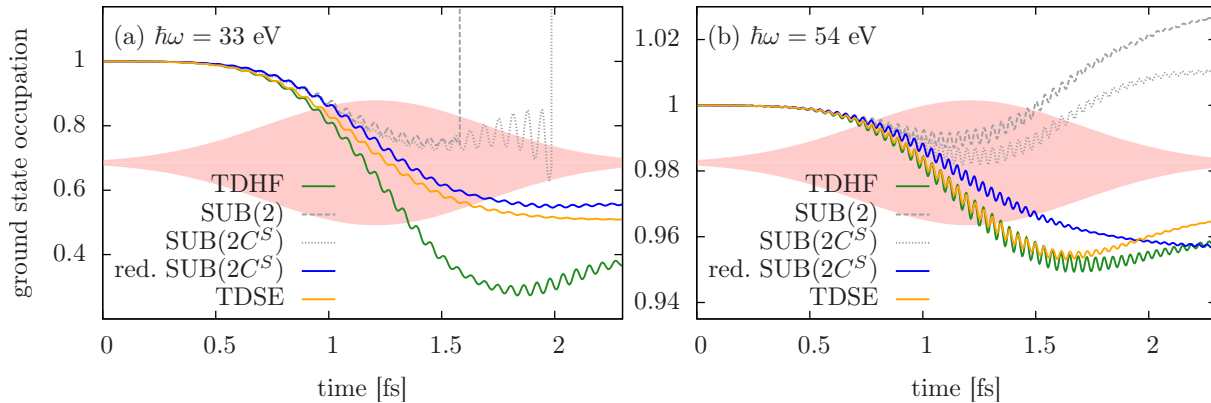


**Figure VI.3.:** Time dependence of the occupation of the first orbital are displayed at  $I = 3.52 \cdot 10^{14}$  W/cm<sup>2</sup> for  $\hbar\omega = 33$  eV (a) and  $\hbar\omega = 54$  eV (b). The results are obtained via the TDHF theory (green curve), the TDSE (orange curve), the SUB(2) level of the RDM formalism (grey dashed curve) and reductions of the SUB(2) with respect to the two-electron system (grey dotted curve and blue curve). The filed pink area represents the envelope of the electric field.

likely due to the unreliable reconstruction of the three-particle RDM for a two electron atom. In order to correct the SUB(2), two simplifying reductions are carried out. First, the asymmetric part of the correlations of the two-particle RDM is neglected in the calculation, ensuring a spin singlet of the two electron atom. This approach is denoted as SUB( $2C^S$ ) and is represented by grey dotted lines in figure VI.3. The second simplification omits the terms of the three last lines in the equations of motion (VI.10b). They stem from the reconstruction of the three-particle RDM and therefore are without meaning for the two electron atom. The corresponding curves in figure VI.3 are plotted with blue lines and labelled as "red. SUB( $2C^S$ )". Figure VI.3 (a) shows that the constriction to correlations representing a spin singlet state still results in diverging dynamics for  $\hbar\omega = 33$  eV. However, an improvement is achieved for the red. SUB( $2C^S$ ), which exhibits a monotonic decrease of the ground state occupation. To verify the dynamics of the ground state obtained with the RDM, figure VI.3 includes results for the TDSE (orange line) and the TDHF (green line). Exciting the system close above the ionization threshold at  $\hbar\omega = 33$  eV induces a large difference between both approaches in agreement with the observations of section V.1. It is found that the results of SUB( $2C^S$ ) are quite close to those of the TDSE and are most likely not influenced by an ionization threshold which is determined by the mean field of the remaining bound electrons as observed for the TDHF. Figure VI.3 (b) shows the ground state occupation as a function of time for a photon energy of  $\hbar\omega = 54$  eV. In this case the RDM formalism does not diverge. However for the complete SUB(2) as well as for the limitation to the singlet state SUB( $2C^S$ ) a ground state probability above one is obtained. The non-physical behaviour disappears if contributions of the reconstruction of the three-particle RDM are neglected (blue line, red. SUB( $2C^S$ )). In agreement with section V.1 for a photon energy inducing an excitation high above the ionization threshold the TDSE and the TDHF yield in similar ionization dynamics. In particular, the corresponding curves coincide quite well until at 1.5 fs deviations occur leading to small differences in the final ionization yields. Surprisingly, the dynamics of

	$E_1^{HF}$ [eV]	$E_2^{HF}$ [eV]
small grid	-59,87	-6,07
converged	-59,81	-6,12

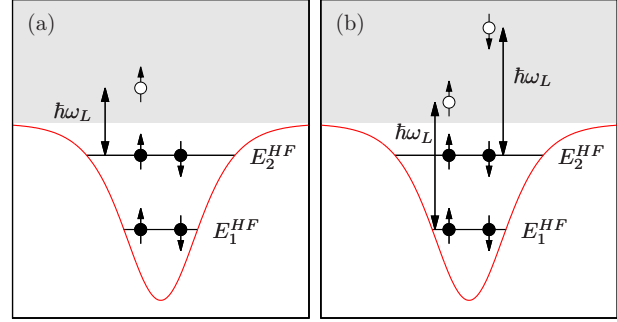


**Figure VI.4.:** Figure (a) illustrates the one-dimensional four electron atom for a laser excitation that allows the single-photon ionization of the valence shell. The position of filled electrons sketches the spin orbitals used for the construction of the Slater determinant of the initial state. Excitation conditions which enable also the single-photon ionization of the lowest bound orbital are shown in figure (b). The corresponding eigenvalues of the orbitals can be found in the table.

the red. SUB(2C<sup>S</sup>) differs from those obtained with the TDSE and TDHF even though similar ion yields are obtained.

### VI.3.2. Four electrons

In the case of four electrons the following parametrization is used for the cosh potential.

$$V_k(x) = \frac{-10E_{Ryd}}{\cosh^2(x/a_B)} \quad V_{el}(x_1 - x_2) = \frac{2E_{Ryd}}{\cosh^2((x_1 - x_2)/a_B)}. \quad (\text{VI.19})$$

Since for a neutral target atom the cosh-potential does not provide any localized self-consistent Hartree-Fock ground state the chosen parameters model a single positive charged atom. The TDRDM is applied for two types of laser excitations, illustrated in figure VI.4. First, as sketched in figure VI.4 (a), the photon energy shall enable a single-photon ionization of the second Hartree-Fock orbital but a multiphoton absorption is required to ionize the lowest Hartree-Fock orbital. Thus, one expects that the contribution to the ionization of the second Hartree-Fock orbital dominates. Second, the photon ionization shall be high enough to realise also a single-photon ionization of the lowest Hartree-Fock orbital, implying an ionization of the second Hartree-Fock orbital far above the ionization threshold (see fig VI.4 (b)). Therefore, the ionization of the lowest Hartree-Fock orbital is expected to be preferred and the creation of a hole-state might be induced.

Figures VI.5 (a) and (b) display the occupation of the first and second Hartree-Fock orbitals of the ground state as a function for  $\hbar\omega = 27$  eV at  $I = 3.52 \cdot 10^{14}$  W/cm<sup>2</sup> obtained via the TDHF and the SUB(2). The photon energy allows a single-photon ionization of the second orbital, whereas the first orbital requires the absorption of three photon for the release of an electron. Increasing the number of electrons above two obviously improves the results of the SUB(2) level of the TDRDM formalism. The dynamics of the two lowest Hartree-Fock orbitals neither diverge nor show any non physical behaviour as it has been the case for two electrons. As consequence of the excitation condition the single-photon

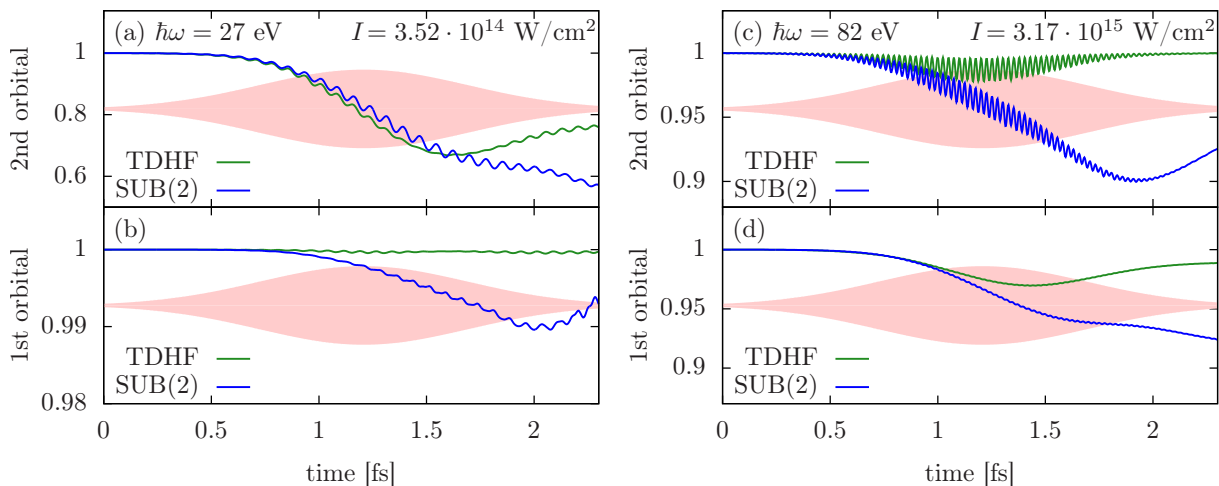


**Figure VI.5.:** Figures (a) and (b) display the time traces of the two initially occupied Hartree-Fock orbitals at a photon energy of  $\hbar\omega = 27$  eV and  $I = 3.52 \cdot 10^{14}$  W/cm<sup>2</sup> obtained via the TDHF theory (green curve) and the SUB(2) (blue curve). The photon energy corresponds to the situation sketched in fig. VI.4 (a). Results according to the excitation conditions of fig. VI.4 (b) for  $\hbar\omega = 82$  eV and  $I = 3.17 \cdot 10^{15}$  W/cm<sup>2</sup> are plotted in figures (c)-(d).

ionization of the second orbital dominates the interaction between the radiation and the atom. For the depletion during the pulse both approaches obtain quantitatively similar results but after approximately 1.5 fs differences occur. The TDHF theory predicts a slight recovery of the occupation of the second orbital whereas further ionization is found for the SUB(2) calculation. Interestingly, a different behaviour between both levels of theory is observed for the time evolution of the first Hartree-Fock orbital. In contrast to the TDHF calculation, where the first orbital is not visibly affected by the laser pulse, the results including correlations show a small depletion of the lowest orbital.

Results for the excitation condition sketched in figure VI.4 (b) are presented in figures VI.5 (c) and (d) for an intensity of  $I = 3.17 \cdot 10^{15}$  W/cm<sup>2</sup>. Even though the intensity of the radiation was enhanced, less ionization is found for  $\hbar\omega = 82$  eV than for  $\hbar\omega = 27$  eV, reflecting the decrease of the ionization cross section with increasing photon energy. For the occupation of both orbitals a stronger ionization is observed for the SUB(2) of the RDM than in case of the TDHF theory. In particular, for the TDHF theory the electrons of the second orbital follow the quivering motion induced by the oscillating electric field without being ejected. Only the electrons of the first orbital contribute to the ionization of the atom. In contrast, as illustrated in figure VI.5 (c), the SUB(2) leads additionally to the ionization of the second orbital, which even temporarily exceeds the one of the first orbital. A further remarkable feature is found in the ongoing dynamics of the SUB(2) calculations, although the intensity of the laser already decreases. In order to explain the observations for calculations including correlations, the Auger decay and the shake-off process are considered in the following. In the case of a shake-off process [35] the departing photoelectron interacts with the remaining bound electrons, resulting in a further ionization. Preferentially, an electron of an inner shell absorbs the photon and kicks out an electron of an outer shell while leaving the core. Since the applied photon

energy of  $\hbar\omega = 82$  eV exceeds the sum of the ionization threshold of both orbitals of the ground state, the shake-off process is energetically possible according to the Hartree-Fock eigenvalues and represents a reasonable explication for the observed depletion of the second orbital. After the creation of a hole in the first orbital an Auger decay can also induce the depletion of the second orbital. In this case, one of electrons of the second orbital is released to the continuum, accompanied by the decay of the other into the first orbital. On the one hand the higher depletion observed for the second orbital than for the first orbital for the SUB(2) between 1.5 fs and 2.0fs (see fig VI.5 (c) and(d)) confirms the presence of the Auger decay. On the other hand, the Auger decay is expected to lead to a higher occupation of the first orbital in the results of the SUB(2) in comparison to the TDHF theory. Unfortunately, the genuinely correlated relaxations and ionization are superimposed with scattering processes between the electrons caused by the small size of the system. In order to evaluate the influence of reflected electrons, one has to consider their energy. Photoelectrons of the first orbital are released with a low energy and in a analogous manner to the shake-off process an impact ionization of the second orbital is enabled after a reflection at the borders of the system. Therefore, in addition to the Auger decay and the shake-off process, the ionization of the second orbital is enhanced due to the small size of the system. The final rise of the second orbital for the SUB(2) could be caused by scattering events between two free electrons, transferring one electron into the bound state and the other to a continuum state of higher energy. Finally, in the presence of an Auger decay a fast reflected Auger electron might carry a sufficient energy to affect the electrons of the first orbital.

### VI.3.3. Six electrons

In the following, the TDRDM formalism is applied for an atom with six electrons. As it has been the case for four electrons, for a neutral atom with six electrons the cosh potential does not provide any localized Hartree-Fock ground state. For the chosen parametrization the atom carries initially a total charge of four positive elementary charges.

$$V_k(x) = \frac{-20E_{Ryd}}{\cosh^2(xa_b^{-1})} \quad V_{el}(x_1 - x_2) = \frac{2E_{Ryd}}{\cosh^2((x_1 - x_2)a_b^{-1})}. \quad (\text{VI.20})$$

The applied excitation conditions are sketched in figure VI.6 and are similar to the one used for four electrons. In figure VI.6 (a) the photon energy is sufficient to free an electron of the valence shell. Releasing an electron of the second orbital or the third orbital requires a multiphoton absorption. The scenario in figure VI.6 (b) considers a higher photon energy, enabling the ionization of the second orbital through a one-photon absorption. Finally, all initially occupied orbitals are accessible via a single photon absorption, as illustrated in figure VI.6 (c). The eigenvalues of the Hartree-Fock orbitals can be found in the table of figure VI.7. The variable size of the finite elements results in a small error for the Hartree-Fock eigenvalues of the lowest and therefore strongest localized orbital. In case of the following less localized states the error increases and reaches 7.7 % of the converged value of  $E_3^{HF}$  due to the enlarged finite elements.

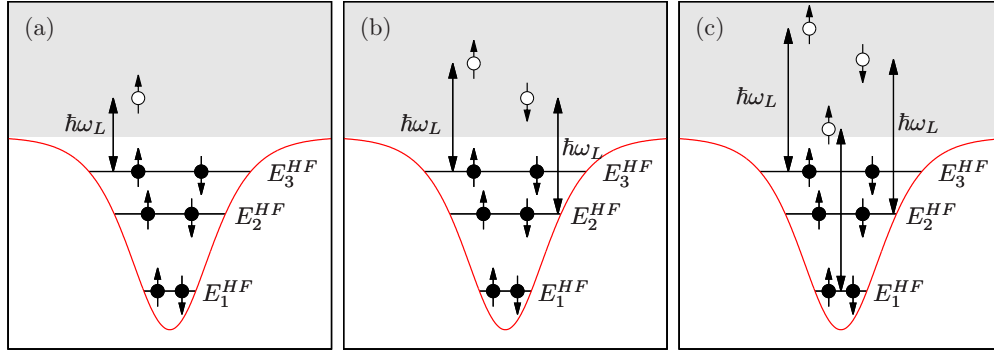


**Figure VI.6.:** The figure shows the excitation conditions applied on a one-dimensional six electron atom. In (a) the single-photon ionization is only possible for the electrons of the valence shell whereas (b) also allows the single-photon ionization of the second Hartree-Fock orbital. A further increase of the photon energy enables the single-photon ionization of all Hartree-Fock orbitals of the ground state, as sketched in (c).

According to the demand of the applied grid for a size  $L$  as large as possible for the limited basis set, these errors are acceptable.

Figures VI.7 (a)-(c) display the time dependence of the occupation of the single particle orbitals forming the Hartree-Fock ground state for an intensity of  $I = 3.52 \cdot 10^{14}$  W/cm<sup>2</sup> at a photon energy of  $\hbar\omega = 27$  eV, referring to the situation sketched in figure VI.6 (a). The laser pulse interacts almost exclusively with the electrons of the third shell, which is coupled to the continuum via a single photon absorption. The comparison between the results of the TDHF with the SUB(2) in figure VI.7 (a) reveals that for both approaches the initial ionization of the third orbital coincides until approximately the maximal field strength is reached. Afterwards the occupation determined by the TDHF recovers in contrast to the results of the SUB(2), which shows a further monotonic decrease. Since a multiphoton absorption is required for the ionization of the first and the second shell, the influence of the laser pulse is rather small compared to the valence shell (see fig. VI.7 (b) and (c)). In particular, on the scale of the respective figures no deviations from the initial occupation is found for both orbitals calculated via the TDHF. However, including correlations between the electrons induces the additional ionization of the lower lying shells even though only of a small degree.

Increasing the photon energy to  $\hbar\omega = 68$  eV realises the scenario sketched in VI.6 (b), which accounts for the single-photon ionization of the second and third orbital of the initial Hartree-Fock ground state. Figures VI.8 (a)-(c) show the corresponding occupation probabilities as a function of time for the TDHF theory and the SUB(2) at a peak intensity of  $I = 3.17 \cdot 10^{15}$  W/cm<sup>2</sup>. As expected, the first orbital plays a minor role in the ionization dynamics and the laser mainly affects the electrons of the second and the third shell. Obviously, the results accounting for correlations differ from those which include the interaction between the electrons on the mean field level. Similar to the observation for four electrons at a photon energy of  $\hbar\omega = 82$  eV, shake-off ionization and the Auger-decay might induce the higher ionization between 1.0 fs and 1.8 fs of the third orbital for correlated electrons. In addition, the less depletion of the second orbital for the SUB(2)

	small grid	converged
$E_1^{HF}$ [eV]	-149.3	-149.4
$E_2^{HF}$ [eV]	-60.5	-61.0
$E_3^{HF}$ [eV]	-5.6	-5.2

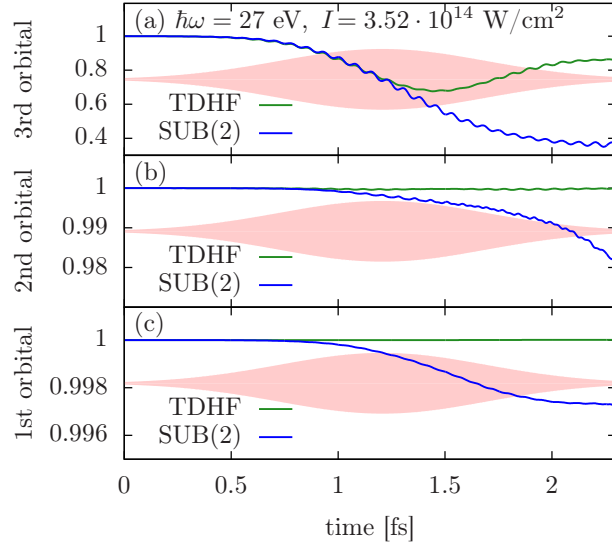


**Figure VI.7.:** Figure (a)-(c) displays the time traces of the three initially occupied Hartree-Fock orbitals at a photon energy of  $\hbar\omega = 27$  eV and  $I = 3.52 \cdot 10^{14}$  W/cm<sup>2</sup> obtained via the TDHF theory (green curve) and the correlation expansion (blue curve). The photon energy corresponds to the situation sketched in fig. VI.6 (a). The table contains the eigenvalues of the orbitals forming the Hartree-Fock ground state of the six electron atom.

compared with for the TDHF theory is in agreement with the expectation corresponding to an Auger decay. Finally, scattering processes between the free electrons probably lead to the reoccupation of the third orbital after the laser pulse as observed in the results of SUB(2) in figure VI.8 (a).

The ionization via a single-photon absorption of all initially occupied shells is enabled by increasing the photon energy to  $\hbar\omega = 163$  eV. Figures VI.8 (d)-(f) display the corresponding dynamics induced at an intensity of  $I = 1.72 \cdot 10^{16}$  W/cm<sup>2</sup>. Despite of the high intensity, the impact of the laser pulse on the bound electrons is small due to the excitation far above the ionization threshold, resulting in a reduced ionization cross section. It is found that with exception of the first orbital the calculations including correlations between the electrons yield in a higher ionization than the TDHF. The photon energy enables the shake-off ionization of the first orbital induced by the photoelectrons of the first and second orbital. Besides, also the less depletion of the first orbital in the results of the SUB(2) compared to the TDHF theory indicates the presence of Auger decays. In addition, the higher number of involved orbitals and electrons increases the number of decay channels and enables cascades of Auger decays leading to a higher ionization of the two outer shells for correlated electrons.

### VI.3.4. Remarks

The time traces of the occupation of the Hartree-Fock orbitals obtained with the SUB(2) level of the RDM formalism revealed many differences in comparison with those of the TDHF theory. The analysis points out that these differences might to some extent

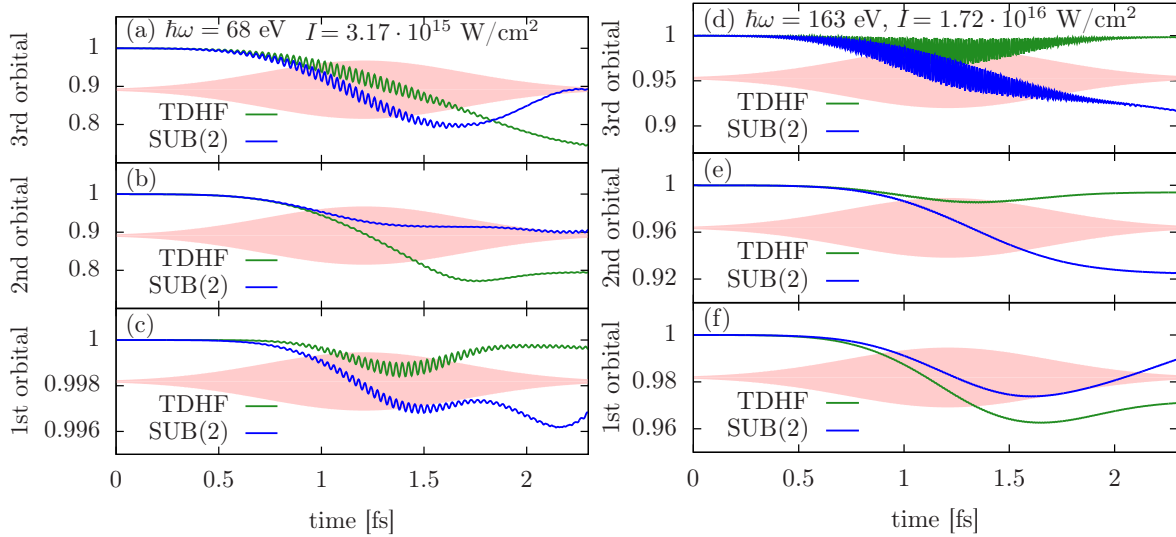


**Figure VI.8.:** Occupation probability of the three initially occupied Hartree-Fock orbitals as function of time determined via the TDHF theory (green line) and the SUB(2) of the RDM formalism (blue line). Figures (a)-(c) correspond to a laser pulse with a photon energy of  $\hbar\omega = 68$  eV and an intensity of  $I = 3.17 \cdot 10^{15}$  W/cm<sup>2</sup>. In figures (d)-(f) the properties of the laser are adjusted to  $\hbar\omega = 163$  eV and  $I = 1.72 \cdot 10^{16}$  W/cm<sup>2</sup>.

represent signatures of correlated electron-electron interaction excited by an ultrashort XUV laser pulse with extreme intensity. In particular, indications of shake-off ionization processes and Auger decays are found. Besides, an artificial behaviour was observed caused by the small spatial size of the system. A comparison with the results of Schäfer-Bung and Nest [147] was not worked out since they did not address the ionization in their investigations. Instead, they analysed the expectation value of the position operator and the energy for a one-dimensional four electron atom interacting with a laser pulse described with SUB(2) level of the TDRDM formalism. Due to the observed numerical instabilities occurring for the full SUB(2) level they limited their approach to configuration interaction with single excitations and further to independent electron pairs. They found that the numerical instabilities stem from the non-linear reconstruction of the three particle RDM and increase for high intensities and enhanced correlations between the electrons. Although the above presented results for four and six particles do not show any signs of numerical instabilities or non-physical behaviour, these problems were observed in the tested parameter range. In particular, numerical instabilities arise for an excitation of the four electron atom close to the threshold of the valence shell with a high intensity. Referring to chapter V, in this situation strong correlations are expected and thus a similar behaviour concerning numerical instabilities is observed as reported by Schäfer-Bung and Nest [147]. In addition, probabilities larger than one or smaller than zero were observed for the diagonal elements of the reduced density matrix. It is known that these problems are induced by the truncation of the hierarchy of equations of motion in the TDRDM formalism and that they are related to the violation of the trace relation (eq. (VI.4)) [150, 151]. More sophisticated truncation schemes

have already been investigated [7, 22, 107] and may provide an improved performance for the photoionization as the present approach.



# VII

## Summary and outlook

The thesis is concerned with the impact of quantum coherences and correlation effects in the dynamics of electrons for an atom exposed to intense and ultrashort XUV-laser pulses. To this end, different levels of theory were applied providing a systematic manner to evaluate the appearance of corresponding processes. As a prime example of coherent quantum dynamics the first issue of this survey were Rabi oscillations between resonantly driven bound atomic states of a one-dimensional two electron accompanied by ionization. A laser pulse enabling Rabi oscillations induces a linear intensity scaling of the ion yield. On the contrary, for pulses lengths shorter than the Rabi period a quadratic intensity scaling was found in agreement with the lowest order perturbation theory for a two-photon ionization. Consequently, at the intensity corresponding to the critical pulse area of a  $\pi$ -pulse a transition from quadratic to linear intensity scaling takes place in the ion yields. In the high intensity regime the comparison between the results of the generic model, consisting of a two level system coupled to the ionization continuum via the upper state, and the direct solution of the time-dependent Schrödinger equation reveals that the further excited localized states and the direct two-photon ionization carry a non negligible contribution to the total ionization yields. Furthermore, the analytic solution of the generic model predicted a renormalization of the Rabi frequency in comparison with an isolated two level system, caused by the losses to the continuum. Thus, the enhanced ion yields observed with the TDSE increase the renormalization of the respective Rabi frequency.

Investigations for an off-resonant excitation proved, that the basic dependency of the amplitude and the frequency of the Rabi oscillations on the detuning coincides with the one known for the isolated two level system. However, the direct two-photon ionization of the ground state gains in importance compared to the resonant case, affecting the intensity scaling of the ion yields. Instead of the critical pulse area for one Rabi cycle, at a large detuning the competition between the direct two-photon ionization and the

Rabi-assisted ionization determines the transition from a quadratic to a linear intensity scaling. For a fixed detuning the position of this transition is the same for all pulse durations as long as the ion yields have not reached the saturation regime. Besides, beats in the time evolution of the occupation probabilities of the ground state were identified as signatures of the coexistence of different Rabi processes.

The influence of correlated electron dynamics on the ionization process has been studied for a laser excitation in the vicinity of single-photon ionization threshold of a one-dimensional helium model. The comparison between the time-dependent Hartree-Fock theory and the exact numerical solution of the Schrödinger equation reveals that correlation effects gain in importance at a high radiation intensity with a photon energy close to the threshold and strongly affect the time evolution of the ground state population. It was found that in the Hartree-Fock approach the single-photon ionization threshold is determined by the mean field of the electrons remaining at the core and thus continuously increases with the rising fraction of free electrons during the interaction with the laser pulse. However, the time-dependent Schrödinger equation strictly distinguished between the threshold for electrically neutral and single ionized two electron atoms. Whenever a high photoionization raises the single-photon ionization threshold of Hartree-Fock approach above the photon energy, deviations compared to the solution including correlation have been observed. Furthermore, the momentum distributions of the electrons emitted in a double ionization process have been analysed. The characteristic signatures of different double ionization processes allowed to separate their respective parts of the total double ionization yields. In case of the coexistence of a non-sequential three-photon and a sequential two-photon double ionization, the corresponding ion yields scale quadratically or cubically with intensity. Surprisingly, the double ionization signal saturates even when its value is lower than 10%. At a high radiation intensity the three photon process clearly dominates even though the total ion yield follows a power law with an exponent below three. The time evolution of the two-electron momentum-distribution revealed a broad peak at short times which becomes narrower with ongoing time. This feature reflects the energy-time uncertainty indicating a strong coherent regime at short times. In addition, the time evolution of the different processes, contributing to the double ionization yields, shows a monotonic increase for the three photon double ionization and the two-photon process with the emission of both electrons in the opposite direction. In contrast, the ion yields for the two-photon process with both electrons leaving the atom in the same direction pass through a maximum with ongoing time, caused by a recapture process.

Finally, the time-dependent reduced density matrix formalism was applied for one-dimensional atom models interacting with an ultrashort laser pulse. To this end, the Bogolyubov-Born-Green-Kirkwood-Yvon hierarchy was truncated one level above the mean field level and therefore correlations between electrons are included. The one particle matrix and the two particle correlations were represented by the finite element discrete variable representation. The product ansatz chosen for the separation of the spin and basis function variables distinguishes between correlations of the spin singlet or of spin triplet states. The numerically obtained time traces of the Hartree-Fock orbitals which form the ground state were analysed for two, four and six electron atoms excited

by an intense ultrashort XUV laser pulse. In order to identify correlation induced process in the ionization dynamics, results of the SUB(2) level of the TDRDM formalism were compared with the TDHF theory. In this manner, signatures of the shake-off ionization process and the Auger decay were found in the time evolution of the occupation of the Hartree-Fock orbital of the ground state. Besides, the small size of the used system induced artificial behaviour because ejected electrons are reflected at the border and therefore interact with other reflected free electrons and remaining bound electrons. Consequently, the resulting in scattering events between the electrons additionally affect the population of the localized orbitals. As known the truncation of the hierarchy leads to non-linear equations of motion and violates the trace relation of the RDMs. Therefore, numerical instabilities and non physical behaviour were observed for some excitation conditions, in particular if electrons were transferred to continuum states close above the ionization threshold and a high degree of ionization was obtained.

The results of the present thesis provide several points of contact for further developments. In particular for the application of the TDRDM formalism on the photonionization of atoms additional investigations suggest themselves. The design of the present approach already strongly supports a parallel numerical implementation. However, the parallelization of the implementation only accounts for multi-core processors using a shared memory model. The limitation on the number of basis functions results in a system size only suitable for first testing purposes. With the extension to a distributed memory program which enables the computation by computer cluster the calculation of system with an increased number of basis functions becomes feasible due to the larger accessible memory. Also the Hartree-Fock ground state is commonly used as initial state in the TDRDM formalism, starting the propagation with correlated state might improve the accuracy. In addition, even though first signatures of correlated processes in the ionization dynamics obtained with the SUB(2) have been observed in the occupation of localized single particle orbitals, a more detailed analysis referring also to the kinetic energies of the free electrons is necessary for a strict confirmation of the shake-off ionization and the Auger decay.

Furthermore, extending the direct numerical solution of the TDSE of one-dimensional atoms to four electrons might prove useful for several aspects concerning the findings of this thesis. Since the SUB(2) level of the TDRDM formalism is not applicable on a two electron atom the comparison with an exact solution was not accomplished and the TDHF theory was the only reference in the case of four and six electron atoms. Thus, the TDSE for four electrons would provide a benchmark for the accuracy of the TDRDM formalism. Besides, it can access an exact treatment of the resonant Auger decay. In the resonant Auger decay the Rabi-assisted ionization is accompanied by a relaxation process [116, 132, 133] and is usually described by models close to the laser driven two level systems with additional rates modelling the photonionization and relaxation processes. Consequently, a comparison similar to chapters III and IV between the commonly used model and the exact results of the TDSE including four correlated electrons seems promising.



# Bibliography

- [1] W. Ackermann, G. Asova, V. Ayvazyan, A. Azima, N. Baboi et al. *Operation of a free-electron laser from the extreme ultraviolet to the water window*. Nature Photonics **1**, 6 (2007).
- [2] E. Allaria, R. Appio, L. Badano, W. A. Barletta, S. Bassanese et al. *Highly coherent and stable pulses from the FERMI seeded free-electron laser in the extreme ultraviolet*. Nature Photonics **6**, 10 (2012).
- [3] J. Amann, W. Berg, V. Blank, F. J. Decker, Y. Ding et al. *Demonstration of self-seeding in a hard-X-ray free-electron laser*. Nature Photonics **6**, 10 (2012).
- [4] J. Andruszkow, B. Aune, V. Ayvazyan, N. Baboi, R. Bakker et al. *First observation of self-amplified spontaneous emission in a free-electron laser at 109 nm wavelength*. Phys. Rev. Lett. **85**, 18 (2000).
- [5] L. Avaldi and A. Huetz. *Photodouble ionization and the dynamics of electron pairs in the continuum*. J. Phys. B: At. Mol. Opt. Phys. **38**, 9, SI (2005).
- [6] V. Axt and S. Mukamel. *Nonlinear optics of semiconductor and molecular nanostructures; a common perspective*. Rev. Mod. Phys. **70**, 1 (1998).
- [7] V. Axt and S. Mukamel. *Real-Space Density-Matrix Description of Dynamic Correlations in the Optical Response of Many-Electron Systems*, volume 101 of *The IMA Volumes in Mathematics and its Applications*. Springer, New York (1998).
- [8] V. M. Axt and T. Kuhn. *Femtosecond spectroscopy in semiconductors: A key to coherences, correlations and quantum kinetics*. Rep. Prog. Phys. **67** (2004).
- [9] V. Ayvazyan, N. Baboi, J. Bahr, V. Balandin, B. Beutner et al. *First operation of a free-electron laser generating GW power radiation at 32 nm wavelength*. Eur. Phys. J. D **37**, 2 (2006).
- [10] V. Ayvazyan, N. Baboi, I. Bohnet, R. Brinkmann, M. Castellano et al. *Generation of GW radiation pulses from a VUV free-electron laser operating in the femtosecond regime*. Phys. Rev. Lett. **88**, 10 (2002).

- [11] K. Balzer, S. Bauch and M. Bonitz. *Efficient grid-based method in nonequilibrium Green's function calculations: Application to model atoms and molecules*. Phys. Rev. A **81**, 2 (2010).
- [12] K. Balzer, S. Bauch and M. Bonitz. *Time-dependent second-order Born calculations for model atoms and molecules in strong laser fields*. Phys. Rev. A **82**, 3 (2010).
- [13] K. Balzer and M. Bonitz. *Nonequilibrium Green's Functions Approach to Inhomogeneous Systems*, volume 867 of *Lecture Notes in Physics*. Springer, Berlin Heidelberg (2013).
- [14] A. D. Bandrauk and H. Shen. *Improved exponential split operator method for solving the time-dependent Schrodinger-equation*. Chem. Phys. Lett. **176**, 5 (1991).
- [15] M. Beck, A. Jäckle, G. Worth and H.-D. Meyer. *The multiconfiguration time-dependent Hartree (MCTDH) method: a highly efficient algorithm for propagating wavepackets*. Phys. Reports **324**, 1 (2000).
- [16] B. L. Beers and L. Armstrong. *Exact solution of a realistic model for 2-photon ionization*. Phys. Rev. A **12**, 6 (1975).
- [17] M. Bergh, N. Timneanu and D. van der Spoel. *Model for the dynamics of a water cluster in an x-ray free electron laser beam*. Phys. Rev. E **70**, 5, 1 (2004).
- [18] M. J. Bogan, W. H. Benner, S. Boutet, U. Rohner, M. Frank et al. *Single particle X-ray diffractive imaging*. Nano Lett. **8**, 1 (2008).
- [19] C. Bostedt, E. Eremina, D. Rupp, M. Adolph, H. Thomas et al. *Ultrafast X-Ray Scattering of Xenon Nanoparticles: Imaging Transient States of Matter*. Phys. Rev. Lett. **108**, 9 (2012).
- [20] P. Burke and V. Burke. *Time-dependent R-matrix theory of multiphoton processes*. J. Phys. B: At. Mol. Opt. Phys. **30**, 11 (1997).
- [21] M. E. Casida and M. Huix-Rotllant. *Progress in Time-Dependent Density-Functional Theory*. volume 63 of *Annu. Rev. Phys. Chem.* (2012).
- [22] W. Cassing and A. Pfitzner. *Self-consistent truncation of the BBGKY hierarchy on the 2-body level*. Z. Phys. A: Hadrons Nucl. **342**, 2:161–167 (1992).
- [23] H. N. Chapman, A. Barty, M. J. Bogan, S. Boutet, M. Frank et al. *Femtosecond diffractive imaging with a soft-X-ray free-electron laser*. Nature Physics **2**, 12 (2006).
- [24] H. N. Chapman, P. Fromme, A. Barty, T. A. White, R. A. Kirian et al. *Femtosecond X-ray protein nanocrystallography*. Nature **470**, 7332 (2011).

- [25] Y. D. Chuang, W. S. Lee, Y. F. Kung, A. P. Sorini, B. Moritz et al. *Real-Time Manifestation of Strongly Coupled Spin and Charge Order Parameters in Stripe-Ordered La<sub>1.75</sub>Sr<sub>0.25</sub>NiO<sub>4</sub> Nickelate Crystals Using Time-Resolved Resonant X-Ray Diffraction*. Phys. Rev. Lett. **110**, 12 (2013).
- [26] J. Colgan, D. C. Griffin, C. P. Ballance and M. S. Pindzola. *Total cross sections for the double photoionization of Li from the ground and excited states*. Phys. Rev. A **80**, 6 (2009).
- [27] J. Colgan and M. S. Pindzola. *Angular Distributions for the Complete Photofragmentation of the Li Atom*. Phys. Rev. Lett. **108**, 5 (2012).
- [28] N. E. Dahlen and R. van Leeuwen. *Solving the Kadanoff-Baym equations for inhomogeneous systems: Application to atoms and molecules*. Phys. Rev. Lett. **98**, 15 (2007).
- [29] E. Dalgaard. *Time-dependent multiconfigurational Hartree-Fock theory*. J. Chem. Phys. **72**, 2 (1980).
- [30] C. David, S. Gorelick, S. Rutishauser, J. Krzywinski, J. Vila-Comamala et al. *Nanofocusing of hard X-ray free electron laser pulses using diamond based Fresnel zone plates*. Sci. Rep. **1** (2011).
- [31] D. Deacon, L. R. Elias, J. Madey, G. J. Ramian, H. Schwettman et al. *1st operation of a free-electron laser*. Phys. Rev. Lett. **38**, 16 (1977).
- [32] L. Delves and J. Mohamed. *Computational methods for integral equations*. Cambridge University Press (1985).
- [33] S. Di Matteo. *Resonant x-ray diffraction: multipole interpretation*. J. Phys. D: Appl. Phys. **45**, 16 (2012).
- [34] Y. Ding, F. J. Decker, P. Emma, C. Feng, C. Field et al. *Femtosecond X-Ray Pulse Characterization in Free-Electron Lasers Using a Cross-Correlation Technique*. Phys. Rev. Lett. **109**, 25 (2012).
- [35] G. Doumy, C. Roedig, S. K. Son, C. I. Bлага, A. D. DiChiara et al. *Nonlinear Atomic Response to Intense Ultrashort X Rays*. Phys. Rev. Lett. **106**, 8 (2011).
- [36] R. Dronyak, J. Gulden, O. M. Yefanov, A. Singer, T. Gorniak et al. *Dynamics of colloidal crystals studied by pump-probe experiments at FLASH*. Phys. Rev. B **86**, 6 (2012).
- [37] P. Elliott, J. I. Fuks, A. Rubio and N. T. Maitra. *Universal Dynamical Steps in the Exact Time-Dependent Exchange-Correlation Potential*. Phys. Rev. Lett. **109**, 26 (2012).
- [38] P. Emma, R. Akre, J. Arthur, R. Bionta, C. Bostedt et al. *First lasing and operation of an angstrom-wavelength free-electron laser*. Nature Photonics **4**, 9 (2010).

- [39] C. S. Fadley. *X-ray photoelectron spectroscopy: Progress and perspectives*. J. Electron. Spectrosc. Relat. Phenom. **178** (2010).
- [40] J. Feist, S. Nagele, R. Pazourek, E. Persson, B. I. Schneider et al. *Nonsequential two-photon double ionization of helium*. Phys. Rev. A **77**, 4 (2008).
- [41] M. D. Feit, J. A. Fleck and A. Steiger. *Solution of the Schrodinger-equation by a spectral method*. J. Comput. Phys. **47**, 3 (1982).
- [42] J. R. Fienup. *Phase retrieval algorithms: a comparison*. Appl. Opt. **21**, 15 (1982).
- [43] D. N. Fittinghoff, P. R. Bolton, B. Chang and K. C. Kulander. *Observation of nonsequential double ionization of helium with optical tunneling*. Phys. Rev. Lett. **69**, 18 (1992).
- [44] M. Forre, S. Selsto and R. Nepstad. *Nonsequential Two-Photon Double Ionization of Atoms: Identifying the Mechanism*. Phys. Rev. Lett. **105**, 16 (2010).
- [45] E. Fomouo, A. Hamido, P. Antoine, B. Piraux, H. Bachau et al. *Time-dependent analysis of the mechanism for two-photon double escape in helium: from very long to attosecond time scales*. J. Phys. B: At. Mol. Opt. Phys. **43**, 9 (2010).
- [46] E. Galtier, F. B. Rosmej, T. Dzelzainis, D. Riley, F. Y. Khattak et al. *Decay of Crystalline Order and Equilibration during the Solid-to-Plasma Transition Induced by 20-fs Microfocused 92-eV Free-Electron-Laser Pulses*. Phys. Rev. Lett. **106**, 16 (2011).
- [47] M. Gavrilu. *Atomic stabilization in superintense laser fields*. J. Phys. B: At. Mol. Opt. Phys. **35**, 18 (2002).
- [48] T. Gorkhover, M. Adolph, D. Rupp, S. Schorb, S. W. Epp et al. *Nanoplasma Dynamics of Single Large Xenon Clusters Irradiated with Superintense X-Ray Pulses from the Linac Coherent Light Source Free-Electron Laser*. Phys. Rev. Lett. **108**, 24 (2012).
- [49] L. Greenman, P. J. Ho, S. Pabst, E. Kamarchik, D. A. Mazziotti et al. *Implementation of the time-dependent configuration-interaction singles method for atomic strong-field processes*. Phys. Rev. A **82**, 2 (2010).
- [50] I. Grguras, A. R. Maier, C. Behrens, T. Mazza, T. J. Kelly et al. *Ultrafast X-ray pulse characterization at free-electron lasers*. Nature Photonics **6**, 12 (2012).
- [51] R. Grobe and J. H. Eberly. *Photoelectron-spectra for a 2-electron system in a strong laser field*. Phys. Rev. Lett. **68**, 19 (1992).
- [52] R. Grobe and J. H. Eberly. *Observation of coherence transfer by electron-electron correlation*. Phys. Rev. A **48**, 1 (1993).

- [53] R. Grobe and J. H. Eberly. *One-dimensional model of a negative-ion and its interaction with laser fields*. Phys. Rev. A **48**, 6 (1993).
- [54] X. Guan, K. Bartschat and B. I. Schneider. *Dynamics of two-photon double ionization of helium in short intense xuv laser pulses*. Phys. Rev. A **77**, 4 (2008).
- [55] X. Guan, O. Zatsarinny, K. Bartschat, B. I. Schneider, J. Feist et al. *General approach to few-cycle intense laser interactions with complex atoms*. Phys. Rev. A **76**, 5 (2007).
- [56] X. Guan, O. Zatsarinny, C. J. Noble, K. Bartschat and B. I. Schneider. *A time-dependent B-spline R-matrix approach to double ionization of atoms by XUV laser pulses*. J. Phys. B: At. Mol. Opt. Phys. **42**, 13 (2009).
- [57] W. Hartig, W. Rasmussen, R. Schieder and H. Walther. *Study of frequency-distribution of fluorescent light-induced by monochromatic radiation*. Z. Phys. A: Hadrons Nucl. **278**, 3:205–210 (1976).
- [58] S. Hau-Riege, R. London and A. Szoke. *Dynamics of biological molecules irradiated by short x-ray pulses*. Phys. Rev. E **69**, 5, 1 (2004).
- [59] S. P. Hau-Riege. *X-ray atomic scattering factors of low-Z ions with a core hole*. Phys. Rev. A **76**, 4 (2007).
- [60] S. P. Hau-Riege, A. Graf, T. Doepfner, R. A. London, J. Krzywinski et al. *Ultrafast Transitions from Solid to Liquid and Plasma States of Graphite Induced by X-Ray Free-Electron Laser Pulses*. Phys. Rev. Lett. **108**, 21 (2012).
- [61] S. P. Hau-Riege, R. A. London, H. Chapman and M. Bergh. *Soft-x-ray free-electron-laser interaction with materials*. Phys. Rev. E **76**, 4 (2007).
- [62] J. M. Hauser, W. Cassing and A. Peter. *2-body correlations in pionic systems*. Nucl. Phys. A **585**, 4 (1995).
- [63] D. Hochstuhl, S. Bauch and M. Bonitz. *Multiconfigurational time-dependent Hartree-Fock calculations for photoionization of one-dimensional Helium*. J. Phys.: Conf. Ser. **220**, 1 (2010).
- [64] D. Hochstuhl and M. Bonitz. *Two-photon ionization of helium studied with the multiconfigurational time-dependent Hartree-Fock method*. J. Chem. Phys. **134**, 8 (2011).
- [65] D. Hochstuhl and M. Bonitz. *Time-dependent restricted-active-space configuration-interaction method for the photoionization of many-electron atoms*. Phys. Rev. A **86**, 5 (2012).
- [66] D. A. Horner, F. Morales, T. N. Rescigno, F. Martin and C. W. McCurdy. *Two-photon double ionization of helium above and below the threshold for sequential ionization*. Phys. Rev. A **76**, 3 (2007).

- [67] D. A. Horner, T. N. Rescigno and C. W. McCurdy. *Decoding sequential versus nonsequential two-photon double ionization of helium using nuclear recoil*. Phys. Rev. A **77**, 3 (2008).
- [68] S. X. Hu. *Optimizing the FEDVR-TDCC code for exploring the quantum dynamics of two-electron systems in intense laser pulses*. Phys. Rev. E **81**, 5, 2 (2010).
- [69] K. L. Ishikawa and K. Midorikawa. *Above-threshold double ionization of helium with attosecond intense soft x-ray pulses*. Phys. Rev. A **72**, 1 (2005).
- [70] I. A. Ivanov and A. S. Kheifets. *Two-photon double ionization of helium in the region of photon energies 42-50 eV*. Phys. Rev. A **75**, 3 (2007).
- [71] S. L. Johnson, R. A. de Souza, U. Staub, P. Beaud, E. Moehr-Vorobeva et al. *Femtosecond Dynamics of the Collinear-to-Spiral Antiferromagnetic Phase Transition in CuO*. Phys. Rev. Lett. **108**, 3 (2012).
- [72] B. Kaiser. *Kurzzeitverhalten der Photoionisation durch ultrakurze hochintensive Röntgenblitze*. Diplomathesis (2010).
- [73] B. Kaiser, A. Brand, M. Glässl, A. Vagov, V. M. Axt et al. *Photoionization of resonantly driven atomic states by an extreme ultraviolet-free-electron laser: intensity dependence and renormalization of Rabi frequencies*. New J. Phys. **15**, 9 (2013).
- [74] B. Kaiser, A. Vagov, V. M. Axt and U. Pietsch. *Ultrafast photoionization dynamics at high laser intensities in the xuv regime*. Phys. Rev. A **84** (2011).
- [75] G. Kamta and A. Starace. *Multielectron system in an ultrashort, intense laser field: A nonperturbative, time-dependent two-active-electron approach*. Phys. Rev. A **65**, 5, B (2002).
- [76] E. P. Kanter, B. Kraessig, Y. Li, A. M. March, P. Ho et al. *Unveiling and Driving Hidden Resonances with High-Fluence, High-Intensity X-Ray Pulses*. Phys. Rev. Lett. **107**, 23 (2011).
- [77] T. Kato and H. Kono. *Time-dependent multiconfiguration theory for electronic dynamics of molecules in an intense laser field*. Chem. Phys. Lett. **392**, 4-6 (2004).
- [78] A. Knapp, A. Kheifets, I. Bray, T. Weber, A. Landers et al. *Mechanisms of photo double ionization of helium by 530 eV photons*. Phys. Rev. Lett. **89**, 3 (2002).
- [79] P. L. Knight. *Saturation and Rabi oscillations in resonant multiphoton ionization*. Opt. Commun. **22**, 2 (1977).
- [80] A. M. Kondratenko and E. L. Saladin. *Generation of coherent radiation by relativistic electron-beam in an undulator*. Dokl. Akad. Nauk **249**, 4 (1979).

- [81] M. Krikunova, M. Adolph, T. Gorkhover, D. Rupp, S. Schorb et al. *Ionization dynamics in expanding clusters studied by XUV pump-probe spectroscopy*. J. Phys. B: At. Mol. Opt. Phys. **45**, 10 (2012).
- [82] M. Krikunova, T. Maltezopoulos, P. Wessels, M. Schlie, A. Azima et al. *Strong-field ionization of molecular iodine traced with XUV pulses from a free-electron laser*. Phys. Rev. A **86**, 4 (2012).
- [83] A. Krugel, V. Axt, T. Kuhn, P. Machnikowski and A. Vagov. *The role of acoustic phonons for Rabi oscillations in semiconductor quantum dots*. Appl. Phys. B: Lasers Opt. **81**, 7 (2005).
- [84] K. C. Kulander. *Time-dependent Hartree-Fock theory of multiphoton ionization - helium*. Phys. Rev. A **36**, 6 (1987).
- [85] K. C. Kulander, K. J. Schafer and J. L. Krause. *Dynamic stabilization of hydrogen in an intense, high-frequency, pulsed laser field*. Phys. Rev. Lett. **66**, 20 (1991).
- [86] M. Kurka, J. Feist, D. A. Horner, A. Rudenko, Y. H. Jiang et al. *Differential cross sections for non-sequential double ionization of He by 52 eV photons from the Free Electron Laser in Hamburg, FLASH*. New J. Phys. **12** (2010).
- [87] M. Kurka, A. Rudenko, L. Foucar, K. U. Kuehnel, Y. H. Jiang et al. *Two-photon double ionization of Ne by free-electron laser radiation: a kinematically complete experiment*. J. Phys. B: At. Mol. Opt. Phys. **42**, 14 (2009).
- [88] P. Lambropoulos, L. Nikolopoulos and M. Makris. *Signatures of direct double ionization under xuv radiation*. Phys. Rev. A **72**, 1 (2005).
- [89] P. Lambropoulos, L. A. A. Nikolopoulos, M. G. Makris and A. Mihelic. *Direct versus sequential double ionization in atomic systems*. Phys. Rev. A **78**, 5 (2008).
- [90] L. Landau and E. Lifschitz. *Quantenmechanik*. Akademie-Verlag, Berlin (1979).
- [91] D. Lappas and R. van Leeuwen. *Electron correlation effects in the double ionization of He*. J. Phys. B: At. Mol. Opt. Phys. **31**, 6 (1998).
- [92] S. Laulan and H. Bachau. *Correlation effects in two-photon single and double ionization of helium*. Phys. Rev. A **68**, 1 (2003).
- [93] C. Leforstier, R. H. Bisseling, C. Cerjan, M. D. Feit, R. Friesner et al. *A comparison of different propagation schemes for the time-dependent Schrodinger-equation*. J. Comput. Phys. **94**, 1 (1991).
- [94] M. Lein, E. Gross and V. Engel. *Intense-field double ionization of helium: Identifying the mechanism*. Phys. Rev. Lett. **85**, 22 (2000).

- [95] H. T. Lemke, C. Bressler, L. X. Chen, D. M. Fritz, K. J. Gaffney et al. *Femtosecond X-ray Absorption Spectroscopy at a Hard X-ray Free Electron Laser: Application to Spin Crossover Dynamics*. *J. Phys. Chem. A* **117**, 4 (2013).
- [96] Q. Liao, Y. Zhou, C. Huang and P. Lu. *Multiphoton Rabi oscillations of correlated electrons in strong-field nonsequential double ionization*. *New J. Phys.* **14** (2012).
- [97] R. Loudon. *One-dimensional hydrogen atom*. *Am. J. Phys* **27**, 9 (1959).
- [98] M. A. Lysaght, P. G. Burke and H. W. van der Hart. *Ultrafast Laser-Driven Excitation Dynamics in Ne: An Ab Initio Time-Dependent R-Matrix Approach*. *Phys. Rev. Lett.* **101**, 25 (2008).
- [99] J. M. J. Madey. *Stimulated emission of bremsstrahlung in a periodic magnetic field*. *J. Appl. Phys.* **42**, 5 (1971).
- [100] M. Magrakvelidze, O. Herrwerth, Y. H. Jiang, A. Rudenko, M. Kurka et al. *Tracing nuclear-wave-packet dynamics in singly and doubly charged states of N-2 and O-2 with XUV-pump-XUV-probe experiments*. *Phys. Rev. A* **86**, 1 (2012).
- [101] N. Maitra, F. Zhang, R. Cave and K. Burke. *Double excitations within time-dependent density functional theory linear response*. *J. Chem. Phys.* **120**, 13 (2004).
- [102] M. G. Makris and P. Lambropoulos. *Theoretical interpretation of multiphoton ionization of neon by soft-x-ray intense radiation*. *Phys. Rev. A* **77**, 2 (2008).
- [103] M. G. Makris, P. Lambropoulos and A. Mihelic. *Theory of Multiphoton Multielectron Ionization of Xenon under Strong 93-eV Radiation*. *Phys. Rev. Lett.* **102**, 3 (2009).
- [104] A. P. Mancuso, T. Gorniak, F. Staler, O. M. Yefanov, R. Barth et al. *Coherent imaging of biological samples with femtosecond pulses at the free-electron laser FLASH*. *New J. Phys.* **12** (2010).
- [105] D. Manolopoulos and R. Wyatt. *Quantum scattering via the log derivative version of the Kohn variational principle*. *Chem. Phys. Lett.* **152**, 1 (1988).
- [106] S. Marchesini, H. He, H. Chapman, S. Hau-Riege, A. Noy et al. *X-ray image reconstruction from a diffraction pattern alone*. *Phys. Rev. B* **68**, 14 (2003).
- [107] D. Mazziotti. *Contracted Schrodinger equation: Determining quantum energies and two-particle density matrices without wave functions*. *Phys. Rev. A* **57**, 6 (1998).
- [108] H. Meyer, U. Manthe and L. S. Cederbaum. *The multi-configurational time-dependent Hartree approach*. *Chem. Phys. Lett.* **165**, 1 (1990).

- [109] M. Meyer, D. Cubaynes, V. Richardson, J. T. Costello, P. Radcliffe et al. *Two-Photon Excitation and Relaxation of the 3d-4d Resonance in Atomic Kr*. Phys. Rev. Lett. **104**, 21 (2010).
- [110] R. Moshhammer, Y. H. Jiang, L. Foucar, A. Rudenko, T. Ergler et al. *Few-Photon Multiple Ionization of Ne and Ar by Strong Free-Electron-Laser Pulses*. Phys. Rev. Lett. **98** (2007).
- [111] Y. Nabekawa, H. Hasegawa, E. Takahashi and K. Midorikawa. *Production of doubly charged helium ions by two-photon absorption of an intense sub-10-fs soft x-ray pulse at 42 eV photon energy*. Phys. Rev. Lett. **94**, 4 (2005).
- [112] Y. Nabekawa, H. Hasegawa, E. J. Takahashi and K. Midorikawa. *Nabekawa et al. reply*. Phys. Rev. Lett. **97**, 16 (2006).
- [113] M. Nagasono, E. Suljoti, A. Pietzsch, F. Hennies, M. Wellhoefer et al. *Resonant two-photon absorption of extreme-ultraviolet free-electron-laser radiation in helium*. Phys. Rev. A **75**, 5 (2007).
- [114] B. Nagler, U. Zastra, R. R. Faeustlin, S. M. Vinko, T. Whitcher et al. *Turning solid aluminium transparent by intense soft X-ray photoionization*. Nature Physics **5**, 9 (2009).
- [115] R. Neutze, R. Wouts, D. van der Spoel, E. Weckert and J. Hajdu. *Potential for biomolecular imaging with femtosecond X-ray pulses*. Nature **406**, 6797 (2000).
- [116] L. A. A. Nikolopoulos, T. J. Kelly and J. T. Costello. *Theory of ac Stark splitting in core-resonant Auger decay in strong x-ray fields*. Phys. Rev. A **84**, 6 (2011).
- [117] L. A. A. Nikolopoulos and P. Lambropoulos. *Comment on "Production of doubly charged helium ions by two-photon absorption of an intense sub-10-fs soft X-ray pulse at 42 eV photon energy"*. Phys. Rev. Lett. **97**, 16 (2006).
- [118] A. Palacios, H. Bachau and F. Martin. *Step-ladder Rabi oscillations in molecules exposed to intense ultrashort vuv pulses*. Phys. Rev. A **74**, 3 (2006).
- [119] A. Palacios, T. N. Rescigno and C. W. McCurdy. *Time-dependent treatment of two-photon resonant single and double ionization of helium by ultrashort laser pulses*. Phys. Rev. A **79**, 3 (2009).
- [120] N. Pontius, T. Kachel, C. Schuessler-Langeheine, W. F. Schlotter, M. Beye et al. *Time-resolved resonant soft x-ray diffraction with free-electron lasers: Femtosecond dynamics across the Verwey transition in magnetite*. Appl. Phys. Lett. **98**, 18 (2011).
- [121] J. Power and G. Rawitscher. *Accuracy of a hybrid finite-element method for solving a scattering Schrodinger equation*. Phys. Rev. E **86**, 6, 2 (2012).

- [122] F. Prengel and E. Scholl. *Delayed intersubband relaxation in quantum wires due to quantum kinetic Coulomb scattering*. Phys. Rev. B **59**, 8:5806–5816 (1999).
- [123] W. H. Press, S. A. Teukolsky, W. T. Vetterling and B. Flannery. *Numerical Recipes in C: The Art of scientific computing*. Cambridge University Press (1988).
- [124] A. J. Ramsay, A. Gopal, E. M. Gauger, A. Nazir, B. W. Lovett et al. *Damping of Exciton Rabi Rotations by Acoustic Phonons in Optically Excited InGaAs/GaAs Quantum Dots*. Phys. Rev. Lett. **104**, 1 (2010).
- [125] L. Redecke, K. Nass, D. P. DePonte, T. A. White, D. Rehders et al. *Natively inhibited Trypanosoma brucei cathepsin B structure determined by using an X-ray laser*. Science (2013).
- [126] T. Rescigno and C. McCurdy. *Numerical grid methods for quantum-mechanical scattering problems*. Phys. Rev. A **62**, 3 (2000).
- [127] P. R. Ribic and G. Margaritondo. *Status and prospects of x-ray free-electron lasers (X-FELs): a simple presentation*. J. Phys. D: Appl. Phys. **45**, 21 (2012).
- [128] V. Richardson, J. T. Costello, D. Cubaynes, S. Duesterer, J. Feldhaus et al. *Two-Photon Inner-Shell Ionization in the Extreme Ultraviolet*. Phys. Rev. Lett. **105**, 1 (2010).
- [129] M. Richter, S. V. Bobashev, A. A. Sorokin and K. Tiedtke. *Multiphoton ionization of atoms with soft x-ray pulses*. J. Phys. B: At. Mol. Opt. Phys. **43**, 19, SI (2010).
- [130] U. Riss and H. Meyer. *Investigation on the reflection and transmission properties of complex absorbing potentials*. J. Chem. Phys. **105**, 4 (1996).
- [131] N. Rohringer and R. Santra. *X-ray nonlinear optical processes using a self-amplified spontaneous emission free-electron laser*. Phys. Rev. A **76**, 3 (2007).
- [132] N. Rohringer and R. Santra. *Resonant Auger effect at high x-ray intensity*. Phys. Rev. A **77**, 5, B (2008).
- [133] N. Rohringer and R. Santra. *Strongly driven resonant Auger effect treated by an open-quantum-system approach*. Phys. Rev. A **86**, 4 (2012).
- [134] F. Rossi and T. Kuhn. *Theory of ultrafast phenomena in photoexcited semiconductors*. Rev. Mod. Phys. **74**, 3 (2002).
- [135] A. Rouzee, P. Johnsson, E. V. Gryzlova, H. Fukuzawa, A. Yamada et al. *Angle-resolved photoelectron spectroscopy of sequential three-photon triple ionization of neon at 90.5 eV photon energy*. Phys. Rev. A **83**, 3 (2011).
- [136] B. Rudek, D. Rolles, S.-K. Son, L. Foucar, B. Erk et al. *Resonance-enhanced multiple ionization of krypton at an x-ray free-electron laser*. Phys. Rev. A **87**, 2 (2013).

- [137] B. Rudek, S.-K. Son, L. Foucar, S. W. Epp, B. Erk et al. *Ultra-efficient ionization of heavy atoms by intense X-ray free-electron laser pulses*. *Nature Photonics* **6**, 12 (2012).
- [138] A. Rudenko, L. Foucar, M. Kurka, T. Ergler, K. U. Kuehnel et al. *Recoil-ion momentum distributions for two-photon double ionization of He and Ne by 44 eV free-electron laser radiation*. *Phys. Rev. Lett.* **101**, 7 (2008).
- [139] A. Rudenko, Y. H. Jiang, M. Kurka, K. U. Kuehnel, L. Foucar et al. *Exploring few-photon, few-electron reactions at FLASH: from ion yield and momentum measurements to time-resolved and kinematically complete experiments*. *J. Phys. B: At. Mol. Opt. Phys.* **43**, 19, SI (2010).
- [140] M. Ruggenthaler and D. Bauer. *Rabi Oscillations and Few-Level Approximations in Time-Dependent Density Functional Theory*. *Phys. Rev. Lett.* **102**, 23 (2009).
- [141] C. Ruiz, L. Plaja, L. Roso and A. Er. *Ab initio calculation of the double ionization of helium in a few-cycle laser pulse beyond the one-dimensional approximation*. *Phys. Rev. Lett.* **96**, 5 (2006).
- [142] E. Runge and E. K. U. Gross. *Density-Functional Theory for time dependent systems*. *Phys. Rev. Lett.* **52**, 12 (1984).
- [143] T. Sako, J. Adachi, A. Yagishita, M. Yabashi, T. Tanaka et al. *Suppression of ionization probability due to Rabi oscillations in the resonance two-photon ionization of He by EUV free-electron lasers*. *Phys. Rev. A* **84**, 5 (2011).
- [144] E. L. Saldin, E. A. Schneidmiller and M. V. Yurkov. *Statistical and coherence properties of radiation from x-ray free-electron lasers*. *New J. Phys.* **12** (2010).
- [145] R. Santra. *Concepts in x-ray physics*. *J. Phys. B: At. Mol. Opt. Phys.* **42**, 2 (2009).
- [146] T. Sato, A. Iwasaki, K. Ishibashi, T. Okino, K. Yamanouchi et al. *Determination of the absolute two-photon ionization cross section of He by an XUV free electron laser*. *J. Phys. B: At. Mol. Opt. Phys.* **44**, 16 (2011).
- [147] B. Schaefer-Bung and M. Nest. *Correlated dynamics of electrons with reduced two-electron density matrices*. *Phys. Rev. A* **78**, 1 (2008).
- [148] K. J. Schafer, B. Yang, L. F. DiMauro and K. C. Kulander. *Above threshold ionization beyond the high harmonic cutoff*. *Phys. Rev. Lett.* **70** (1993).
- [149] V. Schmidt. *Photoionization of atoms using synchrotron radiation*. *Rep. Prog. Phys.* **55**, 9 (1992).
- [150] K. J. Schmitt, P. G. Reinhard and C. Toepffer. *Approximate treatment of fermion systems - chaos through truncation*. *Phys. Rev. A* **40**, 1 (1989).

- [151] K. J. Schmitt, P. G. Reinhard and C. Toepffer. *Truncation of time-dependent many-body theories*. ZPA **336**, 2 (1990).
- [152] B. Schneider, L. Collins and S. Hu. *Parallel solver for the time-dependent linear and nonlinear Schrodinger equation*. Phys. Rev. E **73**, 3, 2 (2006).
- [153] B. Schuette, S. Bauch, U. Fruehling, M. Wieland, M. Gensch et al. *Evidence for Chirped Auger-Electron Emission*. Phys. Rev. Lett. **108**, 25 (2012).
- [154] U. Schwengelbeck and F. H. M. Faisal. *Ionization of the one-dimensional Coulomb atom in an intense laser field*. Phys. Rev. A **50**, 1 (1994).
- [155] M. M. Seibert, S. Boutet, M. Svenda, T. Ekeberg, F. R. N. C. Maia et al. *Femtosecond diffractive imaging of biological cells*. J. Phys. B: At. Mol. Opt. Phys. **43**, 19, SI (2010).
- [156] S.-K. Son, L. Young and R. Santra. *Impact of hollow-atom formation on coherent x-ray scattering at high intensity*. Phys. Rev. A **83**, 3 (2011).
- [157] A. A. Sorokin, S. V. Bobashev, T. Feigl, K. Tiedtke, H. Wabnitz et al. *Photoelectric effect at ultrahigh intensities*. Phys. Rev. Lett. **99**, 21 (2007).
- [158] A. A. Sorokin, M. Wellhoefer, S. V. Bobashev, K. Tiedtke and M. Richter. *X-ray-laser interaction with matter and the role of multiphoton ionization: Free-electron-laser studies on neon and helium*. Phys. Rev. A **75**, 5 (2007).
- [159] Q. Su and J. H. Eberly. *Model atom for multiphoton physics*. Phys. Rev. A **44**, 9 (1991).
- [160] Q. Su, J. H. Eberly and J. Javanainen. *Dynamics of atomic ionization suppression and electron localization in an intense high-frequency radiation-field*. Phys. Rev. Lett. **64**, 8 (1990).
- [161] A. Sytcheva, S. Pabst, S.-K. Son and R. Santra. *Enhanced nonlinear response of Ne<sup>8+</sup> to intense ultrafast x rays*. Phys. Rev. A **85**, 2 (2012).
- [162] M. Thiele, E. K. U. Gross and S. Kuemmel. *Adiabatic approximation in non-perturbative time-dependent density-functional theory*. Phys. Rev. Lett. **100**, 15 (2008).
- [163] M. Thiele and S. Kuemmel. *Hydrodynamic perspective on memory in time-dependent density-functional theory*. Phys. Rev. A **79**, 5 (2009).
- [164] M. Thiele and S. Kuemmel. *Frequency Dependence of the Exact Exchange-Correlation Kernel of Time-Dependent Density-Functional Theory*. Phys. Rev. Lett. **112**, 8 (2014).

- [165] X. Tong and S. Chu. *Multiphoton ionization and high-order harmonic generation of He, Ne, and Ar atoms in intense pulsed laser fields: Self-interaction-free time-dependent density-functional theoretical approach*. Phys. Rev. A **64**, 1 (2001).
- [166] J. Ullrich, R. Moshhammer, A. Dorn, R. Dorner, L. Schmidt et al. *Recoil-ion and electron momentum spectroscopy: reaction-microscopes*. Rep. Prog. Phys. **66**, 9 (2003).
- [167] V. Veniard, R. Taieb and A. Maquet. *Photoionization of atoms using time-dependent density functional theory*. Laser Phys. **13**, 4 (2003).
- [168] A. Vibok and G. Balintkurti. *Parametrization of complex absorbing potentials for time-dependent quantum dynamics*. J. Chem. Phys. **96**, 22 (1992).
- [169] S. M. Vinko, O. Ciricosta, B. I. Cho, K. Engelhorn, H.-K. Chung et al. *Creation and diagnosis of a solid-density plasma with an X-ray free-electron laser*. Nature **482**, 7383 (2012).
- [170] H. Wabnitz, A. de Castro, P. Gurtler, T. Laarmann, W. Laasch et al. *Multiple ionization of rare gas atoms irradiated with intense VUV radiation*. Phys. Rev. Lett. **94**, 2 (2005).
- [171] B. Walker, M. Kaluza, B. Sheehy, P. Agostini and L. Dimauro. *Observation of continuum-continuum Autler-Townes splitting*. Phys. Rev. Lett. **75**, 4 (1995).
- [172] B. Walker, B. Sheehy, L. F. Dimauro, P. Agostini, K. J. Schafer et al. *Precision-measurement of strong-field double-ionization of helium*. Phys. Rev. Lett. **73**, 9 (1994).
- [173] S. J. Wang and W. Cassing. *Explicit treatment of n-body correlations within a density-matrix formalism*. Ann. Phys. **159**, 2 (1985).
- [174] M. Yabashi, H. Tanaka, T. Tanaka, H. Tomizawa, T. Togashi et al. *Compact XFEL and AMO sciences: SACLA and SCSS*. J. Phys. B: At. Mol. Opt. Phys. **46**, 16, SI (2013).
- [175] L. Young, E. P. Kanter, B. Kraessig, Y. Li, A. M. March et al. *Femtosecond electronic response of atoms to ultra-intense X-rays*. Nature **466**, 7302 (2010).
- [176] L. H. Yu. *Generation of intense UV-radiation by subharmonically single-pass free-electron lasers*. Phys. Rev. A **44**, 8 (1991).



# Publications

## As first author

- Kaiser B., A. Vagov, V. M. Axt, U. Pietsch  
*Ultrafast photionization at high laser intensities in the xuv regime*  
Physical Review A Vol. 84, 043431 (2011)
- Kaiser B., A. Brandt, M. Glässl, A. Vagov, V. M. Axt, U. Pietsch  
*Photoionization of resonantly driven atomic states by an extreme ultraviolet-free-electron laser: intensity dependence and renormalization of Rabi frequencies*  
New Journal of Physics, Vol. 15, 93016 (2013)

## As co-author

- M. Burgis, V. Schaller, M. Glässl, B. Kaiser, W. Köhler, A. Krekhov and W. Zimmermann  
*Anomalous diffusion in viscosity landscapes*  
New Journal of Physics, Vol. 13, 43031 (2011)
- A. Brand, B. Kaiser, A. Vagov, V. M. Axt, U. Pietsch  
*Non-Markovian behavior of ultrafast coherent ionization dynamics in a crystal exposed to a seeded free-electron-laser pulse*  
Physical Review A Vol. 89, 063404 (2014)



# Acknowledgment

I would like to thank everyone who has supported and accompanied me during the work on this thesis.

- As supervisor of this thesis gratitude is owed to Vollrath Martin Axt for his help and advice in many fruitful discussions. His enthusiasm for physics and science has inspired me and I have benefited a lot from his experiences.
- My special thanks go to Alexei Vagov for his continuous support and his ideas concerning my thesis.
- I would like to thank all members and alumni of the group for the pleasant company and the challenging table tennis matches, in particular to my room mate Martin Gläßl as well as Christoph Thurn, Markus Hofman, Moritz Cygorek and Jonas Seeberger. Special thanks go to André Brand as closest co-worker for the support concerning numerical and programming issues, the lively exchange on XFEL physics and for carefully reading and checking of the manuscript.
- I gratefully acknowledge the financial support by the Bundesministerium für Bildung und Forschung BMBF through the grant 05K10WCA.
- I would like to thank Anne-Valérie Foucher, my family and my friends for their large support and encouragement.